



UNIVERSIDADE ESTADUAL DE CAMPINAS

Faculdade de Engenharia Mecânica

RENAN NASCIMENTO FERREIRA

**Numerical and Experimental Bending and Torsional
Fatigue Analysis of Lightweight Crankshafts**

**Análise Numérica e Experimental de Fadiga de
Flexão e Torção em Virabrequins Leves**

CAMPINAS

2021

RENAN NASCIMENTO FERREIRA

Numerical and Experimental Bending and Torsional Fatigue Analysis of Lightweight Crankshafts

Análise Numérica e Experimental de Fadiga de Flexão e Torção em Virabrequins Leves

Dissertation presented to the School of Mechanical Engineering of the University of Campinas in partial fulfillment of the requirements for the degree of Master, in the area of Solid Mechanics and Mechanical Design.

Dissertação apresentada à Faculdade de Engenharia Mecânica da Universidade Estadual de Campinas como parte dos requisitos exigidos para a obtenção do título de Mestre em Engenharia Mecânica, na Área de Mecânica dos Sólidos e Projeto Mecânico.

Orientador: Prof. Dr. Marco Lucio Bittencourt

ESTE EXEMPLAR CORRESPONDE À VERSÃO FINAL DA DISSERTAÇÃO DEFENDIDA PELO ALUNO RENAN NASCIMENTO FERREIRA, E ORIENTADA PELO PROF. DR. MARCO LUCIO BITTENCOURT.

CAMPINAS

2021

Ficha catalográfica
Universidade Estadual de Campinas
Biblioteca da Área de Engenharia e Arquitetura
Rose Meire da Silva - CRB 8/5974

F413n Ferreira, Renan Nascimento, 1992-
Numerical and experimental bending and torsional fatigue analysis of
lightweight crankshafts / Renan Nascimento Ferreira. – Campinas, SP : [s.n.],
2021.

Orientador: Marco Lucio Bittencourt.
Dissertação (mestrado) – Universidade Estadual de Campinas, Faculdade
de Engenharia Mecânica.

1. Virabrequim. 2. Fadiga. 3. Indústria automobilística. 4. Métodos
numéricos. I. Bittencourt, Marco Lucio, 1964-. II. Universidade Estadual de
Campinas. Faculdade de Engenharia Mecânica. III. Título.

Informações para Biblioteca Digital

Título em outro idioma: Análise numérica e experimental de fadiga de flexão e torção em virabrequins leves

Palavras-chave em inglês:

Crankshaft

Fatigue

Automotive industry

Numerical methods

Área de concentração: Mecânica dos Sólidos e Projeto Mecânico

Titulação: Mestre em Engenharia Mecânica

Banca examinadora:

Marco Lucio Bittencourt [Orientador]

Pablo Siqueira Meirelles

Alexandre Schalch Mendes

Data de defesa: 14-10-2021

Programa de Pós-Graduação: Engenharia Mecânica

Identificação e informações acadêmicas do(a) aluno(a)

- ORCID do autor: <https://orcid.org/0000-0003-4714-6384>

- Currículo Lattes do autor: <http://lattes.cnpq.br/2818410665896026>

**UNIVERSIDADE ESTADUAL DE CAMPINAS
FACULDADE DE ENGENHARIA MECÂNICA**

DISSERTAÇÃO DE MESTRADO ACADÊMICO

**Numerical and Experimental Bending and Torsional
Fatigue Analysis of Lightweight Crankshafts**

**Análise Numérica e Experimental de Fadiga de
Flexão e Torção em Virabrequins Leves**

Autor: Renan Nascimento Ferreira

Orientador: Prof. Dr. Marco Lucio Bittencourt

A Banca Examinadora composta pelos membros abaixo aprovou esta Dissertação:

Prof. Dr. Marco Lúcio Bittencourt
FEM/UNICAMP

Prof. Dr. Pablo Siqueira Meirelles
FEM/UNICAMP

Dr. Alexandre Schalch Mendes
AAS Consultoria - Simulações Avançadas em CAE

A Ata de Defesa com as respectivas assinaturas dos membros encontra-se no SIGA/Sistema de Fluxo de Dissertação/Tese e na Secretaria do Programa da Unidade.

Campinas, 14 de Outubro de 2021.

*Dedico este trabalho aos meus pais e ao
meu irmão, que nunca faltaram nos
momentos difíceis e me deram uma base
familiar forte,
à Bianca, minha eterna companheira e
maior motivadora e à memória de meus
avós, Benedito e Eunice, minhas
maiores fontes de sabedoria.*

ACKNOWLEDGEMENTS

Agradeço ao professor Marco Lúcio Bittencourt por sua orientação dedicada, pelos conhecimentos compartilhados e por ter me dado a oportunidade de trabalhar em sua equipe por meio deste projeto. Também agradeço ao professor Paulo Roberto Zampieri, que contribuiu neste trabalho com sua grande experiência na área automotiva.

Eu não poderia deixar de agradecer todo o time do Laboratório de Ensaio Dinâmicos, LabEDin. Foi uma honra poder trabalhar em um laboratório que possui uma história tão respeitada e repleta de grandes realizações. Agradeço ao Vivan e ao Kazumi por todo conhecimento sobre testes experimentais que foi compartilhado. Agradeço ao Marcelo e ao Fábio por todo o suporte na montagem dos testes experimentais e ao Sérgio pela grande ajuda com a instrumentação das amostras e com os serviços de eletrônica. Obrigado, Geraldo e Leonildo, por todo serviço de usinagem e soldagem prestados. Obrigado, Eduardo, por ter compartilhado sua experiência com ensaios de fadiga em virabrequins no início deste projeto.

Agradeço ao professor Pablo Siqueira Meirelles pelo espaço disponibilizado no laboratório. Também agradeço ao professor Janito Vaqueiro Ferreira pelo empréstimo dos equipamentos essenciais para a realização deste trabalho. Sou grato ao Fernando Ortolano por ter me ajudado na montagem do setup dos ensaios de fadiga e no reparo de equipamentos. Este trabalho não seria possível sem a ajuda e experiência do time que compõe o LabEDin.

Também não posso deixar de agradecer à Ferramentaria Jundiaí pelo serviço de excelência prestado e pela qualidade na usinagem e confecção dos equipamentos de ensaio. Agradeço ao Laudinei por todo cuidado, dedicação e aconselhamento no projeto do aparato de teste de fadiga. Também agradeço ao Costa e ao Maurício por estarem sempre dispostos a ouvir e ajudar. Desta forma, agradeço a toda a equipe da Ferramentaria Jundiaí pelo envolvimento e pelos serviços prestados.

Agradeço à Fundação de Amparo à Pesquisa do Estado de São Paulo (FAPESP) pelo financiamento do projeto que possibilitou a confecção dos equipamentos utilizados neste trabalho. O presente trabalho foi realizado com apoio da Coordenação de Aperfeiçoamento de Pessoal de Nível Superior – Brasil (CAPES) – Código de Financiamento 001.

Quero agradecer a todos os amigos e funcionários da UNICAMP que contribuíram com este trabalho. Agradeço ao Wagner por todo seu envolvimento e dedicação no projeto dos equipamentos de teste. Obrigado, João, por sua dedicação e por suas contribuições na análise de fadiga numérica. Obrigado, Victor e Matheus, pelas conversas e pela amizade. Obrigado, Ana, por me ajudar com as dúvidas que eu tinha no início do mestrado. Obrigado, Luiz Toledo, pela

amizade e por ter me incentivado durante o período escolar.

Por fim, quero agradecer à minha família, que sempre esteve presente e não mediu esforços para me ajudar no que fosse necessário. Agradeço aos meus pais, Afonso e Miriam, que investiram em minha educação e me deram todo o apoio para que eu pudesse trilhar o meu caminho. Agradeço ao meu irmão, Raynan, por ser fonte de alegria e trazer felicidade em minha vida. Agradeço à minha companheira, Bianca, porque foi a minha sustentação para os momentos difíceis e por me fazer sorrir todos os dias. Nenhum passo eu daria sem a ajuda e o apoio da minha família. Agradeço à Deus por ter me abençoado com as pessoas que me cercam.

RESUMO

O desenvolvimento de projetos otimizados que visam a redução da emissão de gases poluentes e aumento da eficiência de motores de combustão interna tem impulsionado a busca por virabrequins leves na indústria automotiva. Contudo, a subtração de massa desses componentes desperta preocupação com relação à resistência à fadiga devido à grande concentração de tensão nas regiões mais críticas do virabrequim, que são submetidas ao carregamento dinâmico gerado pelos ciclos de combustão e vibração torcional. Os testes de fadiga de novos modelos de virabrequins são caros e demorados. Este trabalho investigou a influência da subtração de massa na resistência à fadiga de um modelo comercial de virabrequim. Visando a redução de custo dos ensaios de fadiga e redução de massa de virabrequins, este trabalho aplicou uma abordagem numérica para estimar a resistência à fadiga do protótipo leve e do modelo original. Os resultados numéricos foram comparados com ensaios experimentais de fadiga realizados em aparatos de ressonância e analisados pelo método *staircase*. Os resultados numéricos e experimentais mostraram que cerca de 10% da massa pode ser subtraída do virabrequim original sem afetar de forma considerável a resistência à fadiga e o balanceamento. A abordagem numérica da análise de fadiga mostrou boa correlação com as medidas experimentais.

Palavras-chave: Virabrequim; Fadiga; Indústria automotiva; Métodos numéricos; Redução de peso.

ABSTRACT

The development of optimized projects aiming to reduce the emission of pollutants gases and increase the efficiency of internal combustion engines has boosted the search for lightweight crankshafts in the automotive industry. However, the mass subtraction of this component arise concern about the fatigue strength due to the high stress concentration in the critical regions, which are subjected to the dynamic loading generated by the combustion cycles and torsional vibration. The fatigue tests of new crankshaft models are expensive and time consuming. This work investigated the influence of the mass subtraction in the fatigue strength of a commercial crankshaft model. Aiming to the cost reduction of the fatigue tests and the mass reduction of crankshafts, this work applied a numerical approach for estimating the fatigue strength of the lightweight prototype and the original crankshaft model. The numerical results were compared to experimental fatigue tests that were carried out in resonant test rigs and analyzed by the staircase method. The numerical and experimental results showed that about 10% of mass can be subtracted from the original model without considerable influence on the fatigue strength and balancing. The numerical approach of the fatigue analysis showed good agreement with experimental measurements.

Keywords: Crankshaft; Fatigue; Automotive industry; Numerical methods; Lightweighting.

LIST OF FIGURES

FIGURE 1.1 – SCHEMATIC DRAWING OF A FOUR-CYLINDER CRANKSHAFT (MORAES, 2017).....	17
FIGURE 1.2 – SETUP FOR THE BENDING RESONANT FATIGUE TEST. AVAILABLE FROM (MORAES, 2017).....	18
FIGURE 1.3 – SKETCH OF A LOCOMOTIVE SHAFT FROM THE 18TH CENTURY. MODIFIED FROM (SIMÕES, 2012).....	19
FIGURE 1.4 – A. PROVOST INTERPRETATION OF THE VERSAILLES RAIL ACCIDENT.	20
FIGURE 2.1 – THE SEVENTEEN SUSTAINABLE DEVELOPMENT GOALS OF THE UNITED NATIONS. AVAILABLE FROM HTTPS://SUSTAINABLEDEVELOPMENT.UN.ORG/SDGS	27
FIGURE 2.2 – ORIGINAL CRANKTHROW AND CRANKSHAFT GEOMETRY.....	28
FIGURE 2.3 – BOUNDARY CONDITIONS APPLIED TO THE CRANKTHROW FOR THE STATIC BENDING SIMULATION.	29
FIGURE 2.4 – MESH USED IN THE STATIC BENDING SIMULATION.	30
FIGURE 2.5 – EQUIVALENT VON MISES STRESS DISTRIBUTION FOR THE STATIC BENDING SIMULATION.	30
FIGURE 2.6 – BOUNDARY CONDITIONS APPLIED TO THE CRANKTHROW IN THE STATIC TORSION SIMULATION.	30
FIGURE 2.7 – MESH USED IN THE STATIC TORSION SIMULATION.	31
FIGURE 2.8 – EQUIVALENT VON MISES STRESS DISTRIBUTION FOR A STATIC TORSION SIMULATION.	31
FIGURE 2.9 – MODIFICATIONS PROPOSED FOR MASS REDUCTION IN THE CRANKSHAFT.....	32
FIGURE 2.10 – BOUNDARY CONDITIONS FOR STATIC STRUCTURAL ANALYSES CONSIDERED FOR THE MASS REDUCTION PROCEDURE.....	33
FIGURE 2.11 – DETAILED SKETCH OF OPTIMIZED CRANKTHROW.	33
FIGURE 2.12 – 3D GEOMETRIES OF THE LIGHTWEIGHT CRANKTHROW AND CRANKSHAFT.....	34
FIGURE 2.13 – FORCES ACTING IN A SINGLE CYLINDER ENGINE (RANGWALA, 2006).	36
FIGURE 2.14 - SKETCH OF SYMMETRICAL VERTICAL FORCES ACTING ON THE CRANKSHAFT.	37
FIGURE 2.15 – PLANE OF SYMMETRY IN A FOUR-CYLINDER ENGINE CRANKSHAFT.	37
FIGURE 2.16 – 3D MODEL GEOMETRY OF THE CRANKSHAFT MODIFIED BY RODRIGUES (2013).	38
FIGURE 3.1 – BENDING TEST RIG COMPONENTS (MORAES, 2017).	40
FIGURE 3.2 – TORSION TEST RIG COMPONENTS.....	41
FIGURE 3.3 – 3D GEOMETRY OF THE TORSION TEST RIG.....	41
FIGURE 3.4 – (A) BENDING AND (B) TORSION TEST RIG.....	42
FIGURE 3.5 – INERTIA PLATE COMPONENTS.	42
FIGURE 3.6 – ASSEMBLY OF THE INTERNAL SLEEVE, INTERNAL BEARING AND CRANKTHROW.....	44
FIGURE 3.7 – INTERNAL SLEEVE GEOMETRY.....	44
FIGURE 3.8 – FIXED SUPPORT ASSEMBLY IN 3D GEOMETRY.....	45
FIGURE 3.9 – GEOMETRY (A) AND MESH (B) USED IN THE MODAL AND HARMONIC RESPONSE ANALYSES.	46
FIGURE 3.10 – BENDING (A) AND TORSION (B) MODES OF VIBRATION AND RESPECTIVE NATURAL FREQUENCIES.	47
FIGURE 3.11 – INPUT FORCE APPLIED TO THE INERTIA PLATE IN THE TORSION HARMONIC RESPONSE ANALYSIS.....	48
FIGURE 3.12 – ACCELERATION OF THE TORSION HARMONIC RESPONSE ANALYSIS FOR DAMPING RATIO OF 0.01.....	48

FIGURE 3.13 – VON MISES STRESS RESULTS OF THE TORSION HARMONIC RESPONSE ANALYSIS FOR DAMPING RATIO OF 0.01	49
FIGURE 3.14 – STRESS IN THE OIL HOLE IN TERMS OF THE ACCELERATION RESPONSE FOR DIFFERENT VALUES OF DAMPING RATIO.	50
FIGURE 4.1 – EXAMPLE OF THE ROSETTE STRAIN GAGE PLACEMENT IN A TORSION CRANKSHAFT SPECIMEN.	53
FIGURE 4.2 – SETUP FOR THE BENDING STATIC CALIBRATION. MODIFIED FROM (MORAES, 2017).	54
FIGURE 4.3 – SETUP OF THE TORSION STATIC CALIBRATION.	54
FIGURE 4.4 – BOUNDARY CONDITIONS OF THE (A) BENDING AND (B) TORSION STATIC CALIBRATIONS.	56
FIGURE 4.5 – MODIFIED SHAFTS ASSEMBLED IN THE INTERNAL SLEEVES OF THE TORSIONAL TEST RIG.	56
FIGURE 4.6 – BOTTOM CENTER VON MISES STRESS FOR 700 NM BENDING MOMENT.	57
FIGURE 4.7 – TOP CENTER VON MISES STRESS FOR 200 NM TORSION MOMENT.	57
FIGURE 4.8 – VON MISES STRESS DISTRIBUTION OF THE (A) ORIGINAL AND (B) LIGHTWEIGHT CRANKSHAFTS SUBJECTED TO 700 NM BENDING MOMENT.	58
FIGURE 4.9 – VON MISES STRESS DISTRIBUTION OF THE (A) ORIGINAL AND (B) LIGHTWEIGHT CRANKSHAFTS SUBJECTED TO 700 NM TORSION MOMENT.	58
FIGURE 4.10 – EXPERIMENTAL AND NUMERICAL RESULTS OF THE BENDING STATIC CALIBRATION FOR THE (A) ORIGINAL AND (B) LIGHTWEIGHT CRANKSHAFT MODELS.	59
FIGURE 4.11 – EXPERIMENTAL AND NUMERICAL RESULTS OF THE TORSION STATIC CALIBRATION FOR THE (A) ORIGINAL AND (B) LIGHTWEIGHT CRANKSHAFT MODELS.	60
FIGURE 4.12 – BENDING TEST RIG SUSPENDED BY WIRES THROUGH THE LIFTING EYES.	61
FIGURE 4.13 – SPIRIT LEVEL USED IN THE BENDING TEST RIG ALIGNMENT.	62
FIGURE 4.14 – BENDING TEST RIG SETUP.	62
FIGURE 4.15 – SHAKER FIXATION AND ACCELEROMETER POSITIONING IN THE INERTIA PLATES OF THE TORSIONAL TEST RIG.	63
FIGURE 4.16 – TORSIONAL TEST RIG SETUP.	63
FIGURE 4.17 – DYNAMIC CALIBRATION SETUP SCHEME. MODIFIED FROM (MORAES, 2017).	64
FIGURE 4.18 – STRESS DATA SAMPLING OF THE LIGHTWEIGHT CRANKSHAFT DYNAMIC CALIBRATION RECORDED FOR 5G IN THE BENDING MODE.	65
FIGURE 4.19 – BENDING AND TORSION RESONANCE FREQUENCIES OF THE ORIGINAL AND LIGHTWEIGHT MODELS.	66
FIGURE 4.20 – OSCILLOSCOPE SCREEN SHOWING THE ACCELERATION RESPONSE OF THE BENDING DYNAMIC CALIBRATION OF THE LIGHTWEIGHT MODEL.	67
FIGURE 4.21 – OSCILLOSCOPE SCREEN SHOWING THE ACCELERATION RESPONSE OF THE TORSION DYNAMIC CALIBRATION OF THE ORIGINAL CRANKSHAFT MODEL.	68
FIGURE 4.22 – BENDING DYNAMIC CALIBRATION CURVES OF THE ORIGINAL AND LIGHTWEIGHT CRANKSHAFT MODELS.	69
FIGURE 4.23 – TORSION DYNAMIC CALIBRATION CURVES OF THE ORIGINAL AND LIGHTWEIGHT CRANKSHAFT MODELS.	70
FIGURE 5.1 – FLOW DIAGRAM FOR FATIGUE TEST IN CRANKSHAFTS. AVAILABLE FROM (MORAES, 2017).	72

FIGURE 5.2 – REPRESENTATION OF THE STAIRCASE DATA FOR THE ORIGINAL CRANKSHAFT MODEL TESTED IN THE BENDING.	75
FIGURE 5.3 – VISUAL REPRESENTATION OF THE STAIRCASE DATA OF THE ORIGINAL CRANKSHAFT MODEL TESTED IN THE TORSION.	76
FIGURE 5.4 – PENETRANT LIQUID APPLIED TO THE CRANKSHAFT SPECIMEN.	81
FIGURE 5.5 – CRACK ON THE FILLET RADIUS SURFACE OF THE ORIGINAL CRANKSHAFT MODEL.	81
FIGURE 5.6 – CRACK ON THE (A) SURFACE AND (B) INNER REGION OF THE CRANKPIN OF THE LIGHTWEIGHT CRANKSHAFT MODEL.	82
FIGURE 5.7 – OSCILLOSCOPE SCREEN DISPLAYING THE MAXIMUM ACCELERATION RESPONSE AND THE RESONANCE FREQUENCY OF THE CRANKSHAFT SPECIMEN IN FATIGUE PROCESS.	84
FIGURE 5.8 – CRACK PROPAGATION REGIONS IN THE CRANKWEB OF THE LIGHTWEIGHT CRANKSHAFT MODEL.	85
FIGURE 5.9 – CRACK INITIATED IN THE SURFACE OF THE TORSION SPECIMEN OF THE LIGHTWEIGHT CRANKSHAFT MODEL.	85
FIGURE 5.10 – S-N CURVES FOR EXPERIMENTAL SPECIMEN, CORRESPONDING FULLY REVERSED AXIAL AND BENDING LOAD CASES. AVAILABLE FROM (MORAES, 2017).	87
FIGURE 5.11 – LOCALIZATION OF THE (A) FORCE APPLICATION AND (B) MEASUREMENT OF ACCELERATION ON THE INERTIA PLATE.	88
FIGURE 5.12 – THE VON MISES STRESS DISTRIBUTION IN THE (A) ORIGINAL CRANKSHAFT AND (B) CUT VIEW OF THE FILLET RADIUS FOR ACCELERATION OF 6.43 G.	89
FIGURE 5.13 – DAMAGE IN THE FILLET RADII OF THE ORIGINAL CRANKSHAFT FOR ACCELERATION OF 6.43 G.	90
FIGURE 5.14 – SAFETY FACTOR IN THE FILLET RADII OF THE ORIGINAL CRANKSHAFT FOR ACCELERATION OF 6.43 G.	90
FIGURE A.1 – INERTIA PLATE BASE DRAWING WITH DIMENSIONS IN MM.	97
FIGURE A.2 – INERTIA PLATE ARM DRAWING WITH DIMENSIONS IN MM.	98
FIGURE A.3 – INERTIA PLATE BLOCK DRAWING WITH DIMENSIONS IN MM.	99
FIGURE A.4 – EXTERNAL SLEEVE DRAWING WITH DIMENSIONS IN MM.	100
FIGURE A.5 – INTERNAL SLEEVE DRAWING WITH DIMENSIONS IN MM.	101
FIGURE A.6 – SHAFT DRAWING WITH DIMENSIONS IN MM.	102
FIGURE A.7 – UPPER FIXED SUPPORT WITH DIMENSIONS IN MM.	103
FIGURE A.8 – BOTTOM FIXED SUPPORT WITH DIMENSIONS IN MM.	104
FIGURE A.9 – BEARING SUPPORT WITH DIMENSIONS IN MM.	105

LIST OF TABLES

TABLE 2.1 – MATERIALS PROPERTIES OF THE ORIGINAL CRANKSHAFT.	28
TABLE 2.2 – COMPARISON OF MASS REDUCTION EFFECTS IN DIFFERENT CRANKSHAFT MODELS.	34
TABLE 3.1 – ELEMENT SIZE USED IN THE MODAL AND HARMONIC RESPONSE ANALYSES.	47
TABLE 3.2 – CAST IRON AND STRUCTURAL STEEL MATERIAL PROPERTIES.	47
TABLE 3.3 – TORSION HARMONIC RESPONSE ANALYSIS RESULTS FOR DIFFERENT VALUES OF DAMPING RATIO.	50
TABLE 4.1 – MESH PARAMETERS FOR THE BENDING STATIC CALIBRATION.	55
TABLE 4.2 – MESH PARAMETER FOR THE TORSION STATIC CALIBRATION.	56
TABLE 4.3 – NUMERICAL AND EXPERIMENTAL RESONANCE FREQUENCY OF THE BENDING VIBRATION MODE FOR DIFFERENT CRANKSHAFT MODELS.	67
TABLE 4.4 – NUMERICAL AND EXPERIMENTAL RESONANCE FREQUENCY OF THE TORSION VIBRATION MODE FOR DIFFERENT CRANKSHAFT MODELS.	67
TABLE 5.1 – NUMBER OF SPECIMENS AND STEP SIZE APPLIED TO THE FATIGUE TESTS OF THE ORIGINAL CRANKSHAFT.	75
TABLE 5.2 – BENDING LOAD MAGNITUDE AND NUMBER OF OCCURRENCE OF LESS FREQUENT EVENT FOR THE ORIGINAL CRANKSHAFT MODEL.	76
TABLE 5.3 – TORSION LOAD MAGNITUDE AND NUMBER OF OCCURRENCE OF LESS FREQUENT EVENT FOR THE ORIGINAL CRANKSHAFT MODEL.	76
TABLE 5.4 – STAIRCASE FATIGUE DATA OF THE ORIGINAL CRANKSHAFT FOR BENDING MOMENT. ...	77
TABLE 5.5 – STAIRCASE FATIGUE DATA OF THE ORIGINAL CRANKSHAFT FOR TORSION MOMENT. ...	77
TABLE 5.6 – LOAD MAGNITUDE AND NUMBER OF CYCLES FOR THE FIRST TORSION TEST OF THE ORIGINAL CRANKSHAFT MODEL.	77
TABLE 5.7 – MEAN FATIGUE LIMIT CALCULATION FOR THE ORIGINAL CRANKSHAFT MODEL.	78
TABLE 5.8 – BENDING MOMENT MAGNITUDES AND NUMBER OF CYCLES OF THE LIGHTWEIGHT CRANKSHAFT SPECIMENS.	78
TABLE 5.9 – TORSION MOMENT MAGNITUDES AND NUMBER OF CYCLES OF THE LIGHTWEIGHT CRANKSHAFT SPECIMENS.	79
TABLE 5.10 – BENDING MEAN FATIGUE STRENGTH CALCULATED FROM NUMERICAL AND EXPERIMENTAL CALIBRATIONS OF THE ORIGINAL AND LIGHTWEIGHT CRANKSHAFT MODELS.	79
TABLE 5.11 – TORSION MEAN FATIGUE STRENGTH CALCULATED FROM NUMERICAL AND EXPERIMENTAL CALIBRATIONS OF THE ORIGINAL AND LIGHTWEIGHT CRANKSHAFT MODELS.	80
TABLE 5.12 – NUMERICAL FATIGUE RESPONSE FOR THE ORIGINAL CRANKSHAFT MODEL.	88
TABLE 5.13 – NUMERICAL FATIGUE RESPONSE FOR THE LIGHTWEIGHT CRANKSHAFT MODEL.	91
TABLE 5.14 – NUMERICAL FATIGUE STRENGTH FOR THE LIGHTWEIGHT AND ORIGINAL CRANKSHAFT SUBJECTED TO THE BENDING VIBRATION MODE.	91

CONTENTS

1. INTRODUCTION	16
1.1 Internal combustion engines	16
1.2 Resonant fatigue test	17
1.3 Historical introduction to crankshafts	19
1.4 Literature Review	21
1.5 Objectives	25
1.6 Dissertation organization	26
2. DESIGN OF A LIGHTWEIGHT CRANKSHAFT	27
2.1 Mass reduction analyzes	28
2.2 Four-cylinder engine crankshaft balancing	35
2.2.1 Effects of mass reduction on balancing	37
3. RESONANT FATIGUE TORSION TEST RIG	39
3.1 Torsion test rig	39
3.1.1 Inertia plates	42
3.1.2 External sleeves.....	43
3.1.3 Internal sleeves	43
3.1.4 Shafts.....	44
3.1.5 Fixed support.....	45
3.2 Modal analyses and harmonic response	45
4. FATIGUE TEST CALIBRATIONS	51
4.1 Static calibration	51
4.1.1 Strain gage positioning.....	52
4.1.2 Static calibration setup.....	53
4.1.3 Static calibration simulation.....	55
4.1.4 Static calibration results.....	57
4.2 Dynamic calibration	61
4.2.1 Dynamic calibration setup.....	61
4.2.2 Dynamic calibration procedure.....	65
4.2.3 Numerical dynamic calibration	66
4.2.4 Dynamic calibration charts.....	68
5. CRANKSHAFT FATIGUE TEST.....	71

5.1	Fatigue test procedure	71
5.2	Staircase method	72
5.3	Dixon-Mood data reduction model	73
5.4	Crack analysis	80
5.5	Numerical fatigue analysis	86
6.	CONCLUSIONS	93
	REFERENCES	94
	APPENDIX A – TEST RIG COMPONENTS DRAWINGS	97

1. INTRODUCTION

The current global model of strong competition faced by industries has promoted the search for innovation and optimized processes. Aiming to reducing production costs and increasing competitiveness, many tools have been developed in the most diverse industrial fields. In this context, Computer Integrated Manufacturing tools (CIM) have been used for controlling of manufacturing processes. Computer Aided Design (CAD) and Computer Aided Engineering (CAE) tools have been used in the design of new products using geometric modeling and numerical simulations. Numerical simulations enable an expressive reduction of time and costs in the development of new components and reduce the risk of design flaws.

In the automotive industry, CIM tools are used in the development of lighter components to improve the efficiency of engines and decrease the emission of pollutants. This chapter introduces the main features of crankshafts, a component of interest in the automotive industry due to its important role in combustion engines. The internal combustion engines (ICE), crankshafts and fatigue tests are also presented in this chapter, followed by a brief historical introduction to crankshafts and the definition of the objectives of this work.

1.1 Internal combustion engines

Internal combustion engines are thermal machines that convert the chemical energy of a fuel into mechanical energy while the pressure of the combustion gases expands in the chambers. The ICE can be classified according to the way the work is obtained. In rotary engines, the work is directly obtained by a rotating motion, such as the Wankel engine. On the other hand, reaction engines generate work by means of the thrust of gases expelled at high speed by the engine (example: jet engine). In reciprocating engines, which is covered in this work, the linear motion of pistons is converted into work for by means of the crankshaft and connecting rod system (VILLALVA; JUNIOR, 2010). Although this kind of engine is mostly related to the propulsion of vehicles (automobile, ship, airplane or locomotive), it can also be used as stationary engines to drive generators or pumps (PULKRABEK, 1997).

The crankshafts used in reciprocating engines are shafts with complex geometry and usually made of cast iron or forged steel. Figure 1.1 shows an example of a four-cylinder engine crankshaft and its main components. In internal combustion engines, the main journal is supported by the engine block. The crankshaft motion is achieved by the connection between

the crank pins and connecting rods. The crankwebs have structural and balancing function and the crankthrow is defined by the sequence of two main journals with a crankpin (MORAES, 2017).

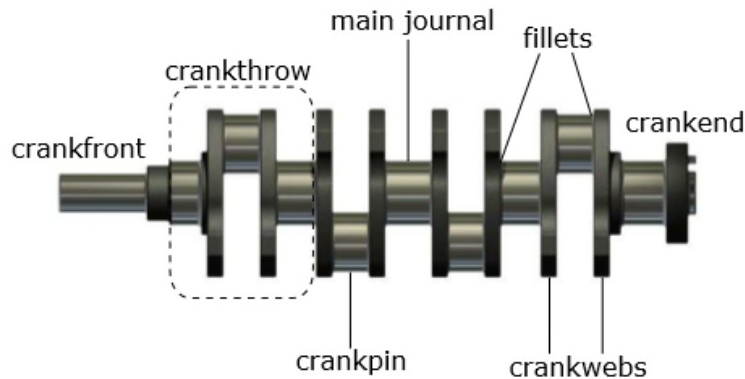


Figure 1.1 – Schematic drawing of a four-cylinder crankshaft (MORAES, 2017).

Under the combustion cycles, the crankshafts are subjected to torsion and bending dynamic loads. Due to the high stress concentration, the fillets of the crankpin and main journal are the most critical regions for crack nucleation. In order to increase the fatigue life of crankshafts, automotive industries induce residual compressive stress on the fillets of crankshafts by nitriding, shot-peening, fillet induction hardening or deep rolling processes. Even though the torsion loads are less intense than the bending ones, the lubricating oil holes are also critical for crack nucleation, especially in diesel ICE (FONSECA, 2015).

Aiming at improving the efficiency of ICE, automotive companies have been investing in the development of optimized crankshafts with mass reduction and application of lower density materials. The development of new crankshaft models, however, requires a reliable assessment of fatigue life. Currently, the resonant fatigue test is the most common experimental method used by companies to evaluate the fatigue strength of crankshafts subjected to bending and torsion loads.

1.2 Resonant fatigue test

The fatigue evaluation of new materials must be carried out by considering the worldwide standards of testing and characterization methodology. For this reason, the fatigue tests are always performed with polished and controlled specimens to obtain the stress-life diagram (S-N diagram). The S-N diagram of any material is universal and the fatigue limit, if existing, is represented by a knee in the curve. Furthermore, a database can be created and

used in numerical simulations for predicting of any risk of fatigue failure.

However, all residual stress introduced in the material will make the S-N diagram useless, since the material properties are modified in the treated regions. Thus, the fatigue behavior of materials subjected to welding, thermal residual stress or plastic deformation can not be directly estimated by the standard S-N diagram.

Taking into account the fact that most of the designed components are subjected to residual stresses from the manufacturing processes, the fatigue limit of manufactured components is usually different from most of the S-N diagram. For fatigue tests of mechanical parts, the fatigue life is arbitrary and has a statistical nature (LEE, 2005). In the case of crankshafts, the fatigue limit is usually defined as 2, 5 or 10 millions of cycles (MORAES, 2017).

Even though many techniques have been developed for fatigue tests of crankthrows, the resonant test method is the most used in the industry, since it requires low amplitude of input loads and short test time (CHIEN et al., 2005; VILLALVA; JUNIOR, 2010; MORAES, 2017). This procedure works by the application of bending or torsion loads in a resonant mode of vibration. The resonant test rig consists of two inertia plates and two pairs of sleeves fixing the crankthrow. The inertia plates are driven by an electrodynamic shaker and the resonance frequency is tracked by an accelerometer. A scheme of the bending test setup is shown in Figure 1.2. The resonance frequency highly depends on the mass and stiffness of the tested system. The crack propagation in the material decreases the structural stiffness and changes the harmonic response. The decrease in the resonance frequency then can be tracked and related to crack propagation (GUDMUNDSON, 1982).

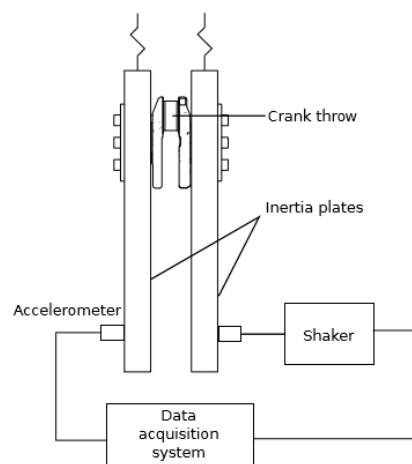


Figure 1.2 – Setup for the bending resonant fatigue test. Available from (MORAES, 2017).

1.3 Historical introduction to crankshafts

It is known that the technological advances obtained in the industrial age left a mark in the mankind history. In the 18th and 19th centuries, the first industrial revolution and the steam engine invention stimulated the development of many technologies that made the means of production faster and the transportation easier. The first internal combustion (IC) engine also began to be developed at this period and became indispensable in the industrial field ever since.

Great advances also occurred in engineering during this age. Dynamic loads were applied to structures and the fatigue phenomenon appeared for the first time. The early half of the 1700s is marked by catastrophic accidents caused by rupture of shafts and derailment of locomotives (NORTON, 2013). The search for the cause of these accidents led to the discovering of the fatigue phenomenon and great advance in the science of materials was reached at that time. Figure 1.3 shows the sketch of a locomotive shaft from the 18th century and the crack representation on the fillets of a crankpin.

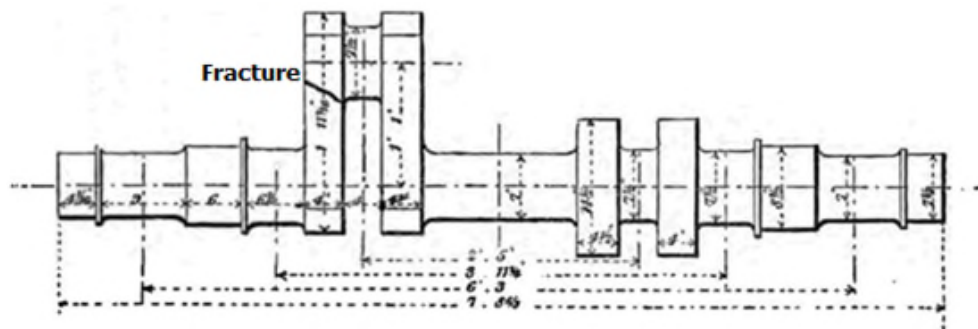


Figure 1.3 – Sketch of a locomotive shaft from the 18th century. Modified from (SIMÕES, 2012).

The resemblance between a locomotive shaft from 1800s and a present crankshaft is evident. One could notice that the crack initiation of those shafts is located on fillets with high stress concentration, which is also observed in crankshafts. These historical facts, however, highlighted the importance of studying the fatigue phenomena. Unfortunately, the discovery of new phenomena in engineering usually comes along with disasters that left marks in the history. One of these tragedies happened in 1842 after the birthday party of the king Louis Philippe, in Versailles. Figure 1.4 shows the A. Provost interpretation of the Versailles rail accident, also known as “Catastrophe ferroviaire de Meudon”. Nowadays his work is located in the Sceaux castle, in France (SIMÕES, 2012).



Figure 1.4 – A. Provost interpretation of the Versailles rail accident.

The rail transport, however, was considered very safe at that time and the particular accidents did not prevent the railway expansion in many countries around the world since 1820. At the same time, modern internal combustion engines were being developed along with the self-propelled vehicles (PULKRABEK, 1997).

The first engines developed in the 17th and 18th centuries can be classified as atmospheric engines. They were large single piston engines with a cylinder opened to the atmospheric pressure. This kind of engine works with a differential pressure generated across the piston between the vacuum formed by the cooled combustion gases and the atmospheric pressure (PULKRABEK, 1997).

The earlier prototypes of self-propelled road vehicles date from 1600s. However, most of them were driven by steam and never became practical operating vehicles. At that time, the evolution of the modern automobile was restricted by the technology, materials, roads and fuels. In 1859, the crude oil discovery in Pennsylvania aroused the search for more reliable fuels to be used in the new developing engines. Before that time, the usage of whale oil, coal gas, mineral oils and gun powder as fuel did not enable a good performance of engines. Even though it took many years to the petroleum industry evolve the first crude oil into gasoline, improved hydrocarbon products started to appear about 1860s and the internal combustion engine evolved together (PULKRABEK, 1997).

The pneumatic rubber tire developed by John B. Dunlop in 1888 was another invention that stimulated the emergence of internal combustion engines. After that, the

automobiles became much more desirable and boosted the propulsion system market. Influenced by Etienne Lenoir (1822-1900), designer of the first executable internal combustion engine, Nicolaus A. Otto (1832-1891) built the first prototype of a four-stroke engine in 1876. It was also the first time the crankshaft and connecting rod appeared in a combustion engine. Four years later, the motor presented by Otto was being used in automobiles (VILLALVA; JUNIOR 2010). In 1886, Karl Benz (1844-1929) developed a three wheel vehicle with one cylinder engine and counterweight in crankshafts to improve the balancing of the engine. The crankshafts of these engines were made of forged steel and subjected to quenching and tempering heat treatment (VILLALVA; JUNIOR, 2010).

Along the First World War (1914-1918), the high strength alloy steels were heavily used in the war industries. The consequent missing of material to the production of crankshafts increased the application of non alloyed steels hardened by carburizing. At that time, the four-stroke vehicles had critical problems with vibrations because the engine block had only two bearings supporting the crankshaft. Nowadays, the excessive vibration of the four-stroke engines is avoided by means of five bearings in the engine block and four or eight counterweights in the crankshafts (VILLALVA; JUNIOR, 2010).

After the 1950s, the usage of hydraulic press accelerated the forging process, which was previously executed using hammer. At that time, the foundry process evolution made possible to obtain cast iron with good mechanical properties for crankshaft application. Gradually the alloy steels were replaced by ferrite-pearlite structure steels with precipitation hardening. A great improvement was obtained later by increasing the number of bearings and using counterweights in the crankshafts. More recent research obtained higher fatigue limit in crankshafts applying residual stress in the fillets of crankpin and main journals by the deep rolling process (VILLALVA; JUNIOR, 2010).

1.4 Literature Review

One of the very first works about resonant fatigue tests in crankshafts was published by Jensen (1970). He instrumented V6 and V8 nodular crankshafts with strain gages for bending and torsion bridges and assembled them in a dynamometer engine to evaluate the dynamic loads applied to the crankshaft. Jensen (1970) verified that gas and inertial forces induced bending and torsion loads in the crankshaft. The bending loads had higher influence in the critical areas of the crankshaft than the torsion loads. Using a “tuning fork” test rig, Jensen (1970) obtained an S-N diagram for the nodular cast iron crankshaft subjected to

bending loading. The paper (JENSEN, 1970) based several works about fatigue tests in crankshafts (CHIEN et al., 2005; VILLALVA; JUNIOR, 2010; YU et al., 2004; SPITERI et al., 2005; SPITERI et al., 2007).

Montazersadgh and Fatemi (2007) performed a dynamic simulation in a single cylinder four-stroke engine. They showed that the maximum force applied to the crankshaft occurs when combustion takes place. At this moment, the force applied by the gas expansion is exactly toward the center of the crankpin and, therefore, the crankshaft is only subjected to bending load (MONTAZERSADGH; FATEMI, 2007). They also showed that the maximum force applied to the crankshaft decreases in higher rotations because of the balancing effect of the inertia forces.

Surface hardening has important role in the fatigue strength of crankshafts and is broadly explored in literature. One of the very first works about this topic was published by Kamimura (1985, apud MORAES, 2017). A direct relation between the rolling force applied to the fillets and the bending stress was derived for a ductile cast iron crankshaft. The rolled samples had fatigue strength increased from 191 MPa to 412 MPa. Grum (2003) showed the compressive nature of residual stresses in a 42CrMo4 steel forged crankshaft. This work evaluated the residual stress distribution after induction of surface hardening in the main bearing of the crankshaft with compressive stresses ranging from 1020 MPa to 1060 MPa at a depth of about 250 μm , dropping to about 800 MPa in a depth of 3.5 mm. A broad review of the deep rolling process is described by Fonseca (2015). He proposed a plastic transient finite element model to investigate the influence of fillet rolling in crankshafts. The fillet radii of rolled crankshafts showed good agreement with the deformation results of the numerical model.

The effects of surface treatments in the fatigue strength of crankshafts were also investigated in (PARK et al., 2001). This work compared the influence of nitriding and fillet rolling in carbon steel and microalloyed steel crankshafts. The fatigue tests showed that microalloyed steel has around 70% of carbon steel fatigue limit. The relationship between fatigue limit and fillet rolling force was also analyzed in this work. The specimens were fillet rolled with force of 500 kgf and 900 kgf and the fatigue limit were compared to the nitrided ones. Both fillet rolled with 900 kgf and nitrided samples showed more than 80% increase in fatigue limit. The fillet rolled with 500 kgf samples obtained improvement of 40% in the fatigue limit. To maximize the fatigue life of crankshafts, authors suggested optimum level of nitriding depth above 400 μm and fillet rolling force kept in a range of 700 to 900 kgf.

Williams and Fatemi (2007) compared the fatigue behavior of forged steel and

ductile iron materials for a one-cylinder engine. The two materials were compared by means of different methods. Specimens were machined from the crankshafts for monotonic tensile tests and strain-controlled fatigue tests. The results showed that the forged steel has greater ductility than the ductile cast iron. The ultimate strength obtained of cast iron was 80% of the forged steel. The fatigue tests at 10^6 cycles showed fatigue strength of 359 MPa for forged steel and 263 MPa for ductile cast iron.

Chien et al (2005) investigated the influence of residual stress induced by fillet rolling process in a cast iron crankshaft. They applied bending moment of 508.4 Nm in a two-dimensional plane finite element analysis to determine the stress distribution in the fillet of the crankpin. A residual stress was applied in an elastic-plastic finite element based on the fillet surface profile measured by shadowgraphs taken before and after the fillet rolling process. Chien et al. (2005) also assessed the fatigue process in the fillet rolled crankshaft by the four-bubble failure criterion, which determines failure when four pinhead-sized bubbles appear within 6.35 mm on the fillet surface. This work, however, concluded that the four-bubble criterion is too conservative, since it cannot indicate whether cracks will propagate or arrest in the plastic zone. For this reason, this failure criterion can only determine the crack initiation for small cracks nucleated in the fillet surface.

The theory of crack arrest in the fillet rolled regions was supported in (SPITERI et al., 2005). This study explored different failures criteria for fatigue in a ductile cast iron crankshaft. The stiffness change criterion was compared to surface cracks and two-piece failure ones. The specimens were monitored in a resonant bending test rig and the frequency shift was related to the number of cycles. They identified that 3% drop in the resonant frequency would represent 90% of the total accumulated cycles before fracture. The four-bubble criterion was found too conservative in agreement with (LEE; MORRISSEY, 2001), (CHIEN et al., 2005) and (SPITERI et al., 2007).

Gudmundson (1982) showed mathematically that eigenfrequencies of structures are affected by cracks due to stiffness shift caused by crack propagation in materials. Feng and Li (2003) showed the influence of cracks in the resonant frequency of fatigue test rigs for crankshafts. They also introduced the static and dynamic calibration principles that enabled an automated test control, making the fatigue test in crankshafts cheaper and more efficient. The concept of resonant frequency drops in notched crankshafts was studied in (YU et al., 2004). This work investigated the influence of notch depth on the drop of resonant frequency in a bending test rig. The notches ranging from 1 to 5 mm were introduced on the crankpin fillets of a cast iron crankshaft. The resonant frequency was obtained experimental and numerically

for each notched specimen and the results showed good agreement.

Moraes (2017) described the test procedures for fatigue assessment of crankshafts. A bending fatigue test rig was designed to perform fatigue tests in a rolled cast iron crankshaft. The fatigue tests were carried out according to the 3% resonant frequency shift criterion, which showed good accuracy for crack detection. The specimens were instrumented with linear strain gages in the center bottom of the crankpin and in the fillet radii for static and dynamic calibrations. The experimental and numerical analysis showed high stress concentration in the fillets of the crankpin.

The stress concentrations in the fillet radii and oil hole of automotive crankshafts were investigated in (VILLALVA; JUNIOR, 2010). This work compared numerical and experimental results for bending and torsion loads in symmetric and non-symmetric crankthrows. The specimens were instrumented with strain gages in the bottom center and in the fillet radii of the crankpin. In the numerical analysis, bending and torsion loads were applied to the main bearing of the crankthrow. The torsional analysis showed high stress concentration in the oil holes of the crankshafts, while the bending one highlighted the fillet radii as critical regions. These results were confirmed by the crack nucleation in the fatigue tests. Furthermore, numerical results showed good agreement with experimental measurements, with less than 1% deviation for 2.63 kNm bending moment. For the torsional tests, it was obtained a deviation of 4.52% for non-symmetric and 1.17% for symmetric crankthrows subjected to 5 kNm.

An optimization analysis of a forged steel crankshaft was conducted by Montazersadgh and Fatemi (2008). The geometry, material and manufacturing processes were optimized taking into account the cost, geometric constraints and manufacturing feasibility. They obtained the critical regions of a single cylinder of a four-stroke engine in a dynamic numerical analysis applied according to the engine assembling conditions. The locations subjected to low stresses in the finite element analysis were modified without affecting the fatigue strength. They obtained 18% weight reduction subtracting mass of the crankweb, crankpin and central shaft. These modifications increased the stress range in the critical locations by 7% with deflection rate under 15%. Authors also approached the benefits of the fillet rolling process in the fatigue strength of crankshafts and the advantages of using microalloyed steel as alternative material to the forged steel. The microalloyed steel can reduce the manufacturing costs of crankshafts, since the heat treatment process can be removed. These results are in agreement with the extensive literature review about fatigue performance evaluation, manufacturing processes and cost analysis of crankshafts summarized in

(ZOROUI; FATEMI, 2005).

In order to understand the influence of crankshaft counterweight in an inline-four cylinder engine, Rodrigues (2013) applied balancing methodologies to three different models of crankshaft. He subtracted mass from the original crankshaft by shrinking (model 1), removing (model 2) and drilling (model 3) the counterweights and investigated the influence of these modifications in the crankshaft static balancing, vertical displacement, main bearings loads, torsional vibration and dynamic analysis. These analyses pointed the drilling of counterweight as better modification for mass reduction purposes, since the small displacement of the center of mass softens the effects of the removed mass in the counterweights (RODRIGUES, 2013).

1.5 Objectives

The main objective of this work is to evaluate fatigue in a lightweight crankshaft model. To do that, this work intends to design a lightweight crankshaft prototype without affecting the balancing and fatigue strength of a commercial crankshaft. Both original and lightweight models will be experimental and numerically tested and the fatigue results will be compared. The development of new crankshaft models requires reliable bending and torsion fatigue assessments to assure the infinity fatigue life during operation. Designing a fatigue test rig for crankshafts is challenging because there are little information available about this kind of rig in the literature. For this reason, designing a resonant test rig for torsion fatigue tests is highlighted as a second objective of this work.

The lightweight crankshaft and the torsion test rig will be designed and tested numerically by CAD and CAE tools. The numerical analyses can provide valuable information about the dynamic behavior of the torsion test rig during the fatigue tests. Besides that, numerical structural analyses will be carried out to determine the influence of the mass subtraction in the loss of stiffness and stress distribution of the lightweight crankshafts. In the automotive industry, the development of new crankshaft models require high cost due to the fatigue tests. The domain of the numerical tools can be used to predict design flaws and reduce the number of specimens required in the approval of prototypes. For this reason, developing a numerical approach for fatigue analysis of crankshaft based on structural analyses stands out as the third objective of this work

1.6 Dissertation organization

This dissertation is organized in six chapters. Chapter 1 approached the introduction to internal combustion engines, fatigue tests of crankshafts and a literature review about this topic. Chapter 2 will discuss the numerical structural analyzes performed for mass reduction purposes and the influence of the mass reduction in the balancing and stress distribution of the crankshaft. Chapter 3 will show the main components of the torsion test rig designed in this work. The modal and harmonic response analyzes of the torsion test rig will be also discussed in Chapter 3. Chapter 4 will present the procedures used in the test calibrations of the bending and torsion rigs. Numerical and experimental structural analyzes will be described for the static and dynamic calibrations. Chapter 5 will show the procedures used in the fatigue tests and the statistical method applied to data reduction model. An approach for numerical fatigue analysis will be also presented in the end of Chapter 5. Chapter 6 will present the main conclusions of this work.

2. DESIGN OF A LIGHTWEIGHT CRANKSHAFT

The greatest challenges of the modern world are usually related to optimization problems. In the last years, the scientific discoveries about the aggravation of the environmental impacts caused by the current means of production have been raising concern among scientists around the world. In 2012, the United Nations (UN) had a conference about sustainable development placed in Rio de Janeiro, Brazil. This conference, known as Rio+20, launched the outcome document “The Future We Want” with a set of seventeen Sustainable Development Goals (SDGs) for people and planet prosperity. The 17 goals of the SDGs are shown in Figure 2.1.



Figure 2.1 – The seventeen sustainable development goals of the United Nations. Available from <https://sustainabledevelopment.un.org/sdgs>.

The 9th, 12th and 13th goals of SDGS are related, respectively, to innovation, efficiency and environmental protection. Sustainable development demands efficient processes capable to produce more and better, reducing waste and environmental impact. The research and development done by companies and universities have an important role in the achievement of these goals by the development of new materials and optimization of the means of production. In the automotive industries, the development of lighter engines leads to efficiency increase and reduction of carbon emission.

This chapter presents the criteria used in the design of a lightweight crankshaft. The lightweight crankshaft was designed based on the original dimensions of a commercial model. Static analyses were carried out in order to determine the stress distribution for bending and torsion loads. Balancing and loss of stiffness were verified considering the displacement of the center of mass and the vertical deflection. Specimens of both models (lightweight and original) were assessed in fatigue tests, which will be discussed in Chapter 4.

2.1 Mass reduction analyzes

Designing a lighter crankshaft from a commercial model is not an simple task. The complex geometry is subject to dynamic torsion and bending loads with high stress concentration regions that are critical for fatigue. Besides that, regular vehicle engines work in the range 1.000 – 5.000 rpm and require perfect balancing to avoid vibration problems. Therefore, balancing and fatigue strength are the major constraints for mass reduction in crankshafts. The loss of stiffness caused by mass subtraction is also an important constraint since the vertical deflection can raise vibration on the main bearings and lead to structural failures in the engine block. For these reasons, the mass reduction process performed by this work focused on balancing, fatigue life and vertical deflection constraints.

The nodular cast iron four-cylinder crankshaft evaluated in this work was supplied by an automotive company. The geometry is shown in Figure 2.2. The material properties of this crankshaft were evaluated by Moraes (2017) and are summarized in Table 2.1.



Figure 2.2 – Original crankthrow and crankshaft geometry.

Table 2.1 – Materials properties of the original crankshaft.

Young Modulus [GPa]	Yield stress [MPa]	Ultimate stress [MPa]	Poisson coefficient
177	400	708	0.275

The first concern in the mass reduction process is the structural failure. A numerical analysis is very useful to highlight the most critical regions and determine the parts that can be subtracted without considerable influence on the structural stiffness and fatigue strength. For this purpose, numerical structural analyses using Ansys software were conducted

in the original crankthrow model. An arbitrary bending load of 100 Nm was applied on the axial face of one journal, while the other one was constrained as fixed support, according to Figure 2.3. The mesh used has 231,726 quadratic tetrahedral elements and 351,928 nodes. The mesh close to the fillet radii requires high refinement due to high stress concentration in these regions. Therefore, the element size adopted was 0.5 mm in the fillet radii and 3 mm in the other regions. The mesh for the bending analysis is depicted in Figure 2.4.

The von Mises stress distribution of the bending simulation is shown in Figure 2.5. The highest stress concentrations are in the pin and journal fillets. These regions are highly affected for any structural modification on the crankshaft. The regions with dark blue color in Figure 2.5 are less sensitive for structural modifications and can be subtracted with lower influence in the global stiffness.

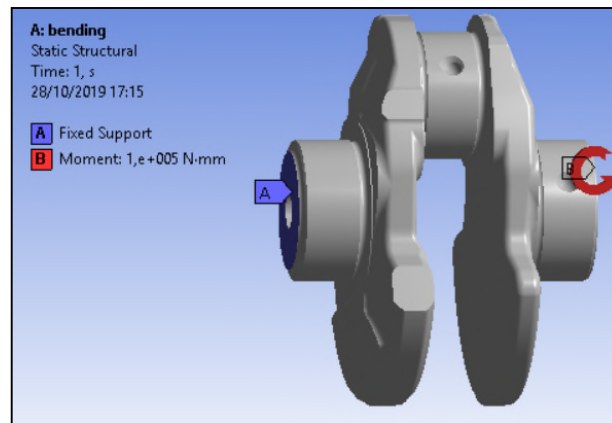


Figure 2.3 – Boundary conditions applied to the crankthrow for the static bending simulation.

A numerical analysis was also carried out for 100Nm torsion load and the crankthrow constrained similarly to the bending analysis. The axial face of one journal was constrained as fixed support and a torsion moment applied to the face of the other side, according to Figure 2.6.

In the torsion case, mesh requires higher refinement on the crankpin surface because the stress concentration in the oil hole has strong influence on the fatigue strength and crack nucleation. For this reason, the mesh has 302,796 quadratic tetrahedral elements and 471,252 nodes. The element size was 0.5 mm on the crankpin surface and fillet radii and 3 mm on the other regions. Figure 2.7 shows the mesh used in the torsion analysis.

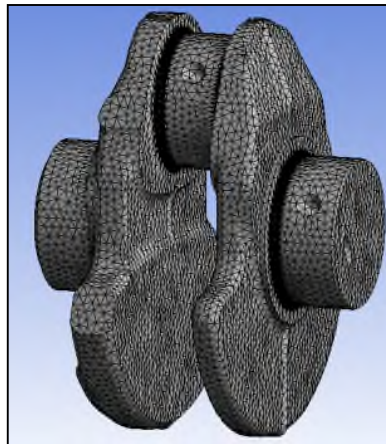


Figure 2.4 – Mesh used in the static bending simulation.

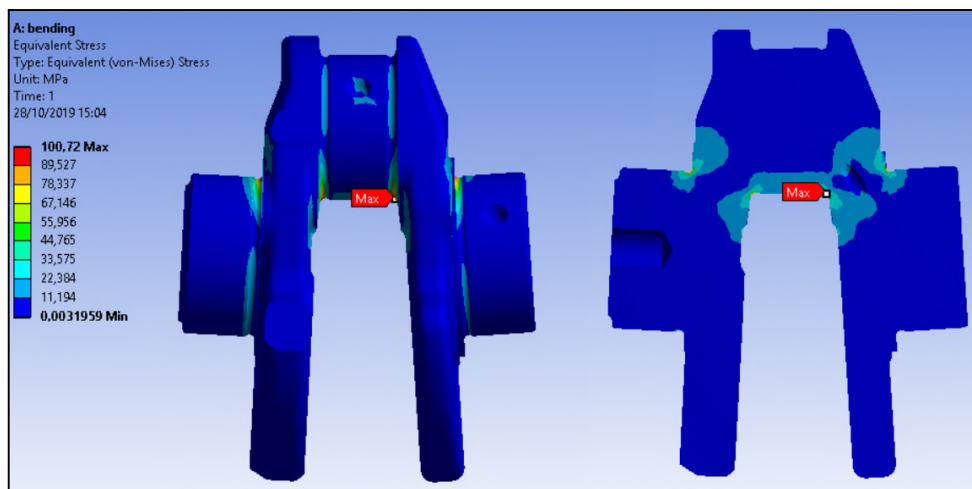


Figure 2.5 – Equivalent von Mises stress distribution for the static bending simulation.

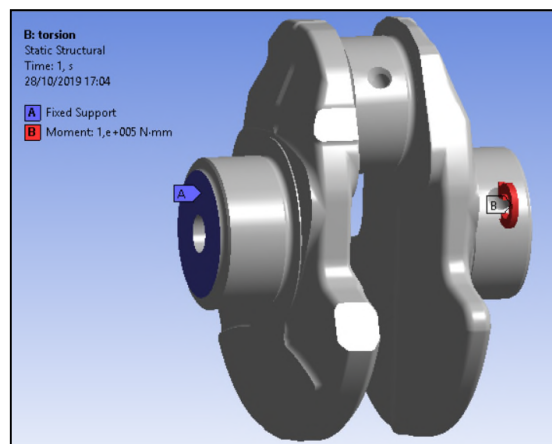


Figure 2.6 – Boundary conditions applied to the crankthrow in the static torsion simulation.

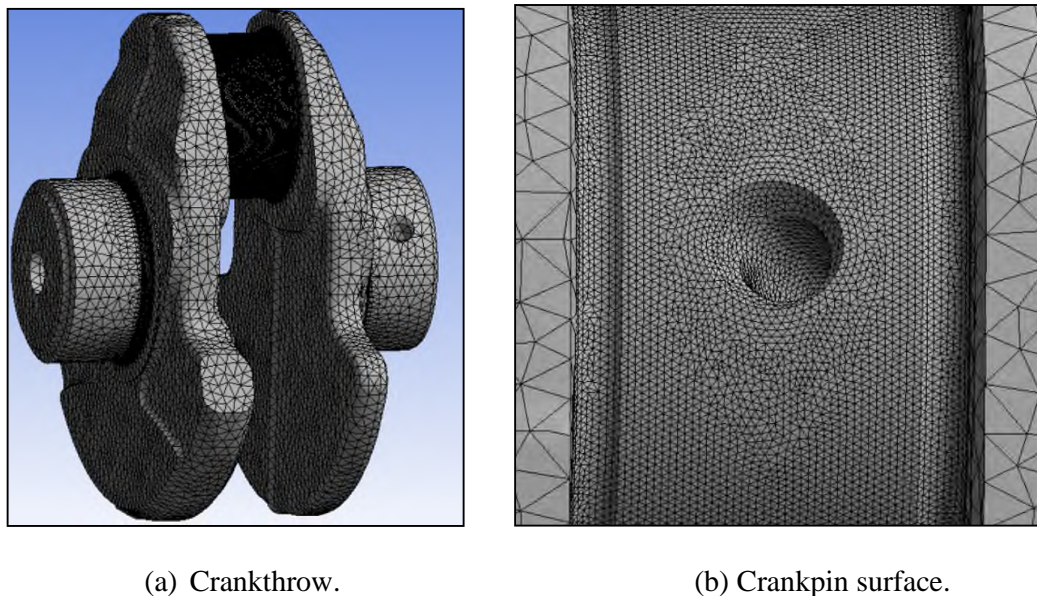


Figure 2.7 – Mesh used in the static torsion simulation.

The von Mises stress distribution of the torsion case is depicted in Figure 2.8. Under torsion loads, the maximum stress is located in the oil hole. The maximum stress obtained on the fillets, however, is very close to the maximum stress of the oil hole (about 26 MPa). It is important to highlight that the fillets of the crankshaft were subjected to deep rolling process to increase fatigue strength. For this reason, the oil hole is the most critical region for crack nucleation under torsion loads.

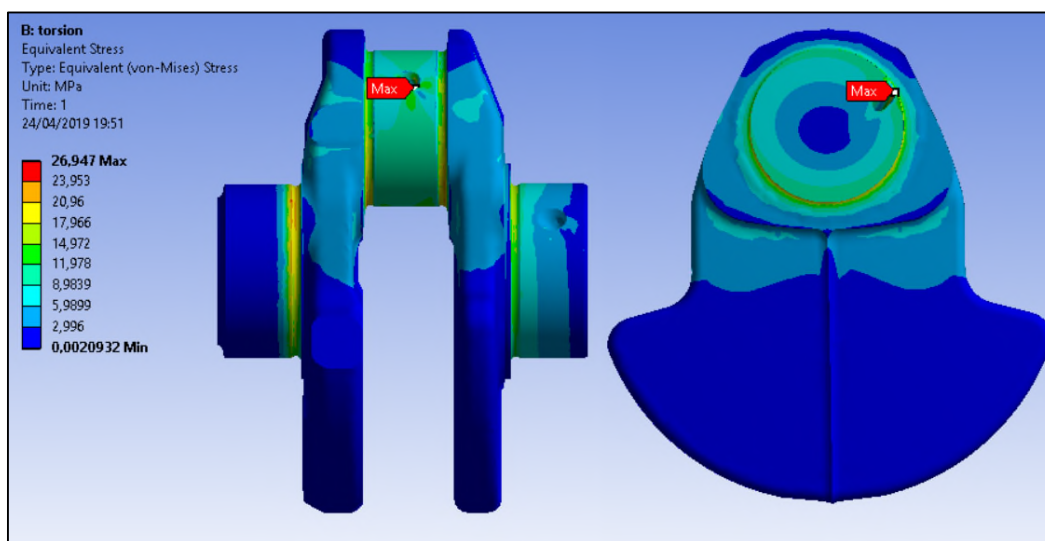


Figure 2.8 – Equivalent von Mises stress distribution for a static torsion simulation.

Both bending and torsion numerical structural analyses indicated that the counterweights has no contribution to the crankshaft stiffness. As expected since the counterweights have only balancing purposes in the crankshaft. It was also noticed that the inner region of the crankpin and main journals can be subtracted with low influence on the structural stiffness. However, both crankpin and counterweight modifications must be performed regarding the displacement of the center of mass to reduce the impact on balancing. For four-cylinder engines this process is not very critical since the crankshaft is symmetric and self balanced.

Furthermore, neither the crankpin nor the main journal bores can influence on the oil hole path and both modifications must be performed with caution to avoid linkage problems. For these reasons, three modifications were proposed for mass reduction process: $\text{\O}10\text{mm}$ pin bore (modification A), $\text{\O}10\text{mm}$ main journal bore (modification B) and $\text{\O}14\text{mm}$ counterweight drilling (modification C). These modifications are depicted in Figure 2.9.

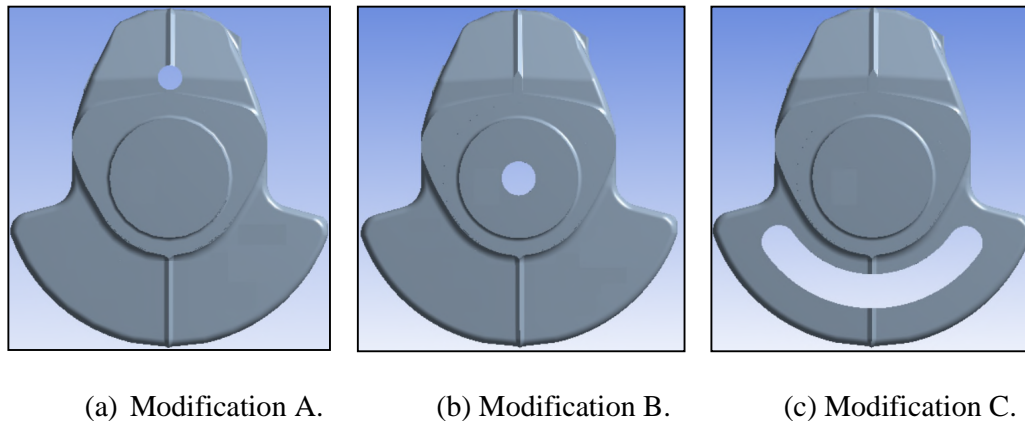


Figure 2.9 – Modifications proposed for mass reduction in the crankshaft.

The constraint adopted for performing the modifications in the original crankthrow was to maximize the mass reduction with minimum vertical deflection. Numerical static analyses were carried out to determine how each proposed modification would affect the vertical deflection of a single crankthrow. An arbitrary static force of 1000N was applied to the top of the crankthrow to simulate the vertical force from the connection rod on the crankpin. The main journals were constrained according to Figure 2.10. The structural analysis was performed to different prototypes related to the modifications A, B and C. The results for these different prototypes are summarized in Table 2.2.

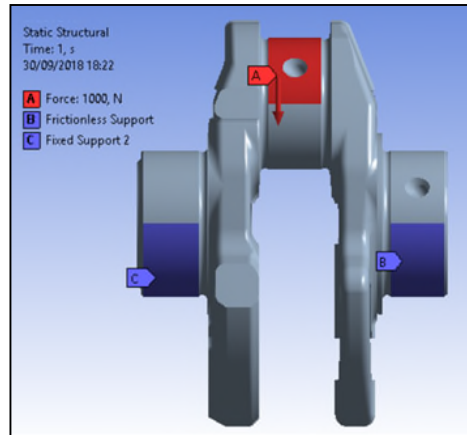


Figure 2.10 – Boundary conditions for static structural analyses considered for the mass reduction procedure.

The maximum mass reduction percentage was obtained for model II (about 12%), where the three proposed modifications (A,B and C) were applied simultaneously. However, the largest deflection (about 7.3%) was also obtained for this case. Comparing the results between models IV and V, we can observe that the main journal bore has stronger influence on the deflection than the crankpin bore. Furthermore, the mass reduction of the crankpin decreases the effects of the center of gravity displacement caused by the counterweight drilling. Therefore, the minimum center of gravity displacement was obtained in model IV. In addition, about 10% of mass reduction percentage and 2.6% of deflection rate were obtained for this model. For these reasons, model IV was selected as the best modification for mass reduction. A detailed sketch of the lightweight crankthrow is depicted in Figure 2.11, where dimensions are in millimeter. Figure 2.12 shows the 3D geometry for the respective lightweight crankshaft.

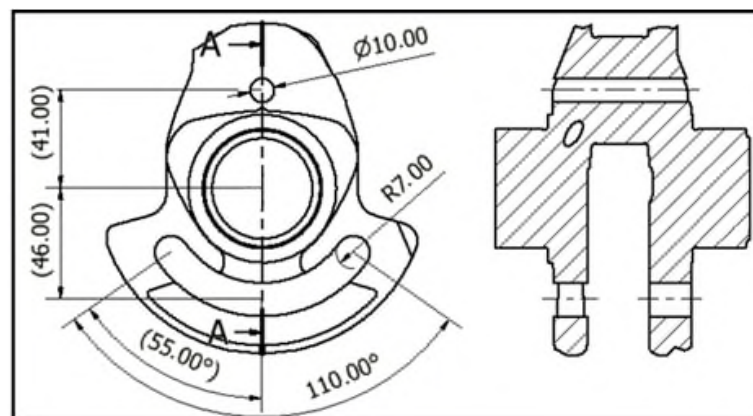


Figure 2.11 – Detailed sketch of optimized crankthrow.

Table 2.2 – Comparison of mass reduction effects in different crankshaft models.

Crankshaft	Model	Geometry	Mass [kg]	Mass reduction [%]	Vertical deflection $\times 10^{-4}$ [mm]	Vertical deflection [%]	Vertical CG [mm]
Original	I		3.2209	-	5.96	-	-1.30
A,B and C	II		2.8366	11.93%	6.39	7.26%	1.87
C	III		2.9409	8.69%	5.99	0.51%	2.25
A and C	IV		2.9087	9.69%	6.12	2.60%	1.82
B and C	V		2.8688	10.93%	6.27	5.19%	2.31



Figure 2.12 – 3D geometries of the lightweight crankthrow and crankshaft.

Even though the center of gravity is displaced from the center axis in a single crankthrow, the global center of gravity of the whole crankshaft presented no change due to the symmetrical positioning of the crankthrows. Furthermore, the inertia tensors (kg.cm²) for both models are almost diagonals, which indicates that both models are well balanced,

$$[I_{original}] = \begin{bmatrix} 204.31 & 0.19 & 1.08 \\ 0.19 & 1,623.48 & 0.04 \\ 1.08 & 0.04 & 1,558.52 \end{bmatrix},$$

$$[I_{lightweight}] = \begin{bmatrix} 177.76 & 0.19 & 0.62 \\ 0.19 & 1,485.88 & 0.04 \\ 0.62 & 0.04 & 1,433.01 \end{bmatrix}.$$

As can be seen from the previous inertia tensors, the moments of inertia of the lightweight crankshaft were reduced due the mass subtraction. The products of inertia, however, were slightly affected by the modifications in the geometry. The influence of the subtracted mass on the balancing and support bearing loads will be discussed in the Section 2.2.1.

2.2 Four-cylinder engine crankshaft balancing

Balancing analysis in crankshafts can be very complex and laborious task. In operation, the main bearings are subjected to inertia forces due to the reciprocating motion of pistons and rotation motion of crankshaft. Figure 2.13 depicts the vertical forces acting in a single cylinder engine. Force F_p acts on the piston along the cylinder axis to produce acceleration in the reciprocating masses. Inertia force F_a comes from the reciprocating motion of the piston assembly (piston, piston rings, piston pin and equivalent mass of the connection rod) and acts in the cylinder axis only. Force F_{cp} is the centripetal force acting on the crankpin due to its mass and the lower end of the connection rod mass in rotating motion. F_{cp} , therefore, is directed radially toward the center of the crankshaft, generating centripetal acceleration. A suitable counterweight with force F_{ct} can be added to the crankshaft to balance F_{cp} . In this case, F_{ct} and F_{cp} have the same magnitude, but opposite directions (RANGWALA, 2006).

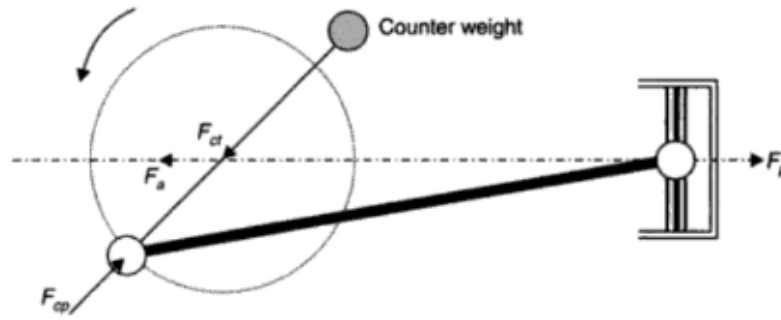


Figure 2.13 – Forces acting in a single cylinder engine (RANGWALA, 2006).

If F_{cp} is well balanced by F_{ct} , the only unbalanced vertical force is F_a , which have no side component. This force can be expressed as follows (RANGWALA, 2006):

$$F_a = -F_p = F'_a + F''_a = m_{rec}r\omega^2(\cos\theta + \frac{r}{L}\cos2\theta) \quad (2.1)$$

wherein r is the crank radius, L is the length of the connecting rod, θ in the crank angle from top dead center and ω is the angular velocity. The first term, F'_a , in Equation (2.1) is the first order inertia force and can be considered as projection on the cylinder axis of a virtual centripetal force, $m_{rec}\omega^2r$, generated by the reciprocating mass (m_{rec}) varying periodically once per shaft revolution. The second order inertia force, F''_a , can be considered as projection of the virtual centripetal force $\frac{r}{L}m_{rec}\omega^2r$, which is varying twice per shaft revolution (RANGWALA, 2006) (RODRIGUES, 2013).

The vertical inertia force acting on the bearings supports, in absence of counterweights, is given by:

$$F_v = F_{cp} + F_a = (m_{rot} + m_{rec})r\omega^2\cos\theta + m_{rec}\frac{r^2}{L}\omega^2\cos2\theta. \quad (2.2)$$

The influence of the inertia forces can be problematic for non-symmetric crankshafts, such as in straight-three cylinder engines. In the case of four-cylinder engines, however, the effects of the inertia forces are softened by the symmetry of the crankshaft geometry.

A crankshaft is said to be statically balanced when the sum of the vertical centripetal forces (F_{cp}) is zero, which is achieved when the center of gravity is in the rotation axis. The dynamic balancing requires that, for any point of the crankshaft, the sum of the moments generated by the centrifugal forces is null. The crankshaft, therefore, is well balanced

when these two conditions (static and dynamic balancing) are satisfied. Figure 2.14 depicts the vertical forces acting on a four-cylinder engine crankshaft.

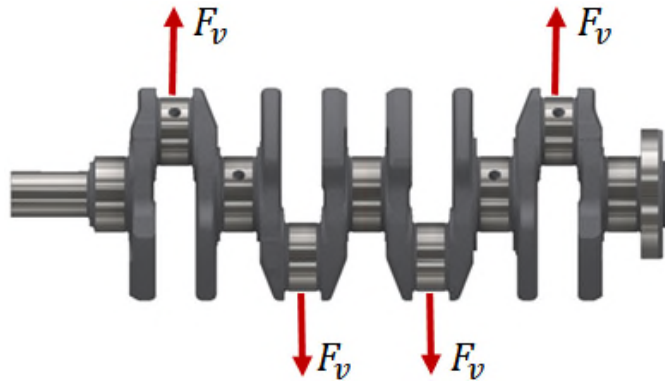


Figure 2.14 - Sketch of symmetrical vertical forces acting on the crankshaft.

In this case, there is a virtual plane of symmetry perpendicular to the rotation axis that divides the geometry into two mirrored parts, according to Figure 2.15. Due to the symmetrical positioning of the crankthrows along the shaft, the static and dynamic balancing requirements are automatically satisfied ($\sum F_{a'} = \sum F_{cp} = 0$ and $\sum M_{Fa'} = \sum M_{Fcp} = 0$). For these reasons, the four-cylinder engine crankshaft is said to be self-balanced. This particular characteristic indicates that counterweights would be unnecessary in this type of crankshaft. However, counterweights are usually used to decrease the effects of the two opposite binaries acting on the support bearings. The counterweight also contributes to minimize the effects of the vertical forces in a single crankthrow, minimizing the local vibration and reducing the loads on the support bearings (crankshaft internal moments).

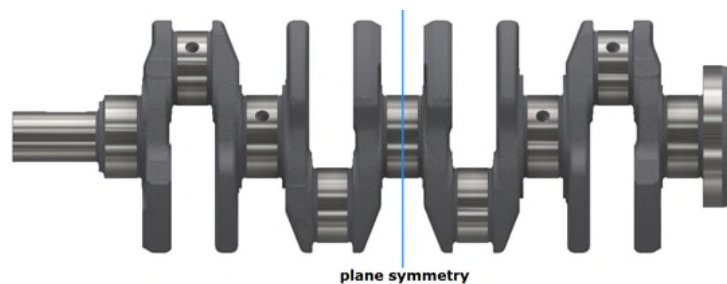


Figure 2.15 – Plane of symmetry in a four-cylinder engine crankshaft.

2.2.1 Effects of mass reduction on balancing

Even though the global balancing is guaranteed geometrically in a four-cylinder engine crankshaft, the mass reduction in the counterweight and crankpin can increase the

vibration on the support bearings due to the loss of stiffness and larger influence of the inertia loads. The numerical analysis indicated that the vertical deflection of a single crankthrow can increase 2.6% after the mass reduction modifications. The center of gravity, in a single crankthrow, is dislocated 1.82 mm from the center axis, which indicates that there is a local unbalancing that can be supported by the main bearings.

Rodrigues (2013) checked the influence of mass reduction of counterweights in the balancing of a four-cylinder engine crankshaft. Mass reduction of 14% was obtained by drilling the counterweights, according to Figure 2.16. Rodrigues (2013) verified that the resulting crankshaft was in according to ISO1940 (ISO1940, 2003) standard. However, the vertical force acting on the support bearings increased 24.12%, while the horizontal force increased 88.86%, disregarding the gas combustion force.

When the combustion force was considered, the vertical force was slightly reduced, since the inertia force of the counterweights acts in the same sense of the combustion load. These results indicate that the mass subtraction of counterweights is slightly beneficial for vertical force, but has a prejudicial effect on the horizontal direction. Even though the horizontal force is much lower than the vertical force, the support bearings has smaller resistance on the horizontal direction (RODRIGUES, 2013).



Figure 2.16 – 3D model geometry of the crankshaft modified by Rodrigues (2013).

In summary, the static numerical analysis indicated that the mass reduction performed in the crankshaft can increase the vertical deflection and increase the unbalancing of single crankthrow. The mass reduction can also increase the horizontal force on the main bearings. However, the results obtained by Rodrigues (2013) indicate that the lightweight designed in this work is in according to ISO1940 (ISO1940, 2003) standard, since the mass reduction in the counterweights is less aggressive than the one performed in the four-stroke crankshaft analyzed in (RODRIGUES, 2013).

3. RESONANT FATIGUE TORSION TEST RIG

The development of new crankshaft models requires major investment of the automotive industry. Before launching a new model, a prototype must be tested and approved by several technical standards to guarantee the quality of the product. The fatigue test procedures demand high costs related to runtime, energy consumption, specimen manufacturing and staff payment. Furthermore, the fatigue test of one specimen can take more than eight hours to reach the failure criterion. For this reason, the test frequency has an important role in the cost saving for experimental tests. The resonant fatigue test is the most used method for fatigue assessment of crankshafts in the automotive field. This method is characterized by high test frequency, low input loads and automatic crack detection.

The resonant test rig can be designed to operate in bending or torsion vibration modes. Even though the bending loads are critical in crankshafts (JENSEN, 1970), torsion fatigue can also occur, especially in diesel engines (FONSECA, 2015). However, the literature about torsion test rigs for fatigue evaluation is scarce. Most papers about crankshafts focus on bending fatigue procedures, application of new materials or influence of superficial treatments for increasing fatigue strength. In this work, a torsional test rig was designed and manufactured to evaluate fatigue strength in crankshafts. This chapter describes the main components of this equipment and the design methodology adopted in this work.

3.1 Torsion test rig

In internal combustion engines, crankshafts are subject to dynamic bending and torsion loads due to the combustion gas expansion in the cylinder chamber and the reciprocating masses of the cranktrain. In the long-term, these loads can lead a poorly designed crankshaft to present fatigue failures. For this reason, resonant test rigs are designed to apply high dynamic bending or torsion loads to determine the fatigue strength of prototypes. However, this method of fatigue evaluation in crankshafts is considered conservative, since the loads applied by the test rigs are fully reversed and larger than the real operation loads of the engine.

The resonant test rigs are designed taking into account two important aspects. The first one is related to the runtime. The test rig must be designed to operate in high frequencies to diminish the time of test and, consequently, the associated cost. The second concern is the required input load. Feng and Li (2003) showed that the mass of the inertia plates is inversely

proportional to the test frequency. However, if the mass of the inertia plates is too low, the system will require higher power to fatigue the specimens. In this work, numerical analyses were carried out to predict the resonant behavior of the torsional test rig and check the suitable equipments to drive the test.

Moraes (2017) designed a bending test rig composed of two inertia plates and two pairs of sleeves, according to Figure 3.1. The external sleeves are fixed in the inertia plate with strong interference fit. In the assembling stage, the specimens are firstly inserted in the internal sleeves. Then, the internal sleeves are fixed in the external ones by means of tightened bolts. This construction was used as reference for designing the torsion test rig.

While the bending test rig is suspended by wires, the torsion rig is suspended by fixed supports with roller bearings. This characteristic makes the torsional test rig more complex and expensive than the bending rig. The high loads required on the torsion tests demands larger inertia plates and more powerful electrodynamic shakers. Even though the torsional test rig is robust, its assembly is simple and practical. Similarly to the bending test rig, the external sleeves are fixed in the inertia plates with strong interference fit. The specimens and internal bearings are inserted in the internal sleeves, which are coupled to the external sleeves by tightened bolts, according to Figure 3.2. Then, the shafts are introduced in the internal bearings and the set is moved to the fixed supports. The roller bearings used in this project enable the rotation motion of the inertia plates, but constrain the translations. Both internal roller bearings (NU 1007 ECP model) and external roller bearings (NJ 2307 ECP model) are made by SKF Company.

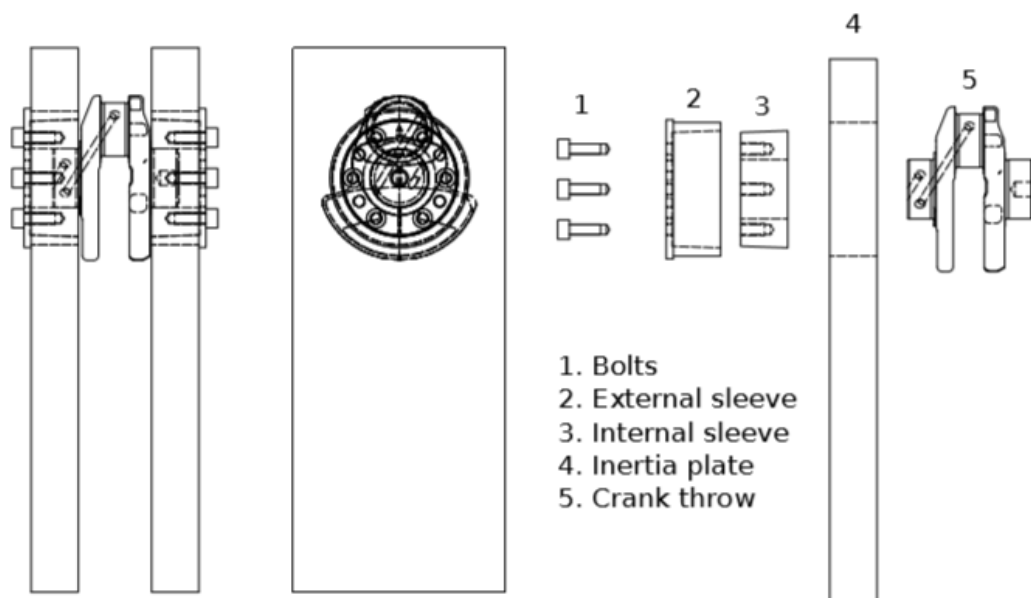


Figure 3.1 – Bending test rig components (MORAES, 2017).

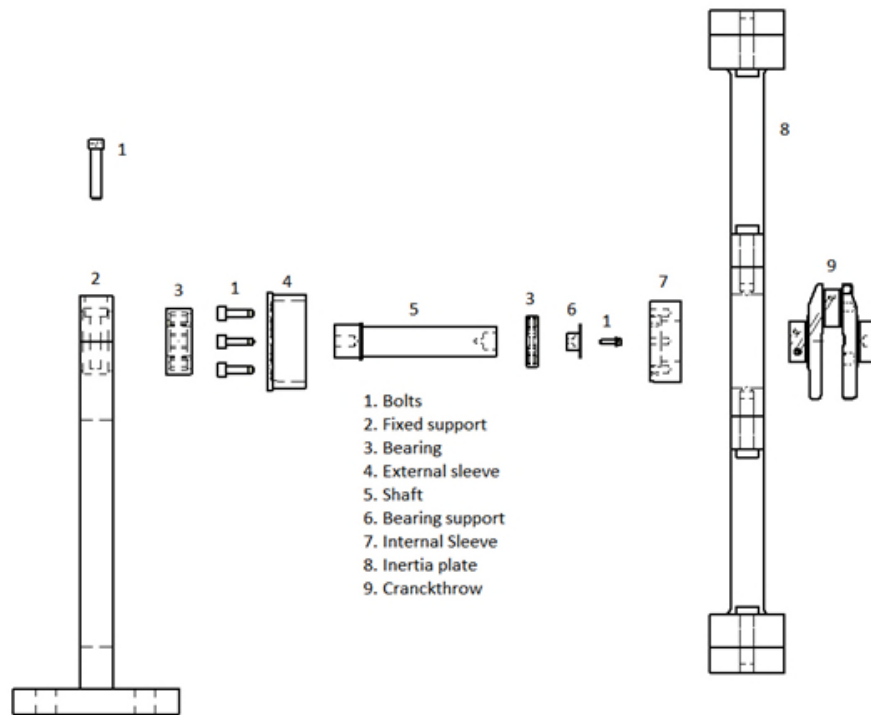


Figure 3.2 – Torsion test rig components.

Figure 3.3 depicts the 3D model of the torsional test rig. Figure 3.4 shows a comparison between the bending and the torsion test rigs. Detailed drawings of the torsion test rig components, with dimensions in millimeters, are included in Appendix A.

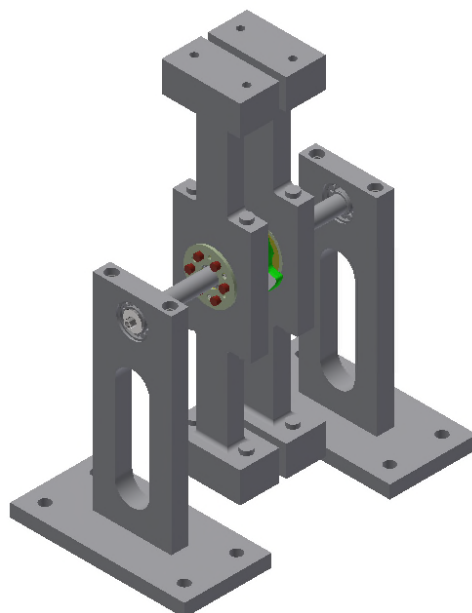


Figure 3.3 – 3D geometry of the torsion test rig.

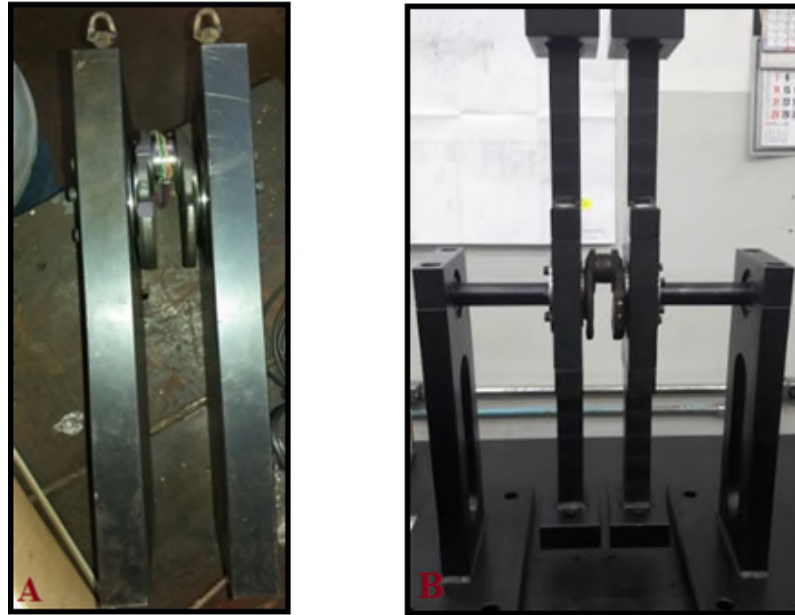


Figure 3.4 – (A) Bending and (B) torsion test rig.

3.1.1 Inertia plates

The inertia plates of the torsion test rig are larger than the bending ones due to the high loads required in the torsion tests. In this work, the inertia plates were split into three different parts to simplify the assembling process. Figure 3.5 shows the three components of the inertia plates, which are made of SAE 1045 steel.

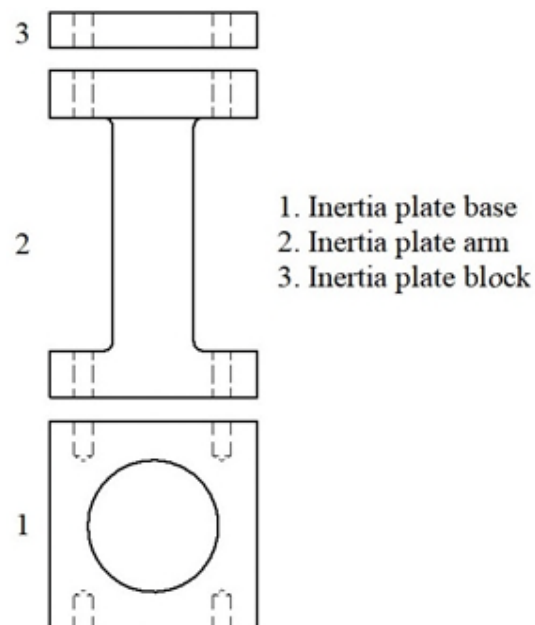


Figure 3.5 – Inertia plate components.

The length of the inertia plate arm has important contribution to the test frequency, since the moment of inertia is inversely proportional to the resonance frequencies. The dimensions of the inertia plates were designed to fatigue the original crankshaft in a frequency about 70Hz. However, higher or lower frequencies can be obtained depending on the crankshaft stiffness. The inertia plate blocks were added to the project to assure flexibility in the test, in such a way that higher loads and lower frequencies are obtained by the addition of blocks to the arms.

3.1.2 External sleeves

The external sleeve has an intermediate role in the coupling of the specimen in the inertia plate. It is permanently fixed in the inertia plate base by an interference fit of 0.126 mm. The internal surface of the external sleeves has 2 degree of conicity for coupling the conical internal sleeve in the structure. The friction between internal and external sleeves requires good wear resistance. For this reason, the external sleeves were made of SAE 4140 steel, carburized and quenched to improve the superficial hardness and fatigue resistance.

3.1.3 Internal sleeves

The internal sleeve is the most complex component of the torsion test rig. Its geometry is conical to make the coupling in the external sleeve stronger, in such a way that the specimen and the roller bearing are fastening whilst the internal sleeve get into the external one. Similar to the external sleeve, the application of this component requires high surface hardness and good wear resistance. Therefore, the internal sleeves were also made of carburized and quenched SAE 4140 steel. Figure 3.6 shows the assembly of the internal sleeve, internal roller bearing and crankthrow.

The internal sleeve requires extreme caution about the tolerance fits because no displacement is allowed between the sleeve and the specimen in operation. For this reason, the internal sleeves were manufactured with a gap to improve the fixation of the crankthrow. Figure 3.7 depicts the gap in the 3D geometry of the internal sleeve. This gap enables the internal sleeve to enlarge the internal diameter to accommodate the crankthrow and the roller bearing. At the same time, the internal diameter diminishes and tightens the crankthrow when the internal sleeve is forced through the conical coupling. The process of insertion of the internal sleeve in the conical coupling is done by six screws, which are fastened against the

external sleeve. Furthermore, the roller bearing must be introduced in the internal sleeves with high clearance fit; otherwise, the internal sleeve will tighten the roller bearing instead of the crankthrow and prejudice the fixation of the specimen.

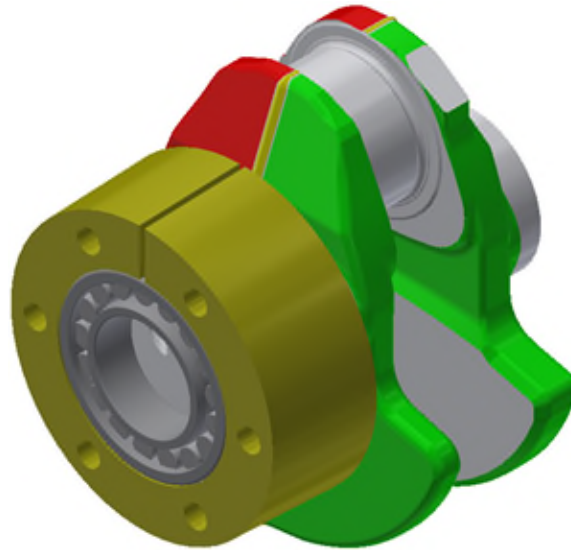


Figure 3.6 – Assembly of the internal sleeve, internal bearing and crankthrow.

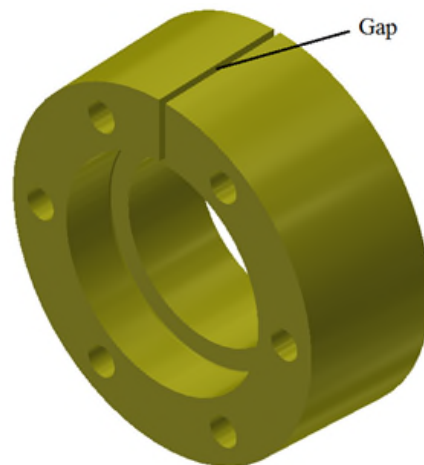


Figure 3.7 – Internal sleeve geometry.

3.1.4 Shafts

Instead of being suspended by wires, the torsional test rig is suspended by bearings that enable the rotation motion of the inertia plates. The connection between the internal and external bearings is made by the shaft, which is made of SAE 1045. The very ends of the shaft were designed to fit into the roller bearing placed in the internal sleeves and fixed supports.

3.1.5 Fixed support

The fixed support is split into two parts to accommodate the roller bearing in the assembling process. Both parts were made of SAE 1045 steel. The two parts of the fixed support are tightened by bolts to ensure that the shafts will not displace during the fatigue tests. The set of the fixed support parts and the roller bearing is depicted in Figure 3.8.

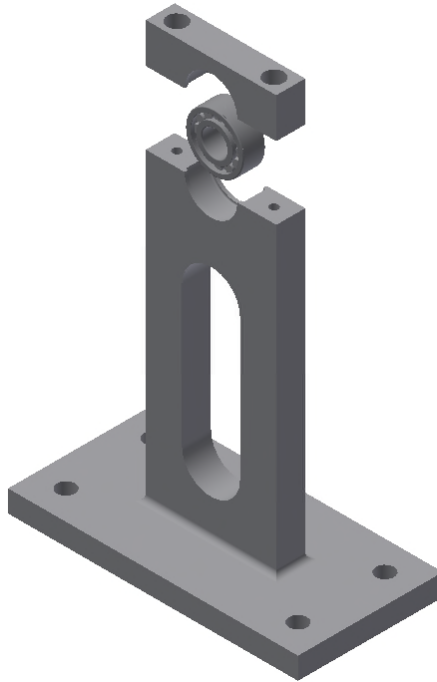


Figure 3.8 – Fixed support assembly in 3D geometry.

The fixed supports were designed with four bores in the bases for fixation purposes. The supports must be well aligned in a rigid platform; otherwise, the shafts will present offset problems in the assembling stage. The alignment issue can be solved whether the two supports are welded in the same base. In this work, however, the supports were made in different bases to make the project lighter and easier to transport.

3.2 Modal analyses and harmonic response

There is little information about the design of fatigue test rigs in the literature. Most of the papers about fatigue tests in crankshafts focus on failure criteria, test procedures or data correlation. Furthermore, if poorly designed, the test rig can present problems related testing time, specimen fixation and testing loads. For these reasons, designing a fatigue test rig

to operate in the resonant modes of vibration requires reliable CAE tools to prevent design flaws. In this work, modal and harmonic response analyses were carried out using ANSYS software to estimate numerically testing frequency and the input load of the prototype.

A numerical modal analysis indicated the modes of vibration and the associated resonance frequencies of the test rig prototype. This information was used in the designing stage to determine the test frequency of the torsion mode of vibration. To avoid expensive computational cost, the geometry of the prototype was simplified to reduce the number of elements and enable a reasonable computation time. For this reason, the influence of the screws, fixed support, rolling bearing and shafts were disregarded in the analyses. The geometry and mesh used in the modal and harmonic response analyses are depicted in Figure 3.9. The mesh has 366,765 quadratic elements and 535,382 nodes. Table 3.1 summarizes the element size used in the simulations. The structural steel material available in the Ansys Workbench library was used in all components of the test rig except for the crankthrow, which is made of cast iron whose properties are in Table 2.1. The material properties of the structural steel and the cast iron are shown in Table 3.2.

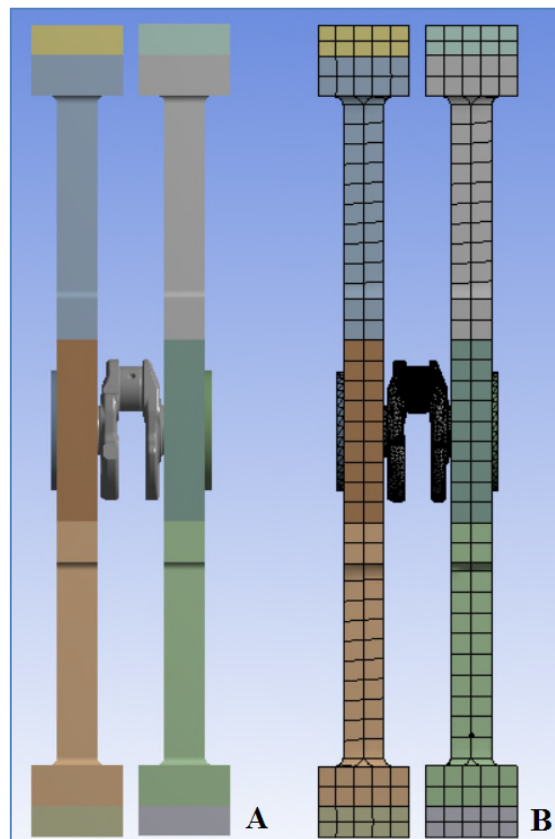


Figure 3.9 – Geometry (A) and mesh (B) used in the modal and harmonic response analyses.

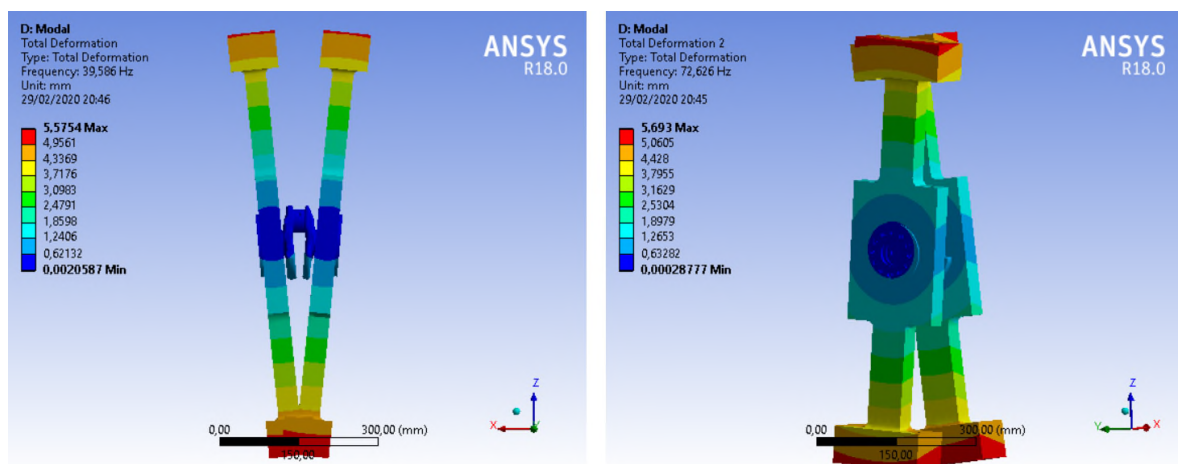
Table 3.1 – Element size used in the modal and harmonic response analyses.

Element Size [mm]	
Crankpin surface	2
Crankpin fillet	0.5
Oil hole surface	0.5
Inertia plates	20
Sleeves	10

Table 3.2 – Cast iron and structural steel material properties.

Property	Cast Iron	Structural Steel
Density [Kg/m ³]	7300	7850
Young Modulus [GPa]	178	200
Poisson ratio	0.275	0.300

The first six modes of vibration are related to rigid body motion with natural frequencies close to 0 Hz. Figure 3.10 shows the 7th and 8th modes of vibration, which are respectively the first bending and torsion modes. Taking into account the resonance frequency of the torsion mode and the failure criterion of 2 million cycles, the fatigue tests were estimated to perform in 8 hours.



(a) Bending mode – 39.586 Hz.

(b) Torsion mode – 72.626 Hz.

Figure 3.10 – Bending (a) and torsion (b) modes of vibration and respective natural frequencies.

The harmonic response analysis was carried out to determine the stress distribution in the crankthrow for an input load of 440 N, which is the maximum load specified for the Modal Shop 2100E11 electrodynamic shaker used in the experimental tests. In this analysis, the stress distribution strongly depends on the damping ratio of the rig. However, this information is not available in the designing stage. For this reason, the damping ratio of the torsional test rig was considered to be between 0.01 and 0.02.

The force was applied to the inertia plate arm at the distance of 300 mm from the center axis of the main journal of the crankthrow. The frequency response was analyzed by the acceleration on the opposite side of the force application, according to Figure 3.11. The model was solved in the frequency range of 72 to 73 Hz with 10 steps linearly spaced. The acceleration response for this range of frequency is depicted in Figure 3.12.

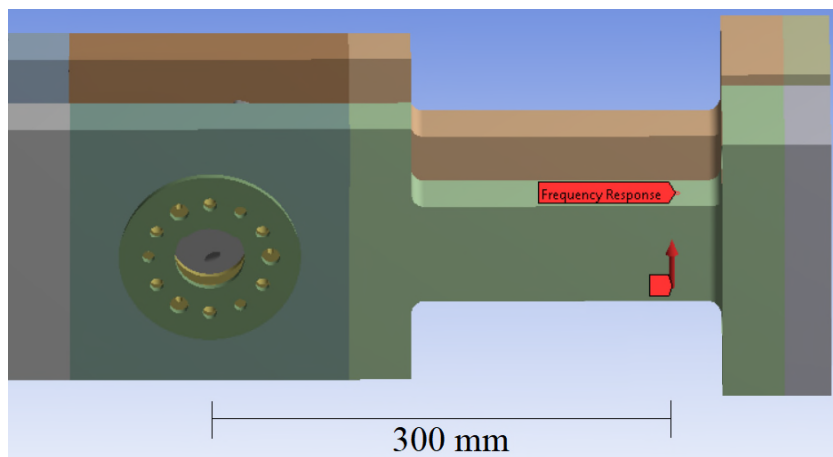


Figure 3.11 – Input force applied to the inertia plate in the torsion harmonic response analysis.

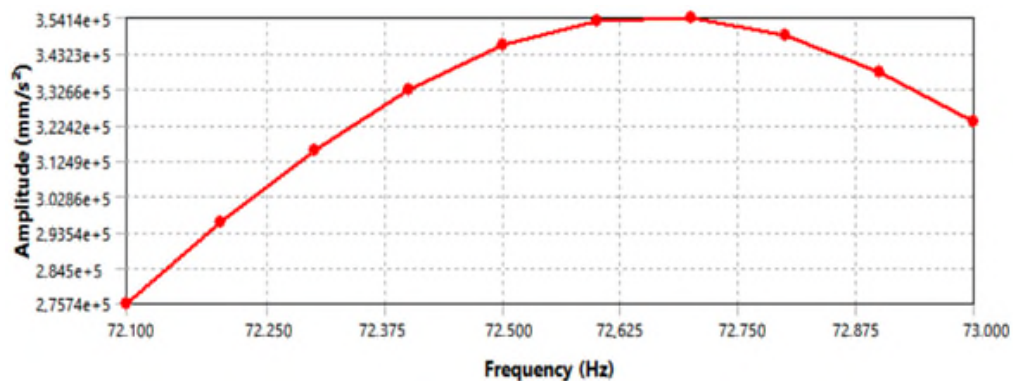
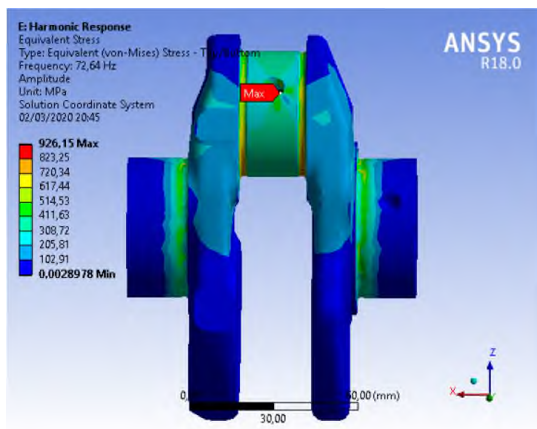
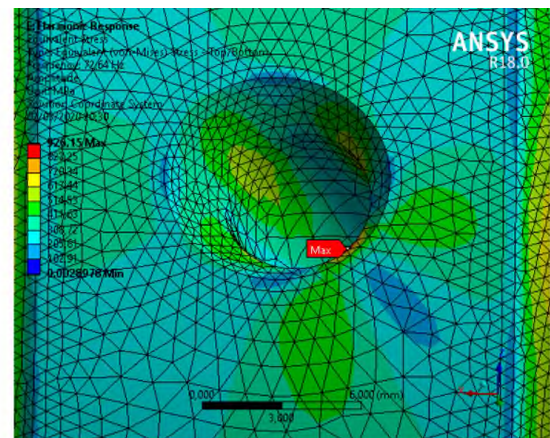


Figure 3.12 – Acceleration of the torsion harmonic response analysis for damping ratio of 0.01.

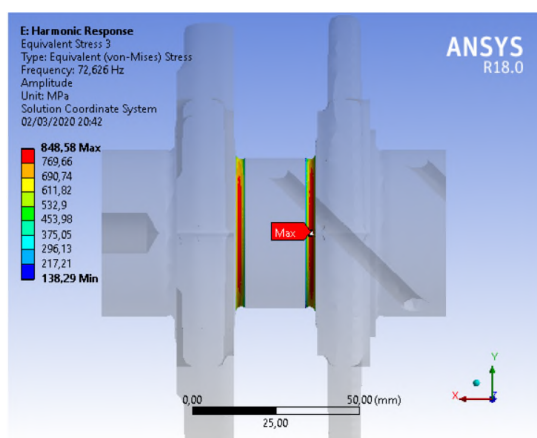
The acceleration and the von Mises stress of the most important regions of the crankthrow were stored for different values of the damping ratio. These results are summarized in Table 3.3. Figure 3.13 shows the von Mises stress distribution in different regions of the crankthrow for damping ratio of 0.01 and input force of 440 N. The harmonic response analysis pointed the oil hole as the critical region for crack nucleation in the fatigue tests. Considering the damping ratio varying from 0.01 to 0.02, the von Mises stress in the oil hole is in the range of 464 to 926 MPa. This result indicates how the maximum stress decreases by the damping ratio increment, in such a way that more powerful shakers are required to test higher damped systems.



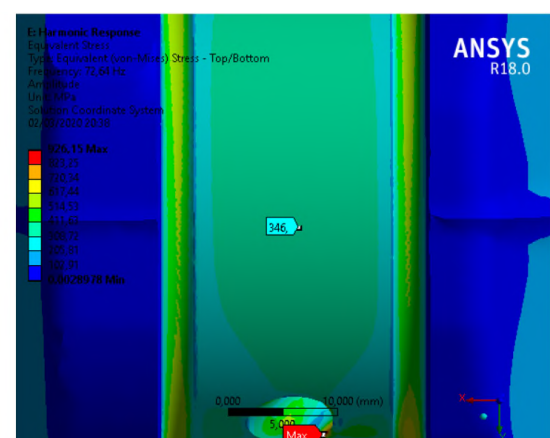
(a) Crankthrow – 926.15 MPa.



(b) Oil hole – 926.15 MPa.



(c) Fillet radii – 848.58 MPa.



(d) Center top of the crankpin – 346 MPa.

Figure 3.13 – von Mises stress results of the torsion harmonic response analysis for damping ratio of 0.01.

Table 3.3 – Torsion harmonic response analysis results for different values of damping ratio.

Force [N]	Damping Ratio	Acceleration [g]	Fillet radii [MPa]	Oil hole [MPa]	Center pin [MPa]
440	0.010	36.11	848.58	926.15	346.00
440	0.015	24.17	566.86	619.00	231.00
440	0.020	18.19	425.44	464.19	174.00

The relation between stress and damping ratio in a harmonic response analysis is linear, according to Figure 3.14. This relation is particularly important because enables the prediction of the dynamic behavior of the test rig, even though the damping properties are unknown. Therefore, the stress distribution in the specimens is numerically determined for any acceleration tracked experimentally by an accelerometer placed in the inertia plates. For this reason, the fatigue strength of the crankshaft can be expressed in terms of the maximum stress, dismissing the strain gages usage.

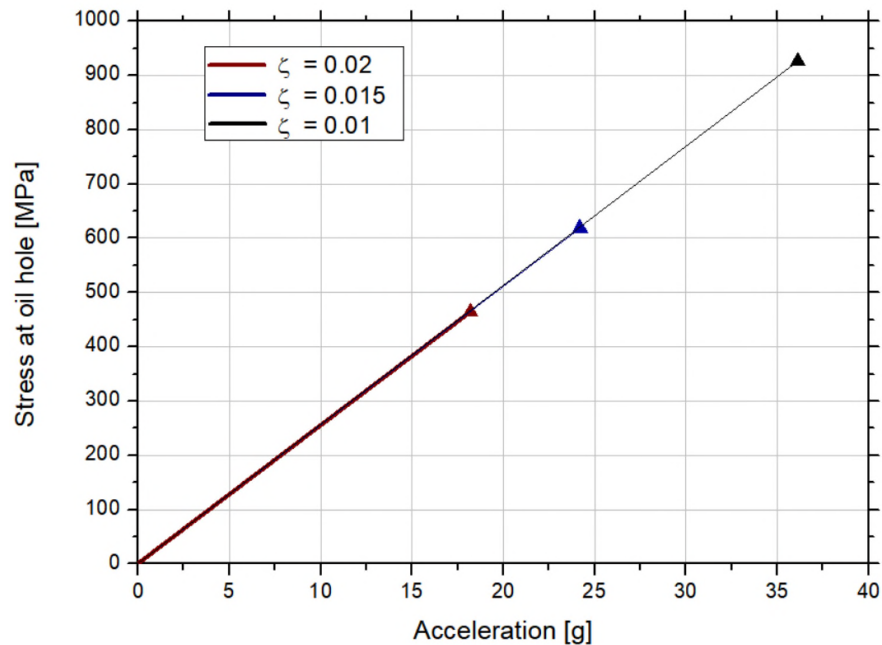


Figure 3.14 – Stress in the oil hole in terms of the acceleration response for different values of damping ratio.

4. FATIGUE TEST CALIBRATIONS

The fatigue strength of materials is usually expressed in terms of minimum admissible stress by number of cycles. However, the stress distribution of components of complex geometries is not easy to determine experimentally. In crankshafts, the imprecision of measurements in the fillet radii becomes a problem for comparison of fatigue strength among different models. Furthermore, there are crankshaft models in which the most critical regions are not accessible for measurements. For these reasons, expressing the fatigue strength in terms of the moment is more interesting for comparing different crankshaft models.

In fatigue tests of crankshafts, the relation between stress and the moment applied to the specimens can be derived from the static calibration. In the past, Jensen (1970) already used this procedure to determine the relation between the strain read by strain gages and the moment applied to the crankshafts. However, if only the static calibration is performed, then the fatigue tests will be controlled by the stress level in the crankshaft and all specimens will have to be instrumented. The time spent for instrumenting each specimen and the cost of the strain gages can make the fatigue tests very expensive.

The dynamic calibration proposed by Feng and Li (2003) made possible to control the fatigue test by means of one accelerometer placed in the inertia plate. After the dynamic calibration, the stress on the crankshaft is determined in terms of the acceleration given by an accelerometer, dismissing the use of strain gage. This procedure made the fatigue tests of crankshafts cheaper, since only the specimens subject to the calibration processes must be instrumented. In this work, numerical and experimental static and dynamic calibrations were carried out to obtain the relations between acceleration, stress and moment applied to the crankshafts. This chapter will discuss the details of the experimental and numerical calibration procedures.

4.1 Static calibration

The static calibration aims to obtain the relation between the strain on the crankpin surface and the moment applied to the specimen. Considering the properties of the material, it is possible to calculate the stress in the measured region for each bending or torsion moment applied to the crankthrow. Since the specimen is loaded in the elastic region, the static calibration results in a linear relation.

4.1.1 Strain gage positioning

In an experimental structural analysis, the strain gages are usually positioned in the most critical regions to detect the maximum stress of the specimens. This is because the maximum stress is an important parameter to evaluate the risks of structural failure. For bending loads, the finite element analyses indicated the fillet radii of the crankpin as the most critical region for crack nucleation. However, the little space available for positioning the strain gage on the fillet radii and the high stress gradients in this region influence the accuracy of the measurements. For this reason, the maximum stress was not used in the static calibration.

The relation between moment and strain must be linear for any region loaded in the elastic zone. Therefore, in the bending case, a KYOWA KFG-3-120-C1-11 3 mm strain gage was placed on the bottom center of the crankpin surface. This region is accessible in all specimens and enables a comparison between the two crankshafts considered in this work. The gages were lined up to the center line of the crankpin. The following relation was used to compute the stresses σ from the measured strain ε :

$$\sigma = \frac{E}{(1-\nu^2)} \varepsilon, \quad (4.1)$$

where E is the Young's modulus and ν is the Poisson's ratio of the material.

In the torsion case, a KYOWA KFG-3-120-D17-11 rosette gage was used to measure the strain in the static and dynamic calibrations. The rosette was positioned on the top center of the crankpin surface and lined up according to the principal stresses. Figure 4.1 shows the rosette gauge used in the torsion specimen. The principal stresses σ_1 and σ_2 of the plane stress state are given by

$$\sigma_1 = \frac{E}{(1-\nu^2)} (\varepsilon_1 + \nu\varepsilon_2), \quad (4.2)$$

$$\sigma_2 = \frac{E}{(1-\nu^2)} (\varepsilon_2 + \nu\varepsilon_1), \quad (4.3)$$

where ε_1 and ε_2 are the measured strains in the principal directions. The equivalent von Mises stress σ_v is calculated by

$$\sigma_v = \sqrt{\sigma_1^2 - \sigma_1\sigma_2 + \sigma_2^2}. \quad (4.4)$$

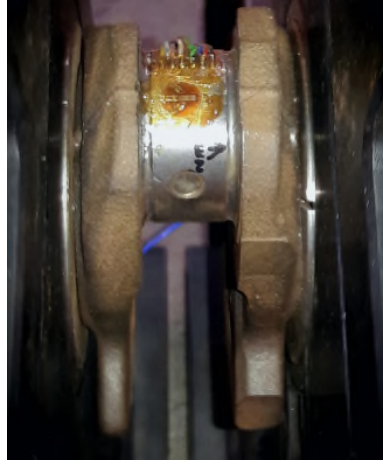


Figure 4.1 – Example of the rosette strain gage placement in a torsion crankshaft specimen.

Equations (4.2) and (4.3) can be used only when the principal directions are known. In the case of pure torsion moment, it is well known that the principal directions are rotated by 45° from the center axis. However, if the principal directions are unknown, then the following equation can be used to determine the principal stresses:

$$\sigma_{1,2} = \frac{E}{(1-\nu)} \frac{(\varepsilon_a + \varepsilon_c)}{2} \pm \frac{E}{\sqrt{2}(1+\nu)} \sqrt{(\varepsilon_a - \varepsilon_b)^2 + (\varepsilon_c - \varepsilon_b)^2} \quad (4.5)$$

where, ε_a , ε_b and ε_c are the rosette strains in the directions of 0° , 45° and 90° , respectively. It is important to highlight that, if the rosette is well positioned on the crankthrow, then the principal stresses calculated by Equations (4.2) and (4.3) and by Equation (4.5) must be the same. Therefore, the comparison between the von Mises stress from these equations is a good indicator for the rosette alignment.

4.1.2 Static calibration setup

The static calibration consists of applying an increasing bending or torsion moment in a specimen instrumented with strain gage to obtain the linear relation between stress and load. In the bending case, the test rig was placed over two supports and the inertia plate was loaded by a hydraulic jack, according to Figure 4.2. The test rig was loaded by an increasing force at a distance of 236 mm from the crankpin center line, bending the crankthrow fixed in the test rig. A HBM U10M 25kN load cell was used for tracking the force applied to the inertia plate. The signals from the load cell and strain gages were acquired by the HBM MGCplus data acquisition system and then input to the HBM Catman Easy software, wherein

each load signal was correlated to the respective strain measurement.

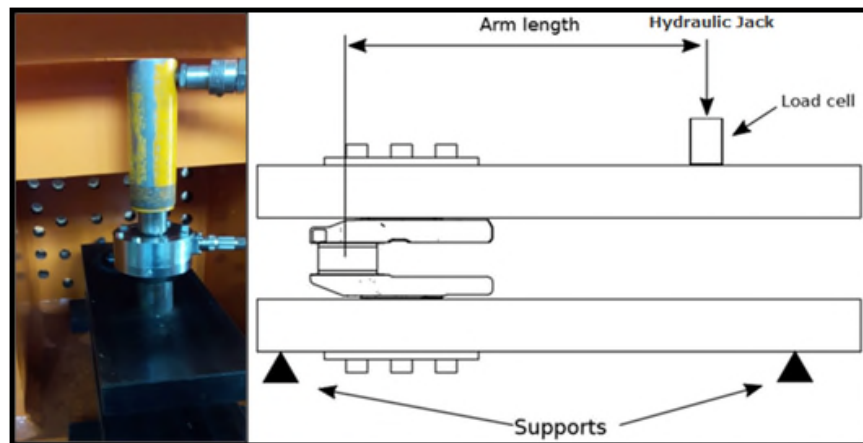


Figure 4.2 – Setup for the bending static calibration. Modified from (MORAES, 2017).

In the torsion case, the test rig was suspended by the fixed support. The load was applied to one of the bottom arms of the inertia plate, whilst the other one was fixed to prevent the rotation motion. The load was applied by a hydraulic jack at the distance of 350 mm from the main journal center line. The load cell and data acquisition system were the same for both bending and torsion calibrations. Figure 4.3 shows the setup used in the torsion static calibration.



Figure 4.3 – Setup of the torsion static calibration.

4.1.3 Static calibration simulation

Numerical analyses were carried out with the ANSYS software to simulate both bending and torsion static calibrations. In the bending case, the force was applied to one of the inertia plates at the distance of 236 mm from the crankpin center, similarly to the experimental calibration. The surface of the other inertia plate was set as fixed support, according to Figure 4.4 (A). All connected regions were set as “bonded” and the influence of the bolts was disregarded. The finite element mesh was build with 507,043 nodes and 352,659 quadratic elements. Table 4.1 summarizes the mesh parameters used in this simulation.

In the torsion case, the test rig geometry was constrained according to Figure 4.4 (B). Similarly to the experimental calibration, the inertia plates were connected to shafts with frictionless supports. The force was applied to one of the bottom inertia plate arms at the distance of 350 mm from the main journal center line, while the surface of the other one was set as fixed support. The very end of the shafts were modified to fit in the internal sleeve, replacing the roller bearing role in the structure. The modification performed in the very end of the shafts geometry is depicted in Figure 4.5. The interaction between the internal sleeves and the shafts were set as “no separation contact” to allow the tangential frictionless sliding. All other contacts between components were set as “bonded” in this analysis. The finite element mesh was build with 406,768 nodes and 265,755 quadratic elements. Table 4.2 summarizes the mesh parameters used in the torsion analysis.

Table 4.1– Mesh parameters for the bending static calibration.

Component	Element type	Element size (mm)
Inertia plate	Hexahedron	20.0
Sleeves	Tetrahedron	20.0
Crankthrow	Tetrahedron	5.0
Fillet radii	Tetrahedron	0.5

The strain gages used in the original and lightweight specimens of the bending case are linear, which means that only the strain on the crankpin centerline direction was measured. For this reason, the stress calculated by Equation 4.1 was not compared to the von Mises stress of the simulations, but the strain obtained in the simulation was used in Equation 4.1 to determine the correspondent numerical stress. Afterwards, the numerical and experimental stresses were compared in the calibrations charts. Figure 4.6 highlights the

bottom center stress for 700 Nm bending moment.

The torsion specimens were instrumented with rosette strain gage, which enables the determination of a plane strain state. In this case, the von Mises stress obtained by Equation 4.4 was directly compared to the results obtained numerically. For this reason, the top center stress of the crankpin was recorded for comparison purposes, according to Figure 4.7.

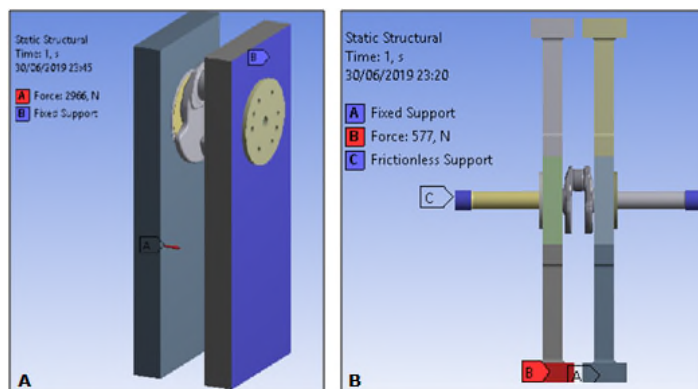


Figure 4.4 – Boundary conditions of the (A) bending and (B) torsion static calibrations.

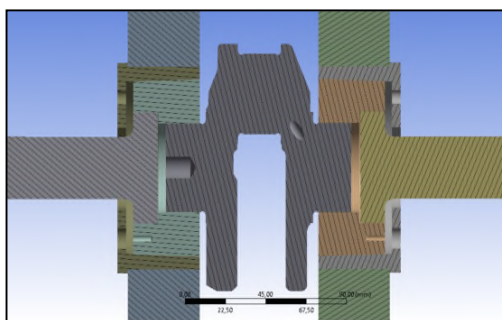


Figure 4.5 – Modified shafts assembled in the internal sleeves of the torsional test rig.

Table 4.2 – Mesh parameter for the torsion static calibration.

Component	Element type	Element size (mm)
Inertia plate	Hexahedron	15
Sleeves	Tetrahedron	20
Shaft	Tetrahedron	3
Crankthrow	Tetrahedron	5
Fillet radii	Tetrahedron	1
Crankpin surface	Tetrahedron	1

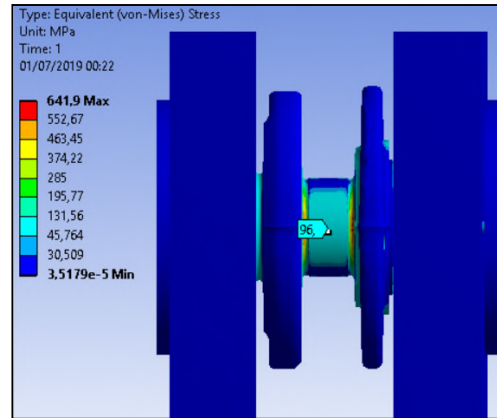


Figure 4.6 – Bottom center von Mises stress for 700 Nm bending moment.

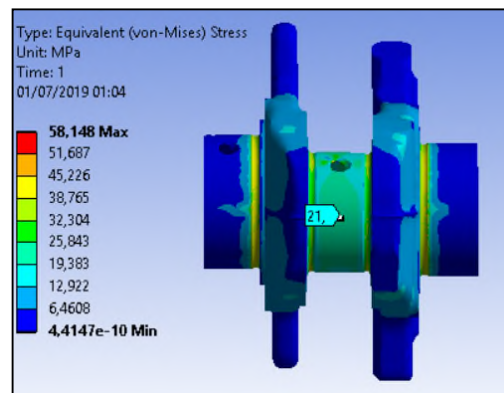


Figure 4.7 – Top center von Mises stress for 200 Nm torsion moment.

4.1.4 Static calibration results

The stress distribution resulting from the numerical analyses provided valuable information about the influence of the mass reduction in the crankshaft. Figure 4.8 shows the comparison between the maximum von Mises stress on the fillet radii of the original and lightweight crankshafts for bending moment of 700 Nm. The stress distributions indicate a relative increment of 1.3% in the maximum von Mises stress of the lightweight model.

The stress distributions of the static calibration analyses for the torsion case are depicted in Figure 4.9. The stress distribution of the two models presented no significant difference in the maximum von Mises stress of the oil hole. These numerical results showed that the mass reduction of the crankpin and crankwebs had low influence in the structural strength, emphasizing the arguments presented in Section 2.1.

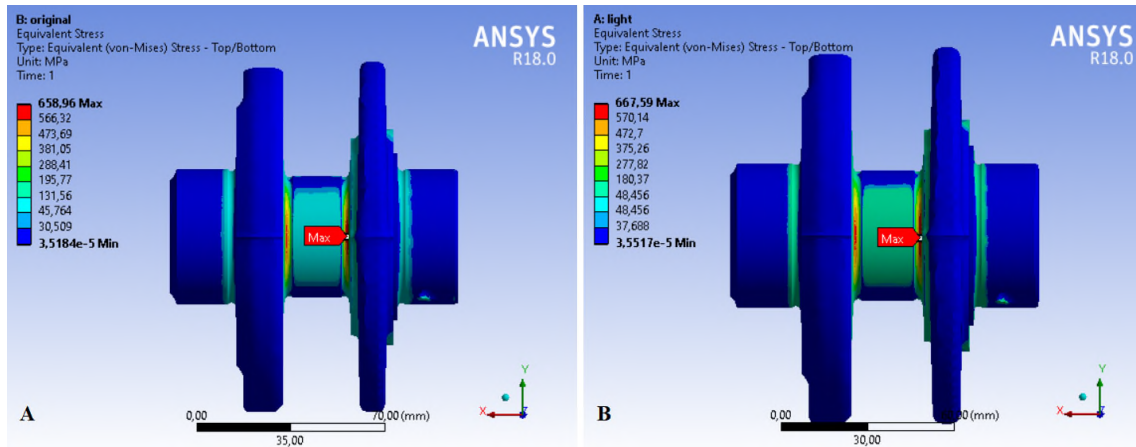


Figure 4.8 – von Mises stress distribution of the (A) original and (B) lightweight crankshafts subjected to 700 Nm bending moment.

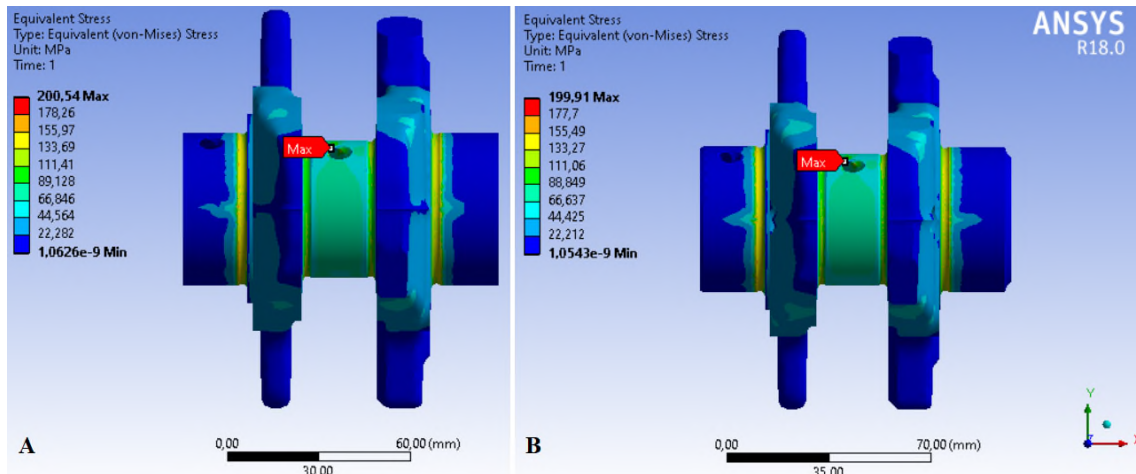
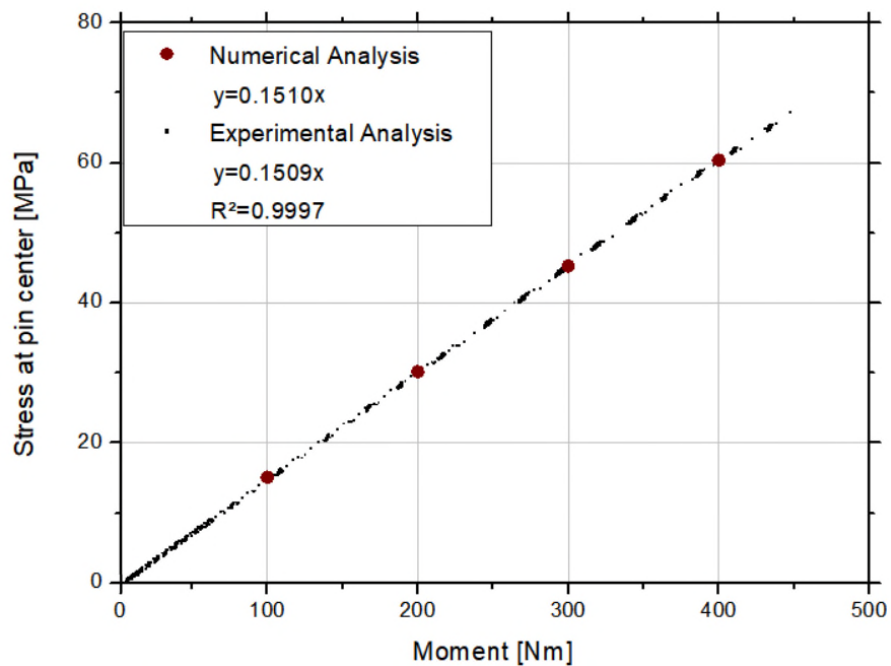
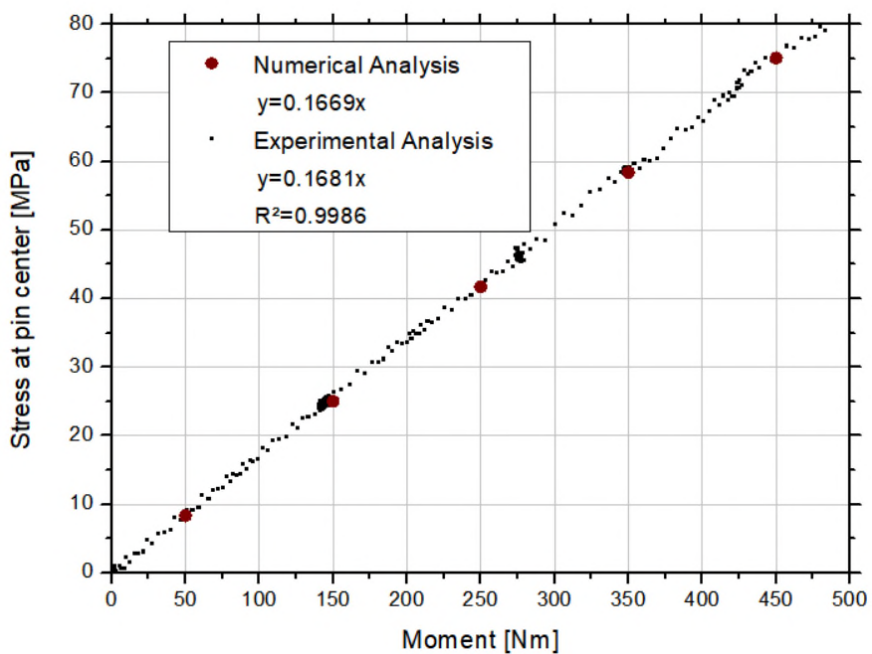


Figure 4.9 – Von Mises stress distribution of the (A) original and (B) lightweight crankshafts subjected to 700 Nm torsion moment.

The experimental data collected in the static tests were plotted and regression lines were generated for each tested case. Figure 4.10 shows the bending static calibration data of the original and lightweight crankshafts. The numerical and experimental data obtained in the torsion case is shown in Figure 4.11. As expected, the regression lines presented good values of determination coefficient (R^2) in all analyses, which means that the relation between strain and stress is well represented by the linear regression. Furthermore, the regression lines of the numerical data were very similar to the experimental ones in both bending and torsion cases. These results indicate that experimental static calibrations curves can be well represented by numerical analyses.

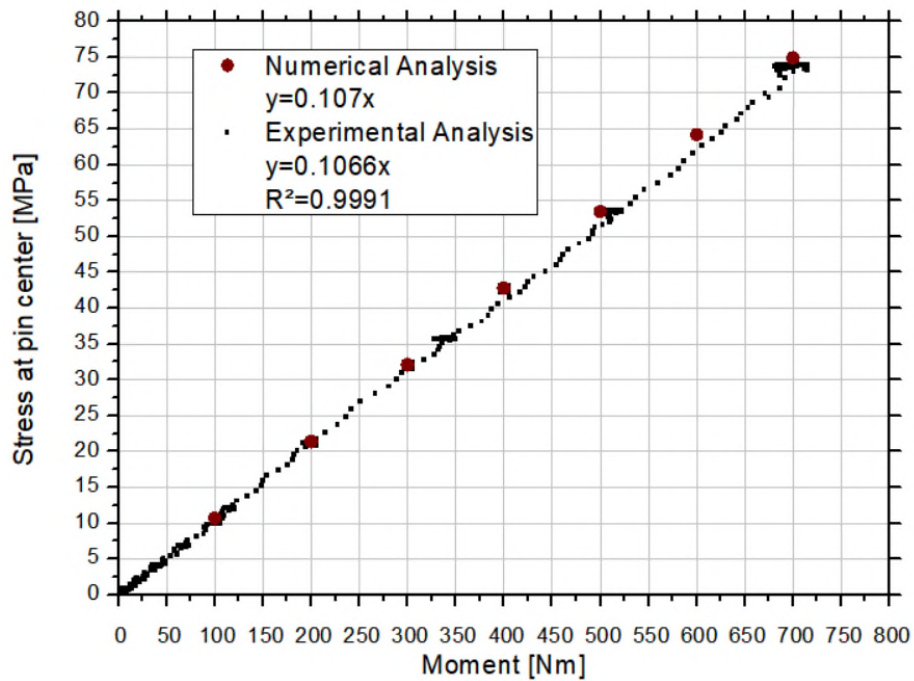


(a) Original crankshaft.

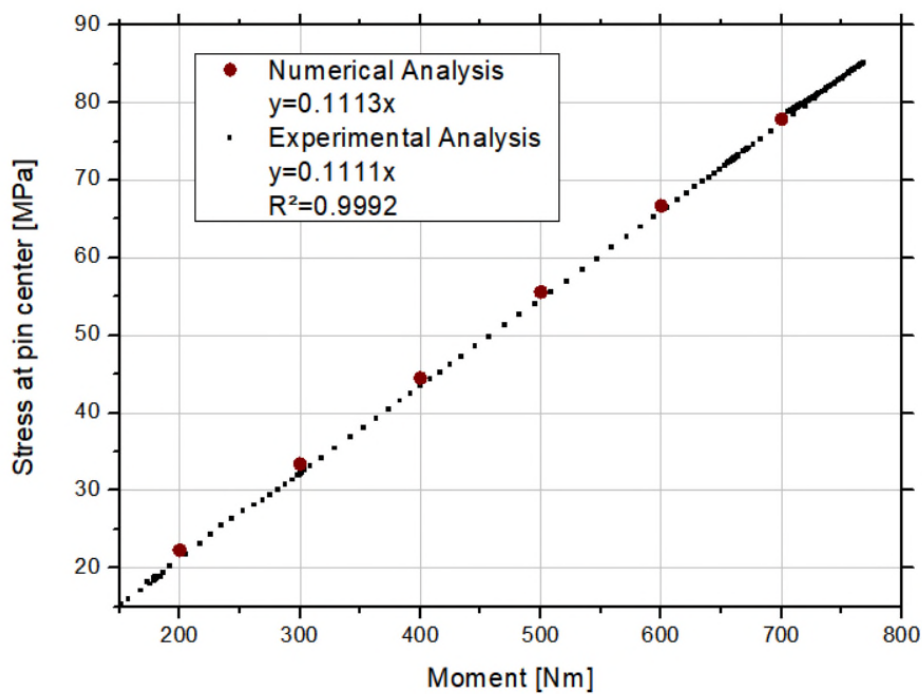


(b) Lightweight crankshaft.

Figure 4.10 – Experimental and numerical results of the bending static calibration for the (a) original and (b) lightweight crankshaft models.



(a) Original crankshaft.



(b) Lightweight crankshaft.

Figure 4.11 – Experimental and numerical results of the torsion static calibration for the (a) original and (b) lightweight crankshaft models.

4.2 Dynamic calibration

In fatigue tests of crankshafts, the dynamic calibration is carried out to determine the relation between the acceleration tracked by the accelerometer placed on the inertia plate and the strain measured by the strain gages. This relation makes possible to control the test load only by acceleration. Consequently, there is no need for instrumenting the specimens in the fatigue tests, except for the ones subjected to the calibration process. It is important to highlight that the harmonic response of the test rig highly depends on the stiffness of the crankshaft model. For this reason, the dynamic calibration must be carried out for each different model assessed. This section will describe the dynamic calibration and the equipment used in this procedure.

4.2.1 Dynamic calibration setup

Ideally, the dynamic test should be performed with a free body, without no constraints applied. However, due to the influence of the gravity, bodies subjected to dynamic tests must be suspended in such a way that the required mode of vibration is not restrained. In the bending analysis, the test rig is suspended by wires, according to Figure 4.12. This test setup requires accuracy in the system positioning due to the strong sensitivity of the shaker to misalignments. If the inertia plate is poorly positioned, the system can amplify rotation motion and generate bending moment in the shaker. In a critical case, the misalignment of the inertia plate can lead the shaker shaft to reach plastic strain. For this reason, a spirit level was used to make sure that the inertia plates would be well aligned. Figure 4.13 shows the bending test rig in the alignment process.



Figure 4.12 – Bending test rig suspended by wires through the lifting eyes.



Figure 4.13 – Spirit level used in the bending test rig alignment.

The electrodynamic shaker is adjusted on the inertia plate by means of a stinger threaded in a bore. The stinger must be flexible to not overload the shaker and enable the vibration of the system, but rigid enough to not fail in fatigue or reach plastic strain. Three mechanical jacks with adjustable height were used to provide the alignment of the shaker to the threaded bore. The accelerometer was arbitrarily placed in the backside of the second inertia plate, at the distance of 100 mm from the bottom. Figure 4.14 shows the bending test rig setup after the alignment procedures.

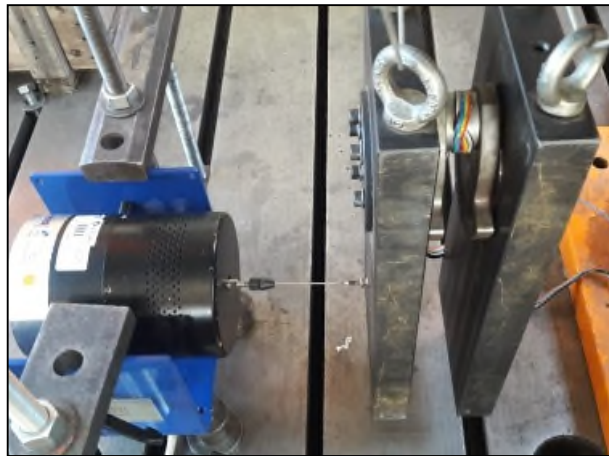


Figure 4.14 – Bending test rig setup.

In the torsion dynamic calibration, the rotation motion of the inertia plates must be unconstrained. For this reason, the test rig is suspended by bearings and shafts. Similarly, to the bending case, the shaker was fixed in the inertia plate by means of a stinger threaded in a bore. The shaker was positioned in a flat surface and fixed by threaded brackets to avoid translational displacement. The accuracy in the alignment is critical for a good performance of

the shaker because this system requires higher power to be driven. Two accelerometers were placed in the back of the inertia plates. The accelerometers were positioned in such a way that the signal tracked by them would be shifted by 180 degrees, characterizing the torsion mode of vibration. Figure 4.15 shows the positioning of the accelerometers and shaker in the inertia plates. The torsion test rig setup is depicted in Figure 4.16.

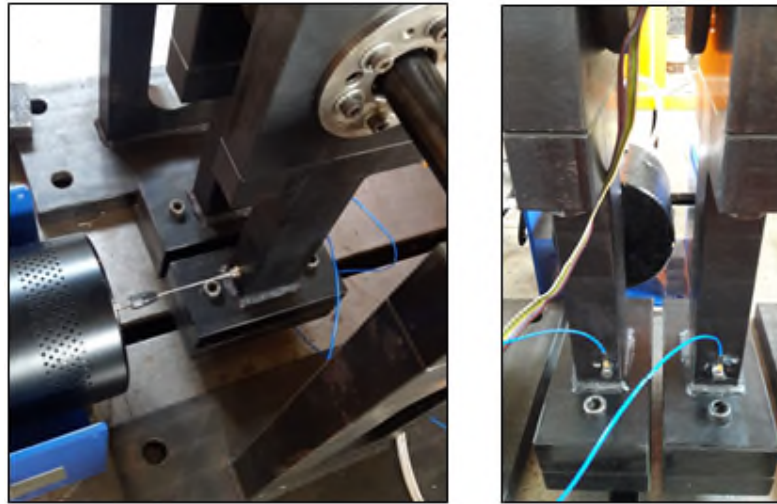


Figure 4.15 – Shaker fixation and accelerometer positioning in the inertia plates of the torsional test rig.

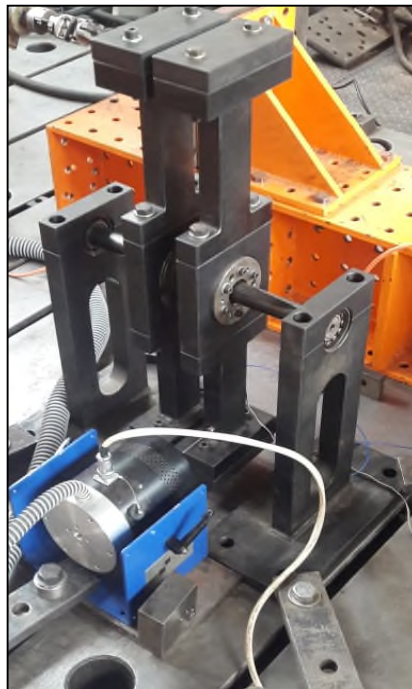


Figure 4.16 – Torsional test rig setup.

Despite the structural differences in the inertia plates, the dynamic calibration procedure is equivalent for both bending and torsion test rigs. At first, the frequency, shape and amplitude of the input signal was adjusted in a Goldstar FG8002 signal generator. The input signal was received by the QSC ISA 750 power amplifier, which was connected to the shaker. A blower was used in the Modal Shop 2100E11 electrodynamic shaker to prevent overheating. The acceleration of the inertia plate was measured by the ICP piezoelectric accelerometer. The accelerometer signal was conditioned in the PCB Piezotronics 480B21 ICP sensor signal conditioner.

The strain gage and acceleration measurements were acquired by the HBM MGCplus data acquisition system and correlated in the HBM Catman Easy software. The signal conditioner was linked to the Tektronix TBS1062 digital oscilloscope, wherein the acceleration response was displayed. The bending dynamic calibration scheme is depicted in Figure 4.17, which is similar for torsion dynamic calibration.

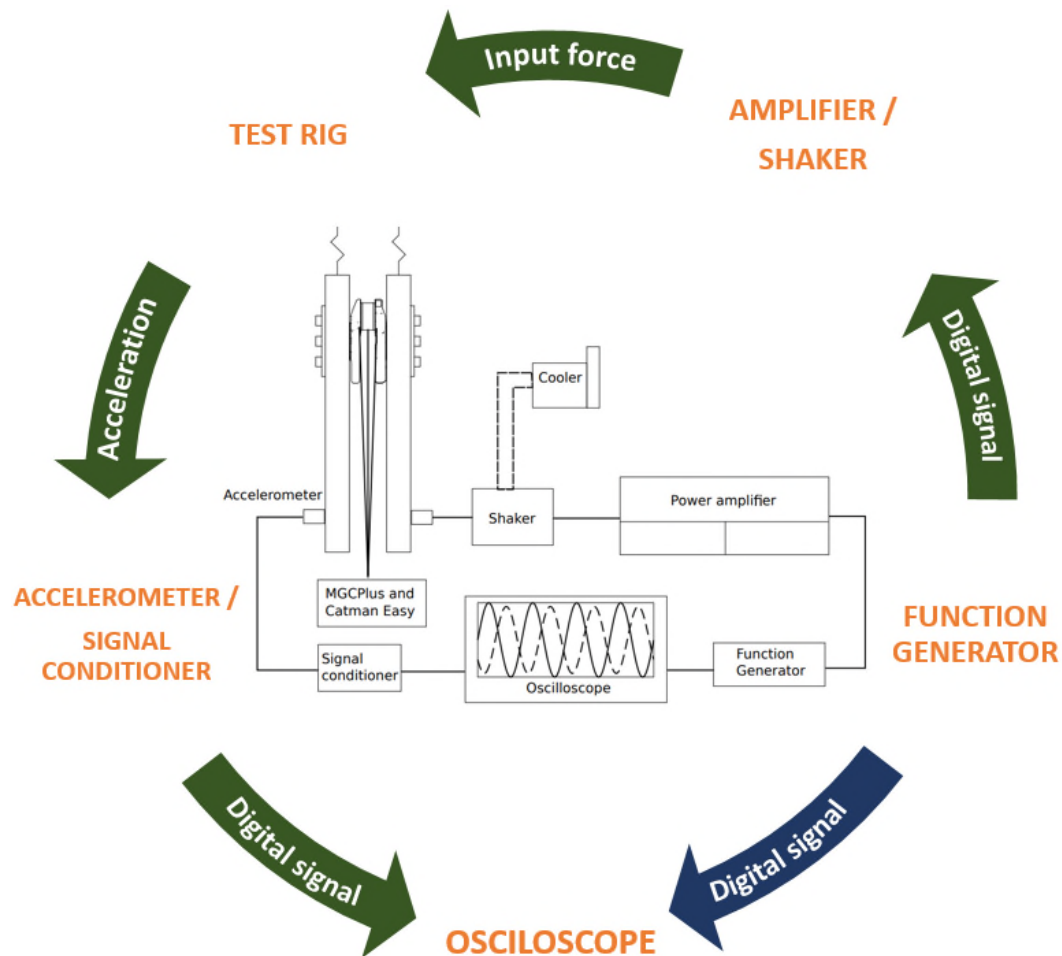


Figure 4.17 – Dynamic calibration setup scheme. Modified from (MORAES, 2017).

4.2.2 Dynamic calibration procedure

Once the testing setup is installed, the testing procedure can be initiated. At first, a frequency sweep was carried out in the sign generator to find the resonance frequency of the test rig. The numerical modal analysis results were used as reference for this step. Right after the determination of the resonance frequency, the input load was diminished until the system stop vibrating. Afterwards, the strain gage and accelerometer readings were set to zero to reduce the noise influence on the measures. At this step, the input force was steadily increased until an arbitrary maximum load in the resonance frequency. The measures from the strain gages and accelerometers were recorded in the HBM Catman Easy software, wherefrom the data for the calibration charts were obtained.

The data analyses showed some instability in the measures, indicating that the dynamic calibrations were performed in a transient state. Figure 4.18 depicts the values of stress in a sampling of the lightweight crankshaft recorded in the bending calibration for acceleration of 5g.

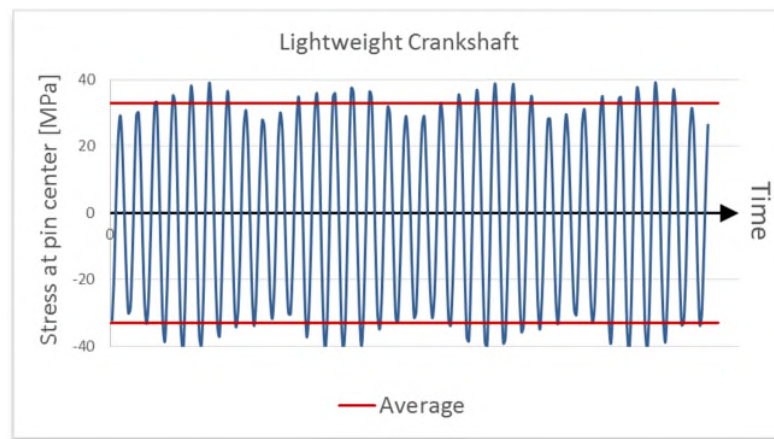
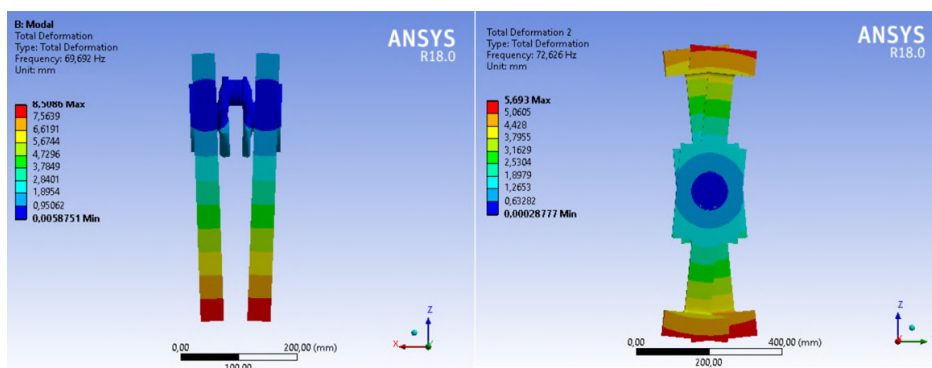


Figure 4.18 – Stress data sampling of the lightweight crankshaft dynamic calibration recorded for 5g in the bending mode.

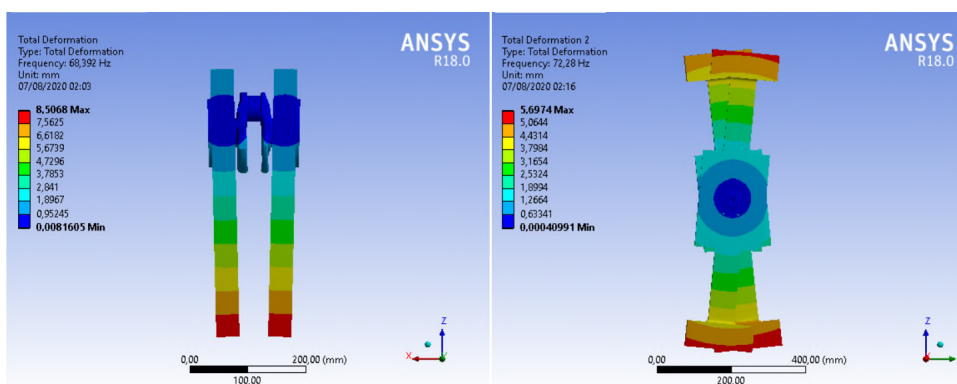
The instability in the dynamic calibration data is consequence of the transient state, which means that the measures were recorded while the test rig was working in an unstable state. This result shows that the increment rate of the input load has influence on the standard deviation of the measurements. In this work, the dynamic calibration charts were built in terms of the maximum amplitudes averaged and the respective standards deviations, according to Figure 4.18.

4.2.3 Numerical dynamic calibration

The modal and harmonic response analyses of the test rigs can also be performed numerically, as discussed in Section 3.2. The numerical harmonic response analysis can provide information about the acceleration and stress for any region of the test rig and crankshaft. Despite the damping properties are unknown, the dynamic calibration curve is not affected by the damping factor. For this reason, the procedures described in Section 3.2 were repeated for the bending case and for both crankshaft models. Figure 4.19 shows the bending and torsion modes of vibration and the respective resonant frequencies obtained by numerical simulations.



(a) Original crankshaft.



(b) Lightweight crankshaft.

Figure 4.19 – Bending and torsion resonance frequencies of the original and lightweight models.

The resonant frequencies from harmonic response analyses of both bending and torsion cases are summarized in Table 4.3 and Table 4.4, respectively. Because the resonance

frequency depends on the stiffness of specimen, experimental data were presented in an interval defined between the minimum and maximum resonance frequencies observed for each crankshaft model. We can notice that the numerical results were very close to the experimental resonance frequencies. The torsion numerical models presented larger relative deviation, which can be explained by the complexity of the test rig.

Table 4.3 – Numerical and experimental resonance frequency of the bending vibration mode for different crankshaft models.

Bending resonance frequencies		
Crankshaft	Experimental	Numerical
Original	68.4 - 69.3	69.69
Lightweight	67.3 - 67.7	68.39

Table 4.4 – Numerical and experimental resonance frequency of the torsion vibration mode for different crankshaft models.

Torsion resonance frequencies		
Crankshaft	Experimental	Numerical
Original	70.5 - 71.2	72.63
Lightweight	70.3 - 70.7	72.28

The acceleration response of the lightweight crankshaft in the bending test rig is shown in Figure 4.20. Figure 4.21 shows acceleration response of the original crankshaft in the torsion test rig. As expected, in the torsion mode of vibration, the signals of the two accelerometers placed in the inertia plates were shifted by 180 degrees, which means that the inertia plate arms were vibrating in opposite sense.

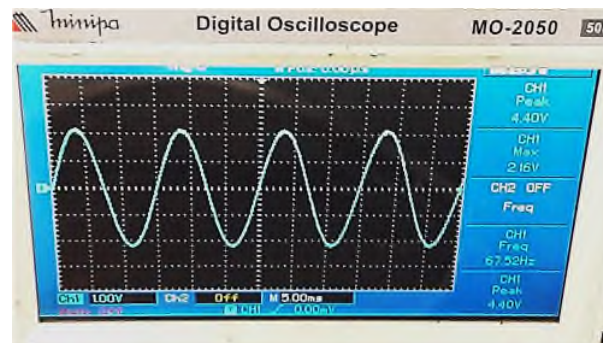


Figure 4.20 – Oscilloscope screen showing the acceleration response of the bending dynamic calibration of the lightweight model.

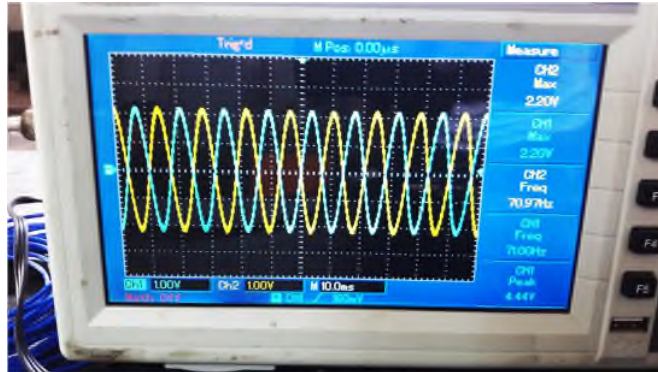


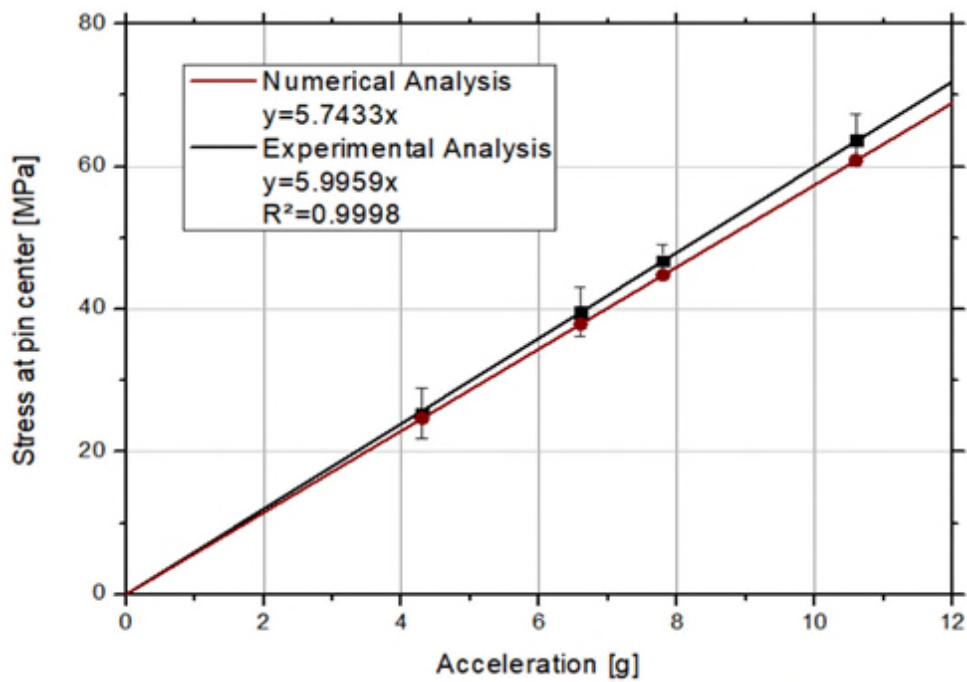
Figure 4.21 – Oscilloscope screen showing the acceleration response of the torsion dynamic calibration of the original crankshaft model.

4.2.4 Dynamic calibration charts

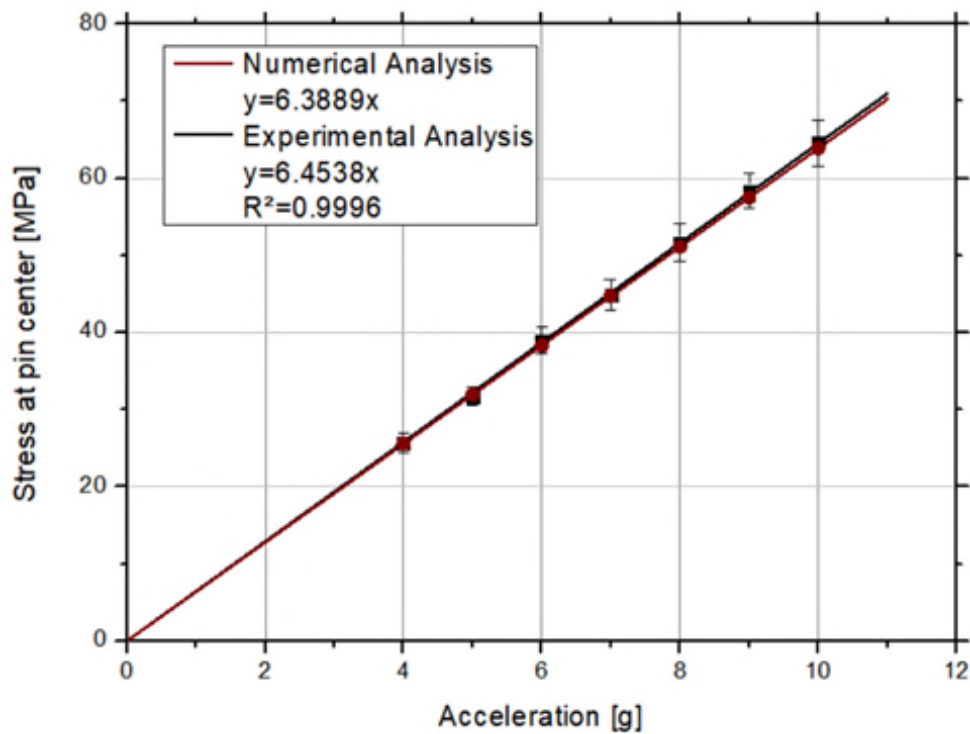
The numerical and experimental data obtained in the dynamic calibration tests were plotted in calibration charts. Similarly to the static case, the stresses were calculated by Equations (4.1), (4.2), (4.3) and (4.4). Figure 4.22 and Figure 4.23 show the dynamic calibration charts of the original and lightweight crankshaft models for the bending and torsional modes of vibration, respectively. As expected, the relation between stress and acceleration was linear.

The larger standard deviation observed in Figure 4.22 is related to the transient zone, which means that the data were recorded while the test rig was vibrating unsteadily, as explained in Section 4.2.2. Figure 4.23 shows a better standard deviation in the torsion calibration, even though the difference between numerical and experimental results were higher for this case. This difference between numerical and experimental curves, however, can be explained by the larger complexity of the torsion test rig. It is important to highlight that the stress distribution of the harmonic response analysis depends on the modal analysis and the error is cumulative.

Another important issue that must be taken into account in the analysis of the standard deviation is the influence of noise in the measurements. The static analysis measurements is less affected by the noise of the environment and equipment because the sampling frequency is low (about 50 Hz). In the case of the dynamic calibration, the sampling frequency is 600 Hz and, therefore, has more sensitivity to detect noise in the measurements. The higher discrepancy between numerical and experimental measurements in the dynamic calibration can be explained by the influence of noise in the system and the vibration transient state during the experimental calibrations.

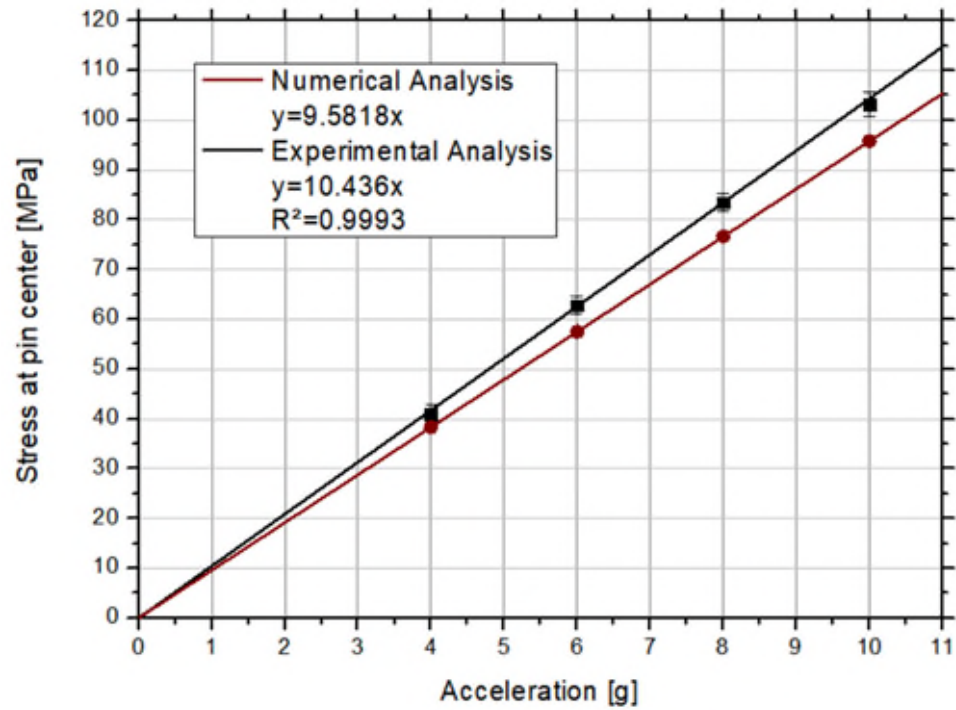


(a) Original crankshaft.

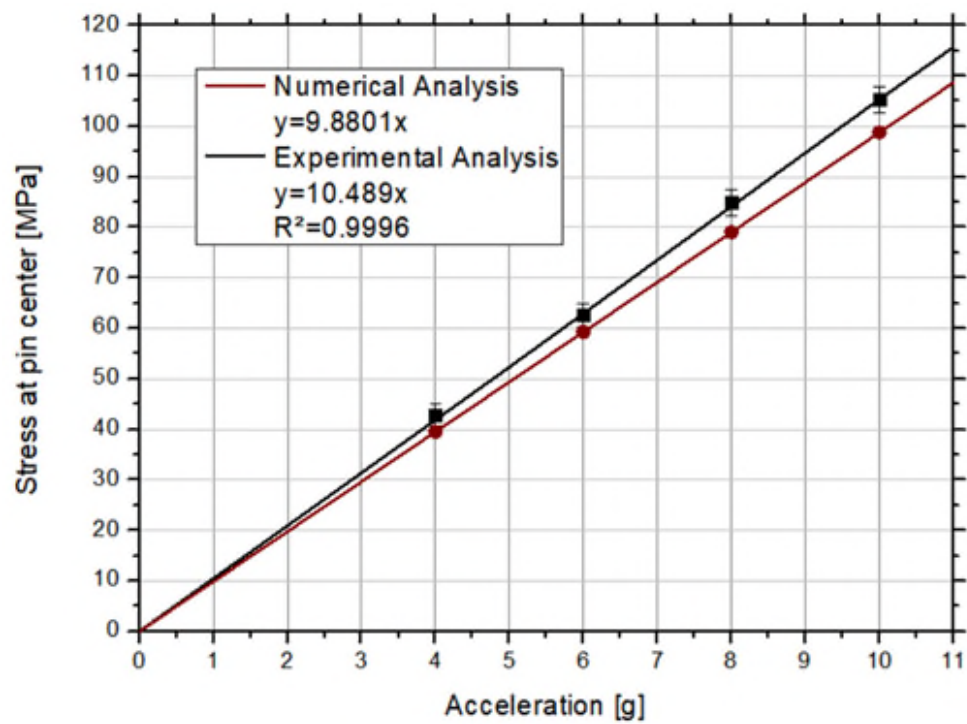


(b) Lightweight crankshaft.

Figure 4.22 – Bending dynamic calibration curves of the original and lightweight crankshaft models.



(a) Original crankshaft.



(b) Lightweight crankshaft.

Figure 4.23 – Torsion dynamic calibration curves of the original and lightweight crankshaft models.

5. CRANKSHAFT FATIGUE TEST

The previous chapters discussed the main aspects and concepts before running the fatigue tests in crankshafts. The methodology used for designing the crankshaft prototypes and the torsion test rig were presented in Chapters 2 and 3. Chapter 4 focused on the calibration procedures and numerical analyses. This chapter presents the methodology used in the crankshaft fatigue assessment, as well as the criteria adopted to determine the mean fatigue limit of the different models evaluated in this work.

5.1 Fatigue test procedure

The nucleation and propagation of cracks in the crankshaft decrease the stiffness of the specimen and shift the resonance frequency of the test rig. The resonant fatigue tests of crankshafts are based on this phenomenon, which is well explained by Gudmundson (1982). Feng and Li (2003) showed that the resonance frequency of the fatigue test rig can be automatically tracked by a controller. In this work, however, the resonance frequency was manually adjusted by means of a signal generator and the accelerometer signal displayed in an oscilloscope. The test set up and the alignment procedures described in Section 4.2.1 were also applied to the fatigue test.

The fatigue test procedure is very similar to the dynamic calibration. The difference is that, in the fatigue case, the specimens are not instrumented with strain gages and the data acquisition system is not required. Firstly, the test rig is excited with a dwell sine signal in low amplitude. Then, the frequency of test is swept in a range close to the resonance frequency, determined in the dynamic calibration. The maximum acceleration response indicates whether the system is in resonance. As the frequency adjustment is not automatic, the operator must follow the test progress until the detection of any drop in the acceleration response.

The decrease in the acceleration amplitude indicates the resonance frequency is shifting due to crack nucleation; therefore, the operator must repeat the frequency sweep process to find the new resonance frequency. If the decrease is of 3% of the original test frequency, then the test is stopped and the specimen is defined as failure. If no frequency drop is detected, then the fatigue test stops after 2 million cycles and the specimen is considered approved. The fatigue test procedure is summarized in Figure 5.1.

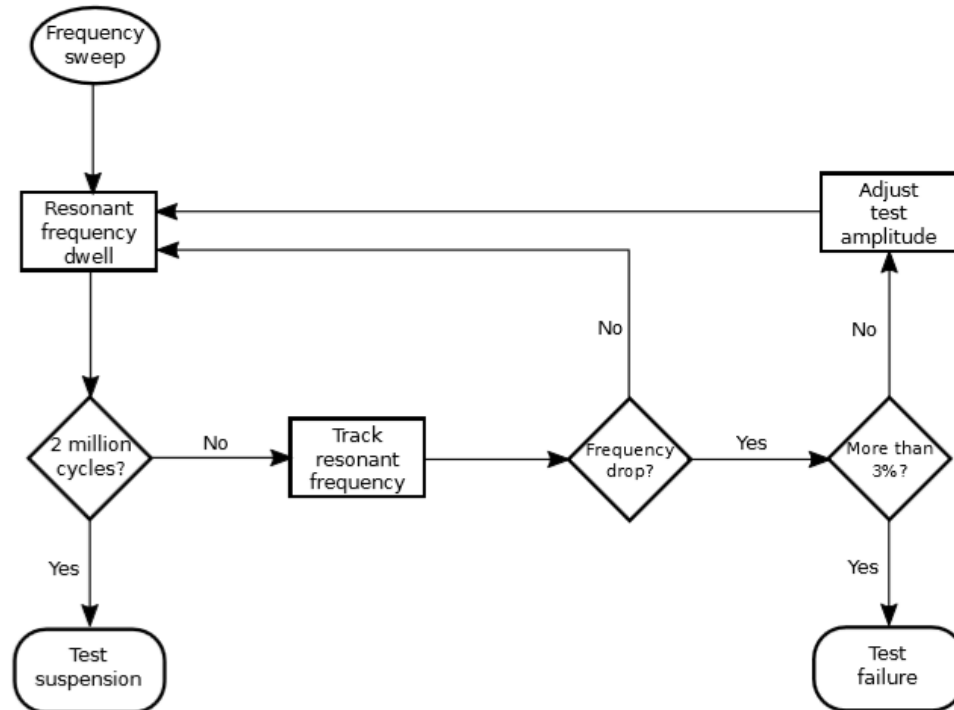


Figure 5.1 – Flow diagram for fatigue test in crankshafts. Available from (MORAES, 2017).

5.2 Staircase method

In an ideal environment, the fatigue limit of a specified crankshaft model would be equivalent for any tested specimen. However, even if the manufacturing process is well controlled, the specimens have different mechanical properties due to the inclusion of impurities in the material or other variants in the production system. Due to the specimen variability, the fatigue limit of crankshafts has a stochastic nature. For this reason, the mean fatigue strength is determined by means of statistical analysis and data reduction models.

Regarding statistical analysis, the fatigue tests can be performed by different methods, depending on the main interest of the analysis, number of specimens or available resources. In the past, the Probit method was very used for estimating the fatigue limit of materials. However, this method requires over 30 specimens to estimate the fatigue limit accurately. The Probit method is more suitably used for determining the fatigue strength response curve and the proportion of specimens which fails before a specified number of cycles. (ASTMSTP91A,1963; BS3518-5,1966; POLLAK, R.D.,2006). The staircase method (also known as Up-and-Down method) is considered statistically more efficient for determining the mean fatigue limit of components.

Dixon and Mood (1948) indicated that the staircase method would require about forty to fifty specimens to reach accuracy in the estimative of the main fatigue strength. The ASTM fatigue standard test (ASTM STP91A, 1963) and the British standard (BS 3518-5, 1966) advise the use of at least 30 specimens in the traditional staircase method. However, Brownlee et al (1953) pointed out that, besides being more efficient than the usual Probit analysis method, the staircase method can obtain reasonably reliable estimate for mean fatigue strength with five to ten specimens. The Japan Society of Mechanical Engineers (JSME) also indicates a 6-specimen staircase for determining the fatigue limit of components (NAKAZAWA et al. 1987, apud POLLAK, 2006).

The greatest disadvantage of the staircase method is that the trials must be made sequentially, which requires much time wasting for fatigue tests (BROWNLEE et al, 1953). This occurs because the load magnitude depends on previous results. Initial load is usually determined based on the main fatigue strength of the material or experimental results obtained previously for similar components (POLLAK, 2006; LEE, 2005). Lee (2005) also recommends that the test load of the first specimen is slightly higher than the estimated fatigue strength. The test load of the second specimen is determined based on the previous result. If the first specimen fails, the second one is tested with a load decreased by an adopted step. If the first specimen does not fail after the specified number of cycles, then the second one is tested with one step higher load.

The step size of the increment or decrement of the test load has impact in the final results. The standard deviation equations assume that the step size is between 0.5σ and 2σ , where σ is the true standard deviation of the fatigue test (POLLAK, 2006). The British Standard recommends a step size equivalent to the standard deviation (BS 3518-5, 1966). The ASTM standard (ASTM STP91A, 1963), otherwise, suggests that the step size must be from $2/3$ to $3/2$ of the true standard deviation. For these reasons, the standard deviation must be estimated prior to the test. This estimative can be done based on previous tests of similar components. If there are no data available about similar components, the standard deviation can be estimated in terms of the fatigue strength of the material. Snyder et al. (2004, apud MORAES, 2017) observed that the step size can vary from 2 to 8% of the fatigue strength, while Lee (2005) recommends a step size of 5% of the fatigue strength.

5.3 Dixon-Mood data reduction model

A great advantage of the staircase method is that the equations used to estimate the

fatigue strength are simple and easy to compute, whereas other methods require complex iterative calculation or graphical methods to estimate parameters (POLLAK, 2006). The approach used for interpreting the staircase data was developed by Dixon and Mood (1948), who used probability estimation techniques to determine analytically the mean and the standard deviation from the staircase data of explosive tests. The Dixon-Mood approach assumes that the variation is normally distributed and the step size is less than twice the standard deviation (DIXON; MOOD, 1948).

In this work, the mean fatigue strength and the standard deviation were estimated according to the staircase method and the Dixon-Mood (1948) approach. The mean fatigue limit was computed in terms of applied moment load instead of stress because this quantity has direct comparison between the crankshaft models. The equations used in the Dixon-Mood method were based on Lee (2001) and Moraes (2017). The mean fatigue limit μ was calculated by the following equation:

$$\mu = M_0 + d \left(\frac{A}{\sum n_i} \mp \frac{1}{2} \right), \quad (5.1)$$

wherein d is the constant step adopted in the staircase method, M_0 is the lowest moment applied to the specimens and n_i is the number of less frequent event at load level i . If the less frequent event is “failure”, then the signal “-” must be used in Equation (5.1). Otherwise, if “suspension” is the less frequent event, then the signal “+” must be used in Equation (5.1). The quantity A is given by

$$A = \sum i n_i. \quad (5.2)$$

The standard deviation σ_s can be calculated by

$$\sigma_s = 1.62d \left[\frac{B \sum n_i - A^2}{(\sum n_i)^2} + 0.029 \right], \quad \text{if } \frac{B \sum n_i - A^2}{(\sum n_i)^2} > 0.3 \quad (5.3)$$

or

$$\sigma_s = 0.53d, \quad \text{if } \frac{B \sum n_i - A^2}{(\sum n_i)^2} \leq 0.3 \quad (5.4)$$

where B is defined by

$$B = \sum i^2 n_i. \quad (5.5)$$

The number of specimens and the step size adopted in this work are summarized in Table 5.1. Even though 6 and 8 specimens can be considered low for approval or disapproval of crankshaft models in an automotive company, which usually tests more than 10 specimens, this quantity of specimens is acceptable for an academic evaluation.

Table 5.1 – Number of specimens and step size applied to the fatigue tests of the original crankshaft.

Fatigue test	Number of specimens n	Step size d [Nm]
Bending	8	36
Torsion	6	40

5.3.1 Staircase Results

The specimens were tested until 2 million cycles and the 3% resonance frequency drop criterion was applied according to the flow diagram illustrated in Figure 5.1. The staircase chart of the original model tested under bending loading is represented in Figure 5.2. For this case, both “+” or “-” signal can be used in the computation of the mean fatigue strength because both events (failure and suspension) occurred in the same amount. In this work, “failure” was arbitrarily chosen as less frequent event. Table 5.2 summarizes the number of failures and bending moments applied for each load magnitude.

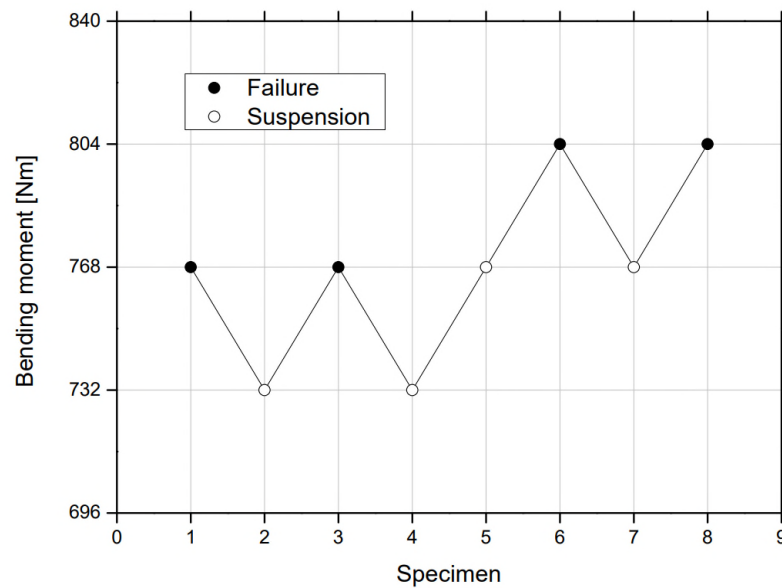


Figure 5.2 – Representation of the staircase data for the original crankshaft model tested in the bending.

Table 5.2 – Bending load magnitude and number of occurrence of less frequent event for the original crankshaft model.

Bending moment M_i [Nm]	Load level number i	Number of occurrence n_i
732	0	0
768	1	2
804	2	2

Figure 5.3 shows the staircase chart for the original crankshaft model tested under torsion loading. Similarly to the bending test, both failure and suspension events can be used to calculate the mean fatigue strength because both events occurred 3 times. Table 5.3 contains the values of torsion moment and number of failures for each load magnitude.

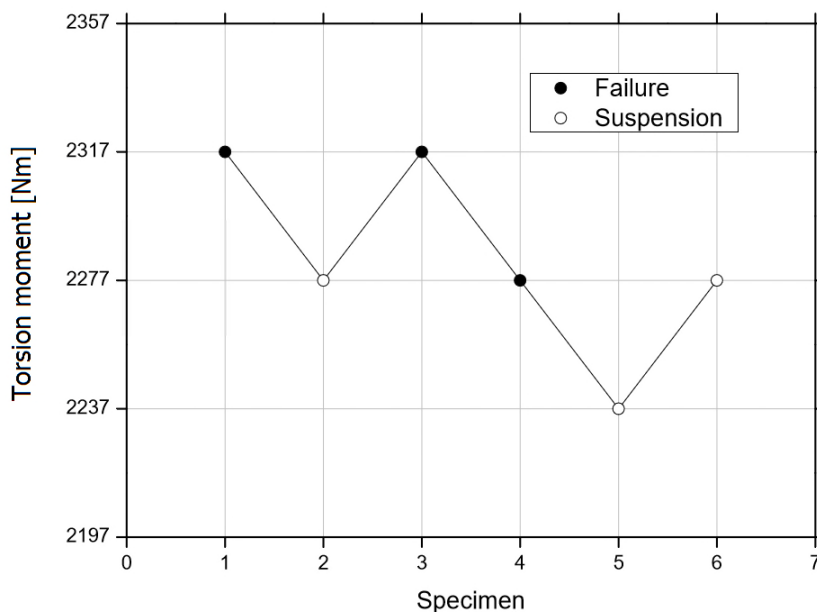


Figure 5.3 – Visual representation of the staircase data of the original crankshaft model tested in the torsion.

Table 5.3 – Torsion load magnitude and number of occurrence of less frequent event for the original crankshaft model.

torsion moment M_i [Nm]	Load level number i	Number of occurrences n_i
2237	0	0
2277	1	1
2317	2	2

The staircase data of the original crankshaft model and the number of cycles for each specimen of the bending and torsion tests are summarized in Table 5.4 and Table 5.5, respectively. Since the fatigue strength of the crankshaft must be estimated before the fatigue tests, the first specimen of the torsion case was tested at different loads until reaching fatigue, according to Table 5.6. The first torsion moment applied to the specimens in the staircase method was defined based on this first test.

Table 5.4 – Staircase fatigue data of the original crankshaft for bending moment.

Specimen	Bending Moment [Nm]	Number of cycles	Outcome
1	768	1,289,508	Failure
2	732	2 million	Suspension
3	768	522,749	Failure
4	732	2 million	Suspension
5	768	2 million	Suspension
6	804	1,098,214	Failure
7	768	2 million	Suspension
8	804	334,102	Failure

Table 5.5 – Staircase fatigue data of the original crankshaft for torsion moment.

Specimen	Torsion Moment [Nm]	Number of cycles	Outcome
1	2317	942,442	Failure
2	2277	2 million	Suspension
3	2317	1,575,348	Failure
4	2277	1,244,156	Failure
5	2237	2 million	Suspension
6	2277	2 million	Suspension

Table 5.6 – Load magnitude and number of cycles for the first torsion test of the original crankshaft model.

Torsion Moment [Nm]	Outcome	Number of cycles
1899	Suspension	2 million
2036	Suspension	2 million
2277	Suspension	2 million
2317	Failure	539,210

Equations (5.1) and (5.2) and Tables 5.2 and 5.3 were used to obtain the mean fatigue limit for 2 million cycles of the original crankshaft model. These results are

summarized in Table 5.7. The fatigue strength for torsion moment (2283.67 Nm) is almost three times the bending moment (768.00 Nm). This result indicates that the crankshaft is more sensitive to bending than torsion loads, which can be explained by the high stress concentration on the fillets. The standard deviation for both bending and torsion cases are almost twice the step size adopted in the staircase method.

Table 5.7 – Mean fatigue limit calculation for the original crankshaft model.

Fatigue test	A	B	M_0 [Nm]	d [Nm]	$\sum n_i$	μ [Nm]	σ_s [Nm]
Bending	6	10	732	36	4	768.00	19.1
Torsion	5	9	2237	40	3	2283.67	21.2

In this work, two specimens of the lightweight model were tested for each loading case (bending and torsion). The number of specimens available for fatigue tests were not enough for applying the staircase method. However, the objective of these fatigue tests was not to estimate the mean fatigue strength of the lightweight model, but detecting any influence of the modifications in the original geometry in the fatigue strength of the original model. For these reasons, the lightweight specimens were tested at different loads until reaching failure before 2 million cycles. Since the load applied to the specimens depends on the stiffness of the crankshaft, it was not possible to apply the same load in both original and lightweight models. Nevertheless, the moment applied to the lightweight model were close to those ones of the original model. Table 5.8 and Table 5.9 show the load magnitude and the number of cycles for the bending and torsion specimens, respectively.

Table 5.8 – Bending moment magnitudes and number of cycles of the lightweight crankshaft specimens.

Bending moment [Nm]	Number of cycles Specimen 1	Number of cycles Specimen 2	Outcome Specimen 1 and 2
721	2 million	-	Suspension
737	2 million	-	Suspension
769	2 million	2 million	Suspension
798	2 million	2 million	Suspension
813	541,404	596,250	Failure

Table 5.9 – Torsion moment magnitudes and number of cycles of the lightweight crankshaft specimens.

Torsion moment [Nm]	Number of cycles Specimen 1	Outcome Specimen 1	Number of cycles Specimen 2	Outcome Specimen 2
2153	2 million	Suspension	2 million	Suspension
2190	2 million	Suspension	1,116,896	Failure
2228	2 million	Suspension	-	-
2266	822,510	Failure	-	-

In the bending test, the lightweight specimens showed fatigue strength two steps superior to the mean fatigue strength of the original model. The increase of fatigue strength in the modified crankshafts can be explained by the stochastic nature of the fatigue tests and the difference of production lot. Even though the specimens were manufactured by the same company, the events and variants of the production system can affect the mechanical properties of the crankshafts.

In the torsion test, the first specimens failed at the same load of the mean fatigue strength of the original model, while the second specimen failed two steps lower. These results indicate that the mass subtraction in the inner pin region was slightly prejudicial to torsion fatigue strength.

The fatigue strength obtained for the original and lightweight crankshafts were calculated considering the experimental calibration curves. However, the fatigue strength can also be obtained from the numerical calibrations. Table 5.10 and Table 5.11 present the main fatigue limit obtained from the experimental and numerical calibrations for the original and lightweight specimens. The lightweight fatigue strength in these tables represents the arithmetic average of the two specimens tested for each case and the relative error is defined as the difference between the experimental and numerical values divided by the experimental one.

Table 5.10 – Bending mean fatigue strength calculated from numerical and experimental calibrations of the original and lightweight crankshaft models.

Crankshaft model	Experimental [Nm]	Numerical [Nm]	Relative Error
Original	768.00	750.22	2.32%
Lightweight	798.00	790.53	1.01%

Table 5.11 – Torsion mean fatigue strength calculated from numerical and experimental calibrations of the original and lightweight crankshaft models.

Crankshaft model	Experimental [Nm]	Numerical [Nm]	Relative Error
Original	2278.67	2088.67	8.34%
Lightweight	2190.50	2059.46	5.98%

The relative errors between the numerical and experimental results indicate that the experimental calibrations were well represented by the numerical simulations. It is important to highlight that the relative error presented contains the individual deviation of the static and the dynamic calibration, since these two analyses were used for determining mean fatigue strength. Therefore, the relative errors calculated for the torsion specimens are consequence of the higher deviation obtained in the torsion dynamic calibration. These results increase the reliability of the stress distribution from the numerical models, which provides substantial information about the critical regions that were not experimentally measured in this work.

5.4 Crack analysis

The failure criterion adopted in this work determines that the fatigue test will be stopped if the resonance frequency drops more than 3% before 2 million cycles. After the test, the failed specimens were subjected to liquid penetrant inspection for revealing cracks in the critical regions. An example of a crankshaft specimen covered by the penetrant liquid is depicted in Figure 5.4. As expected, the bending specimens presented cracks in the fillet radii, whereas the torsion ones revealed cracks in the oil hole, according to Figure 5.5 and Figure 5.6, respectively.



Figure 5.4 – Penetrant liquid applied to the crankshaft specimen.

Figure 5.6 (a) shows that, under torsion loads, the crack nucleates at 45° from the crankpin centerline and propagates along the oil hole direction, passing through the critical region pointed by the numerical simulation (Figure 3.13 (b)). Figure 5.6 (b) shows that after 3% drop of the resonance frequency, the crack propagated from the surface to the inner center of the crankpin.



Figure 5.5 – Crack on the fillet radius surface of the original crankshaft model.

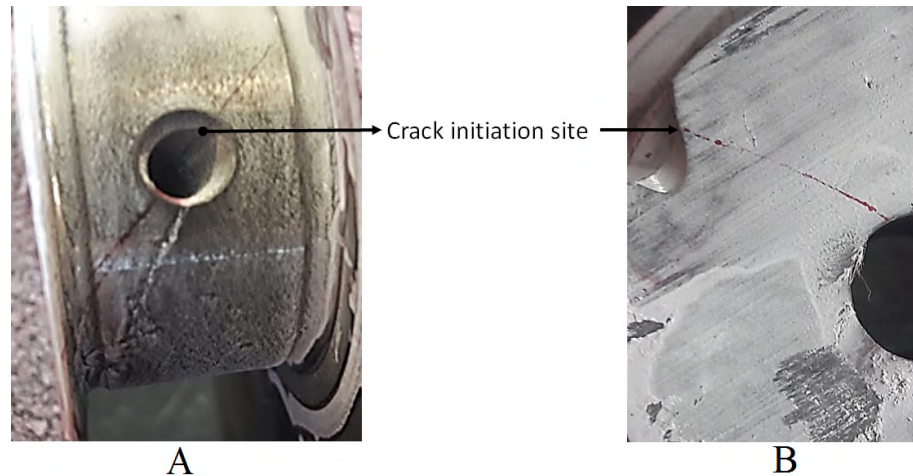


Figure 5.6 – Crack on the (A) surface and (B) inner region of the crankpin of the lightweight crankshaft model.

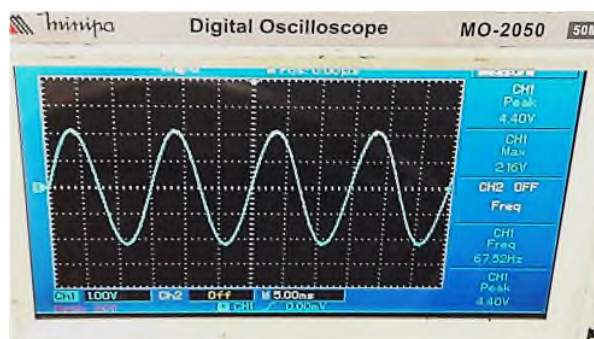
This work aimed to understand how the mass subtraction performed in the crankpin would affect the crack propagation in the crankshaft. In the original model, it is known that the crack initiates on the fillet radii and propagates throughout the crankweb. In the lightweight model, however, the mass reduction in the inner center of the crankpin could affect the trajectory of the crack propagation. For this reason, the bending specimens of the lightweight crankshaft model were tested until two-piece complete failure for verifying the crack trajectory.

It is important to highlight that the dynamic calibrations performed for each crankshaft model depends on the resonance frequency of the tested system. Therefore, the resonance frequency shift implies in different loads acting on the specimen and the linear relation between acceleration and stress changes according to the test frequency. The influence of this loading difference was disregarded for specimens of the same model.

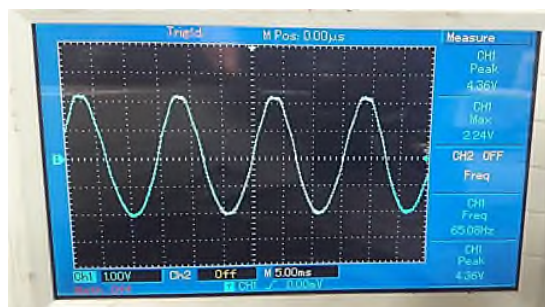
The bending or torsion moment acting on the specimen highly depends on the stiffness of the crankshaft, in such a way that it is not possible to know the moment applied to the specimen after the 3% drop of the initial test frequency. Furthermore, the instability of the fatigue test increases as the crack propagates in the specimen. For this reason, the fatigue test conducted after the 3% drop in the resonance frequency must be carried out with caution to prevent damage to the shaker.

Figure 5.7 shows the acceleration response and the resonance frequency shift of a lightweight specimen during the fatigue process. The acceleration response depicted in Figure

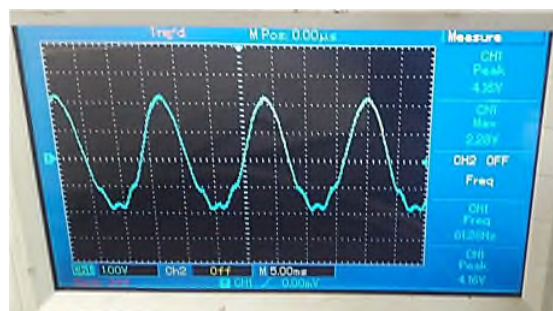
5.7 (b) shows slightly instability in the vibration mode from 65.08 Hz (3.6% drop of resonance frequency). The instability of the fatigue test increases as the crack propagates in the crankthrow and, as consequence, the maximum acceleration amplitude decreases proportionally.



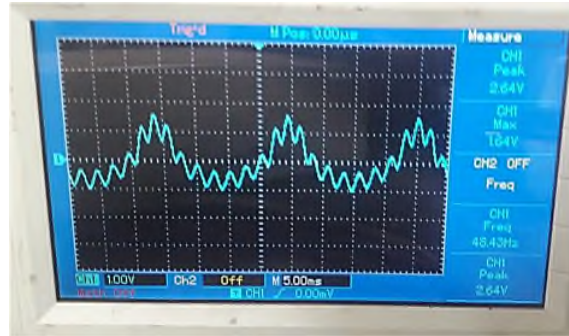
(a) 22.0 g and 67.52 Hz.



(b) 21.8 g and 65.08 Hz.



(c) 20.8 g and 61.26 Hz.



(d) 13.2 g and 48.43 Hz.



(e) 7.6 g and 39.44 Hz.

Figure 5.7 – Oscilloscope screen displaying the maximum acceleration response and the resonance frequency of the crankshaft specimen in fatigue process.

When the test frequency decreases about 42% (39.44 Hz), the specimen is in the imminence of reaching two-piece fracture. At this point of the fatigue test, the stiffness of the system is too low to reach resonance and the force applied to the front plate is poorly transferred to the second one, according to Figure 5.7 (e). These results show that the loads acting in the specimens are unknown after 3% drop of the resonance frequency. This feature is particularly important because the crack propagation region can be extended whether the moment applied to the specimen decreases during the test.

Figure 5.8 depicts the fractured specimen of the lightweight crankshaft model. There are three well defined regions that characterize the crack initiation (I), propagation (II) and the final rupture (III). The size of the crack propagation region indicates that the material absorbed much energy before fracture. However, the propagation region showed in Figure 5.8 may not represent the true behavior of the crankshaft because the instability of the fatigue test after 3% drop in the resonance frequency reduces the moment applied to the specimen. For this reason, region II would be smaller whether the initial bending moment were kept constant along the test. Even though little information was revealed about the ductility of the material, the crack fracture analysis shows that the modifications in the geometry had no influence in

the crack trajectory. Similarly to the original model, the crack initiated on the fillet radius and propagated throughout the crankweb, passing by the oil hole and reaching the external surface.



Figure 5.8 – Crack propagation regions in the crankweb of the lightweight crankshaft model.

In the case of the torsion specimen, it was not possible to reach two-piece failure. The system became excessively unstable and the resonance frequency stopped decreasing before the final rupture of the specimen. For this reason, the test had to be stopped to avoid damage to the shaker. Figure 5.9 shows the crack initiated at 45° in the crankpin surface of the torsion specimen of the lightweight model. The difficulty to reach the two-piece failure under torsion loads in the lightweight model can be justified by the inner hole of the crankpin, which prevent the crack to continue propagating through the crankshaft. This result indicates that the mass subtraction of the inner crankpin can be beneficial for preventing the two-piece fracture of crankshafts subjected to torsional vibration in internal combustion engines.

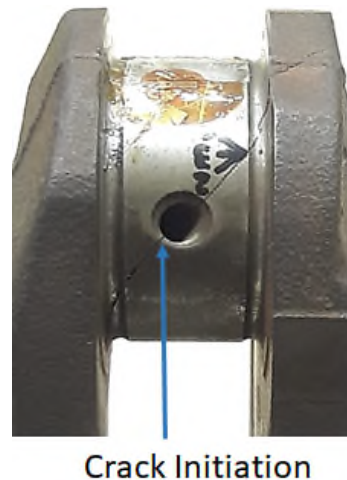


Figure 5.9 – Crack initiated in the surface of the torsion specimen of the lightweight crankshaft model.

5.5 Numerical fatigue analysis

The fatigue phenomenon has increased interest of researchers around the world since the 18th and 19th centuries, when the first cases of unexpected failures under dynamic loads suddenly appeared. This phenomenon, however, is so complex that still there are many questions about the mechanisms involved in the crack nucleation and propagation. The complexity of this phenomenon derives from many parameters that interfere in the fatigue behavior, such as geometry, stress concentration, defects in the microstructure (pores, inclusions, lattice distortion), temperature, corrosion, mean stress effect, manufacturing process, among other parameters.

In fracture mechanics, some models can be used to predict the fatigue failure, but they are usually used in 2D specimens with simple geometries and restricted to some classes of materials. The fatigue limit obtained by fracture mechanics is strongly affected by the boundary conditions and require a correct adjustment of parameters. However, due the large number of parameters, the fatigue phenomenon of different materials can be described statistically by means of stress-life diagrams (S-N diagrams) obtained from standard specimens. The S-N diagrams, therefore, represents the fatigue response of standard specimens subject to specific load conditions. They can be used for mechanical components by means of correction factors to represent broader different operational and manufacturing conditions.

Moraes (2017) extracted fatigue tensile test specimens from a nodular cast iron crankshaft of the original crankshaft model evaluated in this work. Moraes (2017) also applied correction factors to convert the S-N diagram resulting from experimental tensile tests to bending moment loading, according to Figure 5.10.

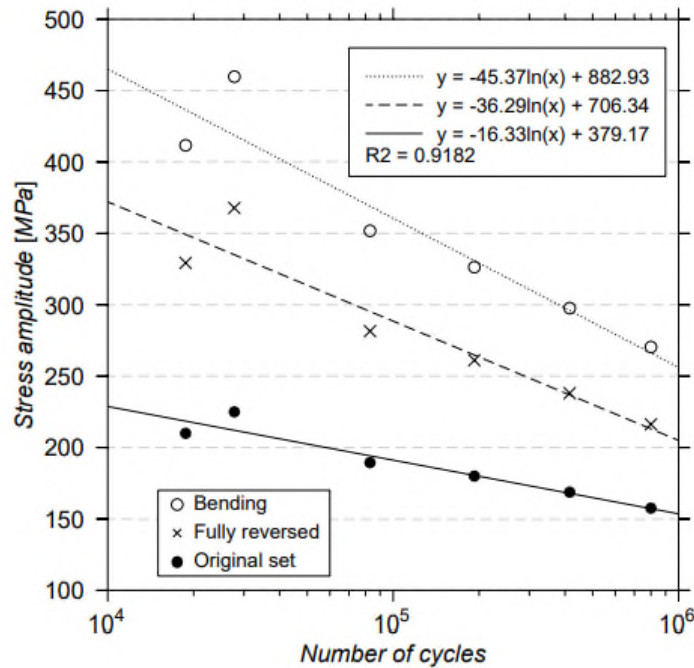


Figure 5.10 – S-N curves for experimental specimen, corresponding fully reversed axial and bending load cases. Available from (MORAES, 2017).

In order to predict the fatigue strength of the crankshafts models subjected to bending loads, the fatigue life, damage and safety factor were verified in a harmonic response analysis. The bending S-N curve showed in Figure 5.10 was input in the ANSYS software and added to the properties of the crankshaft material. The harmonic response analysis was carried out with a constant damping ratio of 0.015. However, similarly to the dynamic calibration, the damping factor did not influence on the fatigue analysis, since the linear relation between acceleration and stress is not affected by this variable, as explained in Section 3.2.

In the fatigue analysis, arbitrary forces were applied to the inertial plate and correlated to the total acceleration, maximum von Mises stress, fatigue strength, damage and safety factor. The excitation force was applied at the distance of 195 mm from the main journal center. The total acceleration was measured in the second inertia plate at distance of 100 mm from the very end, according to Figure 5.11. The fatigue analysis was run for 28,698 seconds, which correspond to 2,000,000 cycles for a frequency of 69.692 Hz. The total acceleration was used in the calculation of the bending moment by means of the numerical dynamic and static calibrations from Figure 4.22 and Figure 4.10. The results obtained for this numerical fatigue analysis is shown in Table 5.12.

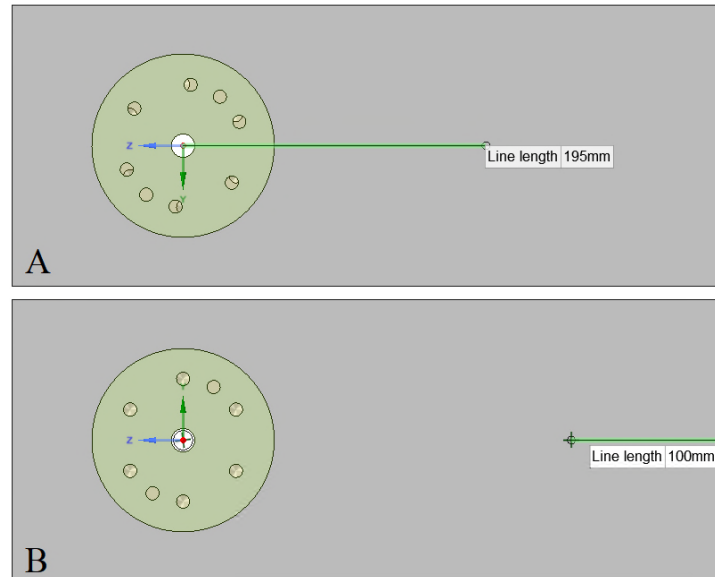


Figure 5.11 – Localization of the (A) force application and (B) measurement of acceleration on the inertia plate.

Table 5.12 – Numerical fatigue response for the original crankshaft model.

Force [N]	Fillet stress [MPa]	Acceleration [g]	Bending [Nm]	Life [cycles]	Damage	Safety Factor
40	145.75	4.08	155.18	2,000,000	1.00	1.54
60	218.62	6.12	232.77	2,000,000	1.00	1.03
62	225.91	6.32	240.53	1,966,290	1.02	0.99
63	229.55	6.43	244.41	1,830,809	1.09	0.98
74	269.63	7.55	287.29	759,573	2.63	0.83

The excitation forces of Table 5.12 do not represent the real excitation force applied by the shaker because the real damping ratio of the system is unknown. However, regardless the excitation force, the relation between stress, acceleration and bending moment is the same. Therefore, the fatigue analysis indicates that, when the accelerometer reaches 6.32 g, the maximum von Mises stress on the fillets reaches the fatigue strength of the crankshaft material for 2 million cycles (226 MPa) and this region is in the imminence of crack nucleation. This acceleration also correspond to 240.53 Nm bending moment, according to the calibration curves.

Figure 5.12 shows the von Mises stress distribution in the crankthrow for

acceleration of 6.43 g. As expected, the maximum stress is located on the surface of the fillet radius. However, for fatigue analysis, it is important to understand how the stress is distributed in the inner region of the fillets. Figure 5.12 (b) indicates high stress gradient, varying from 229 MPa to 102 MPa near the fillet surface. The damage for acceleration of 6.43 g is shown in Figure 5.13 and the safety factor is depicted in Figure 5.14.

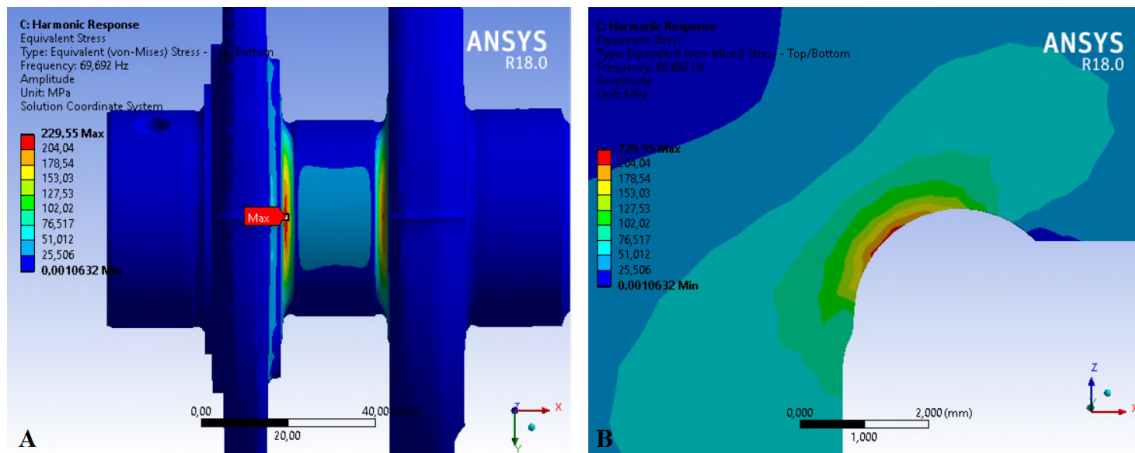


Figure 5.12 – The von Mises stress distribution in the (A) original crankshaft and (B) cut view of the fillet radius for acceleration of 6.43 g.

In the ANSYS software, damage is defined as the relation between the fatigue life obtained in the simulation and the designed fatigue strength of the material. This model, therefore, is not able to predict the location of the crack propagation or nucleation. However, the stress level on fillet radius can be used as estimative of the fatigue strength considering the S-N diagram. The problem is that this analysis type is very conservative because, even though the fatigue strength is reached on the fillet surface, the simulation can not predict the number of cycles necessary to reach 3% drop in the resonance frequency. Furthermore, this fatigue analysis does not take into account the residual stress provided by the deep rolling process on the fillet radii. For these reasons, aiming to a more realistic analysis, the fatigue strength obtained by this method must be converted by two correction factors.



Figure 5.13 – Damage in the fillet radii of the original crankshaft for acceleration of 6.43 g.

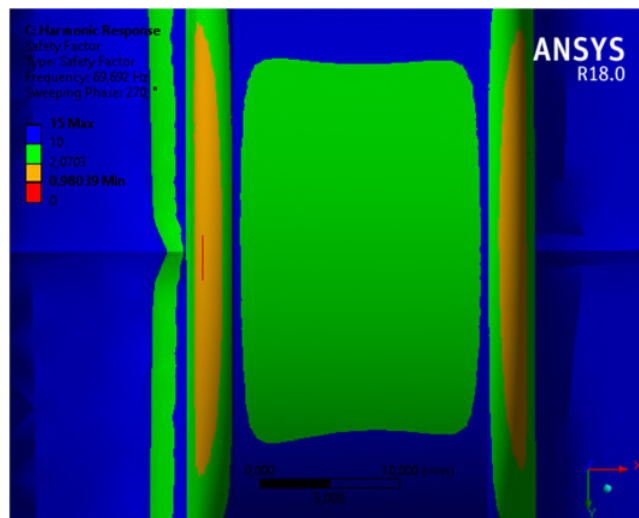


Figure 5.14 – Safety factor in the fillet radii of the original crankshaft for acceleration of 6.43 g.

The first correction factor (k_c) is related to the failure criterion adopted in the fatigue tests. If the fatigue criterion is the crack nucleation on the fillet surface, then $k_c = 1$. If the fatigue criterion is 3% drop in the resonance frequency, then the k_c factor value must be adopted based on previous fatigue tests of similar crankshaft models. The second correction factor (k_s) refers to the surface treatment applied on the fillets of the crankshaft. The deep rolling process has strong influence on the fatigue strength and must be considered in the fatigue analysis. Then, the fatigue strength is calculated by

$$M_F = k_c k_s M_f, \quad (5.6)$$

wherein M_f is the fatigue strength obtained in the numerical simulation and M_F is the actual fatigue limit of the crankshaft described in terms of the bending moment.

Spiteri et al. (2005) conducted fatigue tests in V6 and V8 cast iron crankshafts. Considering the 3% drop in the resonance frequency criterion, they obtained a R90C90 fatigue strength of 496 Nm and 754 Nm for the V6 and V8 models, respectively. Spiteri et al. (2005) compared these results with R75C90 fatigue strength (using surface crack failure criterion) of 367 Nm and 427 Nm obtained by Jensen (1970) in the analysis of the V6 and V8 crankshafts. This comparison showed an increment of 35% and 77% in the fatigue strength of the V6 and V8 models, respectively. Considering that the mean fatigue strength of the original crankshaft model and the characteristics of the V6 and V8 crankshafts, this work adopted $k_f = 1.56$ based on the average of the increment in the fatigue strength of the V6 and V8 crankshafts.

Kamimura (1985) showed that the deep rolling process can increase the crankshaft fatigue strength from 80% until 115% depending on the rolling force. Park (2001) also investigated the influence of the deep rolling in the crankshaft strength and obtained more than 80% of increment in the fatigue limit of a microalloyed steel crankshaft. Regarding the literature, this work assumed an increment of 100% in the fatigue strength ($k_s = 2$) due the influence of the deep rolling process.

The correction factors were used in the fatigue analysis to predict the fatigue strength of the lightweight and original crankshaft models. Table 5.13 shows the fatigue results of the lightweight crankshaft. Table 5.14 shows the numerical fatigue limit calculated for the original and lightweight crankshaft.

Table 5.13 – Numerical fatigue response for the lightweight crankshaft model.

Force [N]	Fillet stress [MPa]	Acceleration [g]	Bending [Nm]	Life [cycles]	Damage	Safety Factor
40	148.46	4.07	155.68	2,000,000	1.00	1.54
60	222.69	6.10	233.52	2,000,000	1.00	1.03
61	226.40	6.20	237.41	1,947,633	1.03	0.99

Table 5.14 – Numerical fatigue strength for the lightweight and original crankshaft subjected to the bending vibration mode.

Crankshaft model	M_f [Nm]	k_c	k_s	M_F [Nm]	Relative Error
Original	240.53	1.56	2.00	750.45	2.29%
Lightweight	237.41	1.56	2.00	740.72	7.2%

The numerical fatigue analysis indicated that the mass reduction of the lightweight model had small influence (1.3%) in the fatigue strength of the crankshaft. This fatigue strength drop, however, was not verified in the experimental tests. The experimental results showed an increase from 768 Nm to 798 Nm in the lightweight model. This discrepancy can be explained by the stochastic nature of the fatigue phenomenon and the low number of specimens tested, since only two specimens were available for bending fatigue tests of the lightweight model. However, considering the standard deviation of 19.1 Nm obtained in the bending fatigue tests of the original model and numerical fatigue analysis, the assumption of small influence of the mass subtraction on the fatigue strength is very reasonable.

In the torsion case, the lack of information about experimental torsion fatigue analysis in the literature prevent a reasonable estimative of parameters for numerical fatigue analysis. The experimental results showed a slightly decrease (from 2278 Nm to 2190 Nm) in the fatigue life of the lightweight model.

6. CONCLUSIONS

The torsional test rig designed and manufactured for fatigue tests of the crankshaft specimens had good performance in operation. Its resonance frequency was well correlated to the numerical modal analysis and the resonant testing method was very efficient and time saving for fatigue evaluation. At the same time, the 3% frequency drop criterion was effective in the crack detection. The liquid penetrant analyses revealed cracks in all specimens that showed resonance frequency drop during the fatigue test.

The CAD and CAE tools used in this work were very useful in the designing stage of the torsional test rig and the lightweight crankshaft model. The numerical modal analysis predicted with accuracy the resonance frequency of the torsion mode of vibration. The structural simulations also showed good correlation with experimental results. The divergence of the fatigue limit calculated by the numerical calibrations and experimental ones was less than 3% for the bending case and less than 9% for the torsion case. The comparison between curves of the numerical and experimental calibrations indicates that CAE tools are reliable and can be used as reference to predict the characteristics of new crankshaft models.

The fatigue assessment of the specimens were well performed for both bending and torsion cases. As expected, the bending loading was more critical for fatigue of the specimens, since the fatigue strength of the torsion test was about three times as much as the bending one. In the bending tests, the cracks nucleated in the bottom region of the fillet radius and propagated throughout the crankweb. Under torsion loading, otherwise, the crack nucleated at the oil hole and propagated at 45° from the crankpin centerline.

The numerical fatigue analysis showed good correlation with experimental results. The S-N diagram methodology applied with finite element analysis and the correction factors was able to predict the fatigue limit with less than 3% error for the original model and less than 8% for the lightweight model. The experimental and numerical structural analysis showed that the modifications performed in the lightweight model had small influence in the stiffness and stress distribution. Besides that, both numerical and experimental fatigue analyses indicated that the fatigue life of the lightweight model is very similar to the original one. The balancing analysis also showed that the symmetry of the four-cylinder crankshaft ensures the static and dynamic balancing. Therefore, the modification performed in the crankshaft geometry enabled about 10% of mass reduction without relevant influence in the balancing and the fatigue strength of the crankshaft.

REFERENCES

- ANSYS, Inc. **ANSYS 15.0 Mechanical User's Guide**. [S.l.], 2013.
- ASTM STP91A. **A Guide for Fatigue Testing and the Statistical Analysis of Fatigue Data**. USA, 1963. 1-94 p.
- BROWNLEE, K.; JR, J. H.; ROSENBLATT, M. The up-and-down method with small samples. **Journal of the American Statistical Association**, Taylor & Francis Group, v. 48, n. 262, p. 262–277, 1953.
- BS 3518-5. **Fatigue Testing Part 5: Guide to the application of statistics**. UK, 1966. 1-44 p.
- CABEZAS, E. CELENTANO, D. (2002). Experimental and numerical analysis of the tensile test using sheet specimens. **Mecánica Computacional XXI**, 854–873.
- CHIEN, W. *et al.* Fatigue analysis of crankshaft sections under bending with consideration of residual stresses. **International Journal of Fatigue**, Elsevier, v. 27, n. 1, p. 1–19, 2005.
- DIXON, W. The up-and-down method for small samples. **Journal of the American Statistical Association**, Taylor & Francis Group, v. 60, n. 312, p. 967–978, 1965.
- DIXON, W. J.; MOOD, A. M. A method for obtaining and analyzing sensitivity data. **Journal of the American Statistical Association**, Taylor & Francis, v. 43, n. 241, p. 109–126, 1948.
- JENSEN, E. Crankshaft strength through laboratory testing. **SAE Technical Paper**, 1970.
- FENG, M.; LI, M. Development of a computerized electrodynamic resonant fatigue test machine and its applications to automotive components. **SAE Technical Paper**, 2003.
- FONSECA, L. G. A. **Crankshaft Deep Rolling Modeling Through Explicit Analysis Using Finite Element Method**. Master's Thesis — Instituto Tecnológico de Aeronáutica, 2015.
- GRUM, J. Analysis of residual stresses in main crankshaft bearings after induction surface hardening and finish grinding. **Proceedings of the Institution of Mechanical Engineers, Part D: Journal of Automobile Engineering**, Sage Publications Sage UK: London, England, v. 217, n. 3, p. 173–182, 2003.
- GUDMUNDSON, P. Eigenfrequency changes of structures due to cracks, notches or other geometrical changes. **Journal of the Mechanics and Physics of Solids**, Elsevier, v. 30, n. 5, p. 339–353, 1982.
- ISO1940. **Mechanical vibration - Balancing quality requirements for rotors in a constant (rigid) state**. 2003.
- KAMIMURA, T. Effects of fillet rolling on fatigue strength of ductile cast iron crankshaft. **SAE Technical Paper**, 1985.
- LEE, Y.-L. **Fatigue Testing and Analysis: Theory and Practice**. [S.l.]: Butterworth-Heinemann, 2005. v. 13.

- LEE, Y.-L.; MORRISSEY, W. Uncertainties of experimental crankshaft fatigue strength assessment. **International Journal of Materials and Product Technology**, Interscience Publishers, v. 16, n. 4-5, p. 379–392, 2001.
- MONTAZERSADGH, F. H.; FATEMI, A. Dynamic load and stress analysis of a crankshaft. **SAE Technical Paper**, 2007.
- MONTAZERSADGH, F. H.; FATEMI, A. Stress analysis and optimization of crankshafts subject to dynamic loading. **Americal Iron and Steel Institute**, 2007.
- MONTAZERSADGH, F. H.; FATEMI, A. Optimization of a forged steel crankshaft subject to dynamic loading. **SAE International Journal of Materials and Manufacturing**, v. 1, n. 2008-01-0432, p. 211–217, 2008.
- MORAES, E.B. **Numerical and Experimental Fatigue Analysis of Crankshaft**. 2017. Master's thesis. Faculdade de Engenharia Mecânica, Universidade Estadual de Campinas, Campinas.
- NAKAZAWA, HAJIME and SHOTARO KODAMA. Statistical S-N Testing Method with 14 Specimens: JSME Standard Method for Determination of S-N Curves. *Statistical Research on Fatigue and Fracture*, Japan Society of Materials Science, Elsevier (New York), 1987.
- NORTON, R. **Machine Design: An Integrated Approach**. [S.l.]: Prentice Hall, 2013.
- PARK, H.; KO, Y. S.; JUNG, S. C. Fatigue life analysis of crankshaft at various surface treatments. **SAE Technical Paper**, 2001.
- PATEL, R. K.; SPITERI, P. V. Development of a computerized digital resonance fatigue test controller with load feedback management. **SAE Technical Paper**, 2006.
- POLLAK, R.; PALAZOTTO, A.; NICHOLAS, T. A simulation-based investigation of the staircase method for fatigue strength testing. **Mechanics of Materials**, Elsevier, v. 38, n. 12, p. 1170–1181, 2006.
- PULKRABEK W. W. *Engineering fundamentals of the internal combustion engine*. **Prentice Hall upper saddle river**, New Jersey, 1997.
- RANGWALA, A. S. *Reciprocating Machinery Dynamics*. **New Age International**, New Delhi, 2006.
- RODRIGUES A. S. **Análise Dinâmica e Balanceamento de Virabrequins Leves de Motores**, Master's Thesis, Unicamp, 2013.
- SIMÕES, D. A. **Entalhes Melhorados e Otimizados**, Master's Thesis, PUC-Rio, 2012.
- SNYDER, P. M.; LU, M.-W.; LEE, Y.-L. Reliability-based fatigue strength testing by the staircase method. **SAE Technical Paper**, 2004.
- SPITERI, P.; HO, S.; LEE, Y.-L. Assessment of bending fatigue limit for crankshaft sections with inclusion of residual stresses. **International Journal of fatigue**, Elsevier, v. 29, n. 2, p. 318–329, 2007.
- SPITERI, P. V.; LEE, Y.-L.; SEGAR, R. An exploration of failure modes in rolled, ductile,

cast-iron crankshafts using a resonant bending testing rig. **SAE Technical Paper**, 2005.

VILLALVA, S. G.; JUNIOR, E. G. F. Correlation between CAE and experimental fatigue bench tests for automotive crankshafts. **SAE Technical Paper**, 2010.

WILLIAMS, J.; FATEMI, A. Fatigue performance of forged steel and ductile cast iron crankshafts. **SAE Technical Paper**, 2007.

WILLIAMS, J.; MONTAZERSADGH, F.; FATEMI, A. Fatigue performance comparison and life predictions of forged steel and ductile cast iron crankshafts. **University of Toledo, Ohio**, 2007.

YU, V. *et al.* Testing and modeling of frequency drops in resonant bending fatigue tests of notched crankshaft sections. **SAE Technical Paper**, 2004.

ZOROUFI, M.; FATEMI, A. A literature review on durability evaluation of crankshafts including comparisons of competing manufacturing processes and cost analysis. In: **26th Forging Industry Technical Conference**. [S.l.: s.n.], 2005.

APPENDIX A – TEST RIG COMPONENTS DRAWINGS

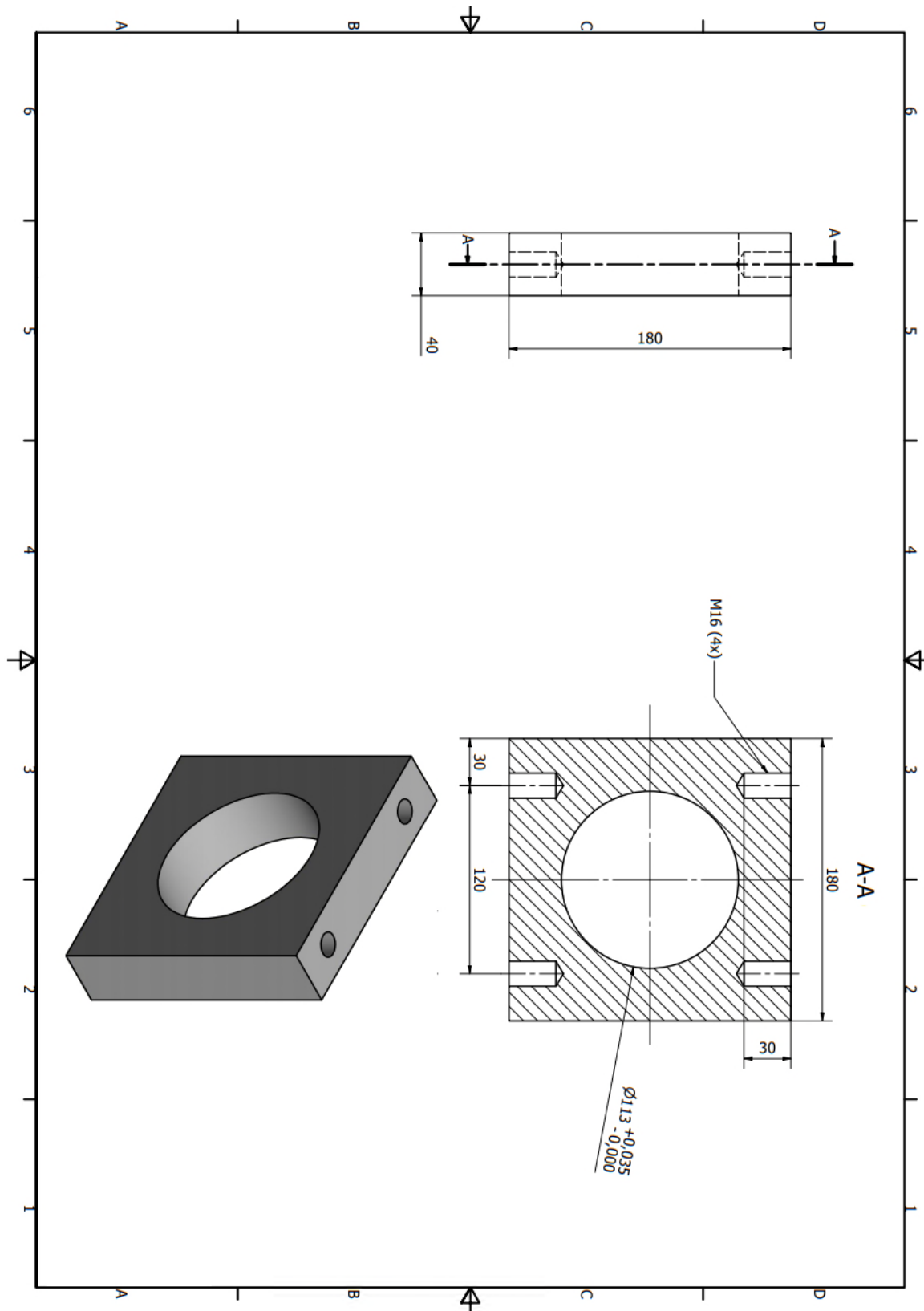


Figure A.1 – Inertia plate base drawing with dimensions in mm.

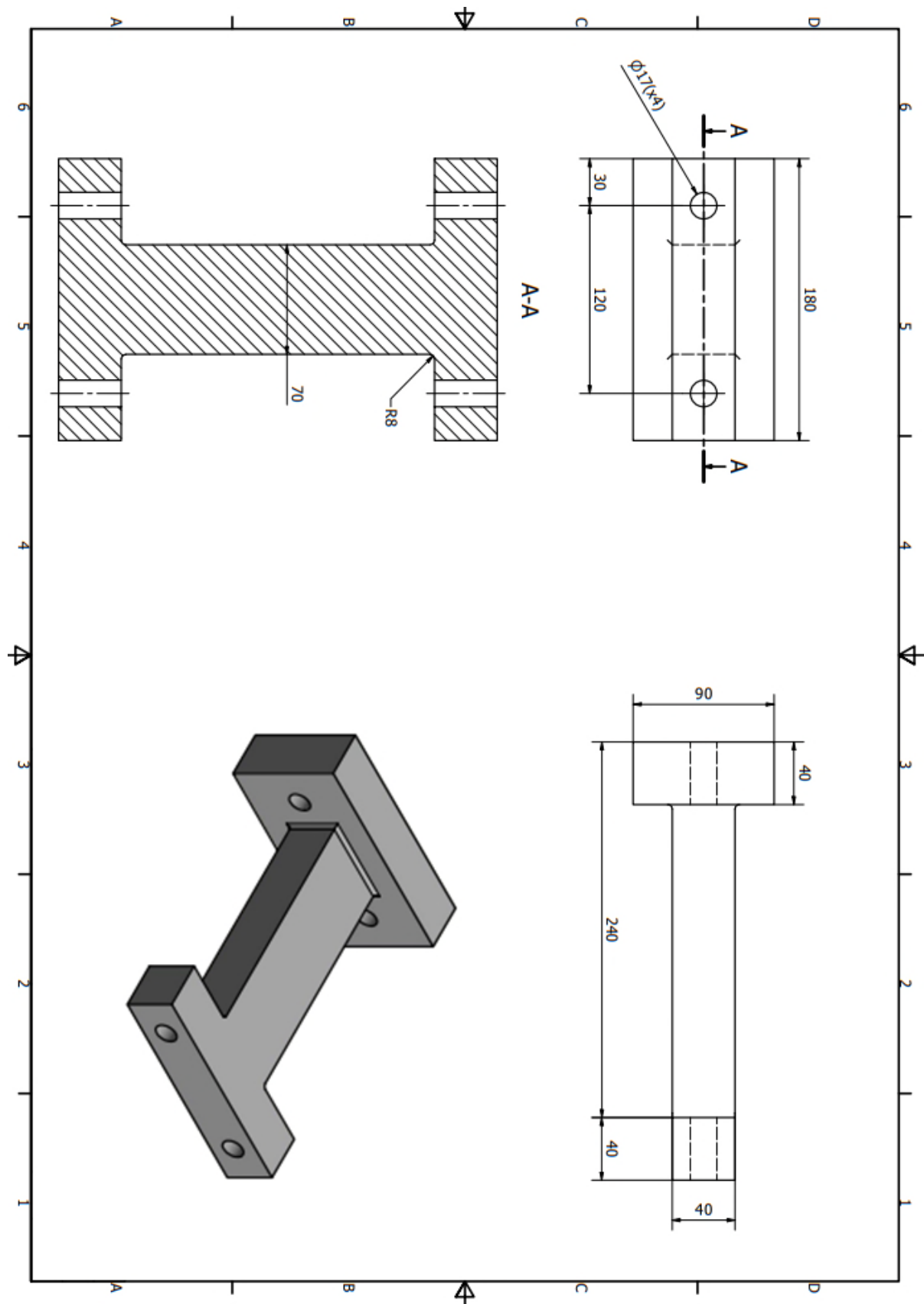


Figure A.2 – Inertia plate arm drawing with dimensions in mm.

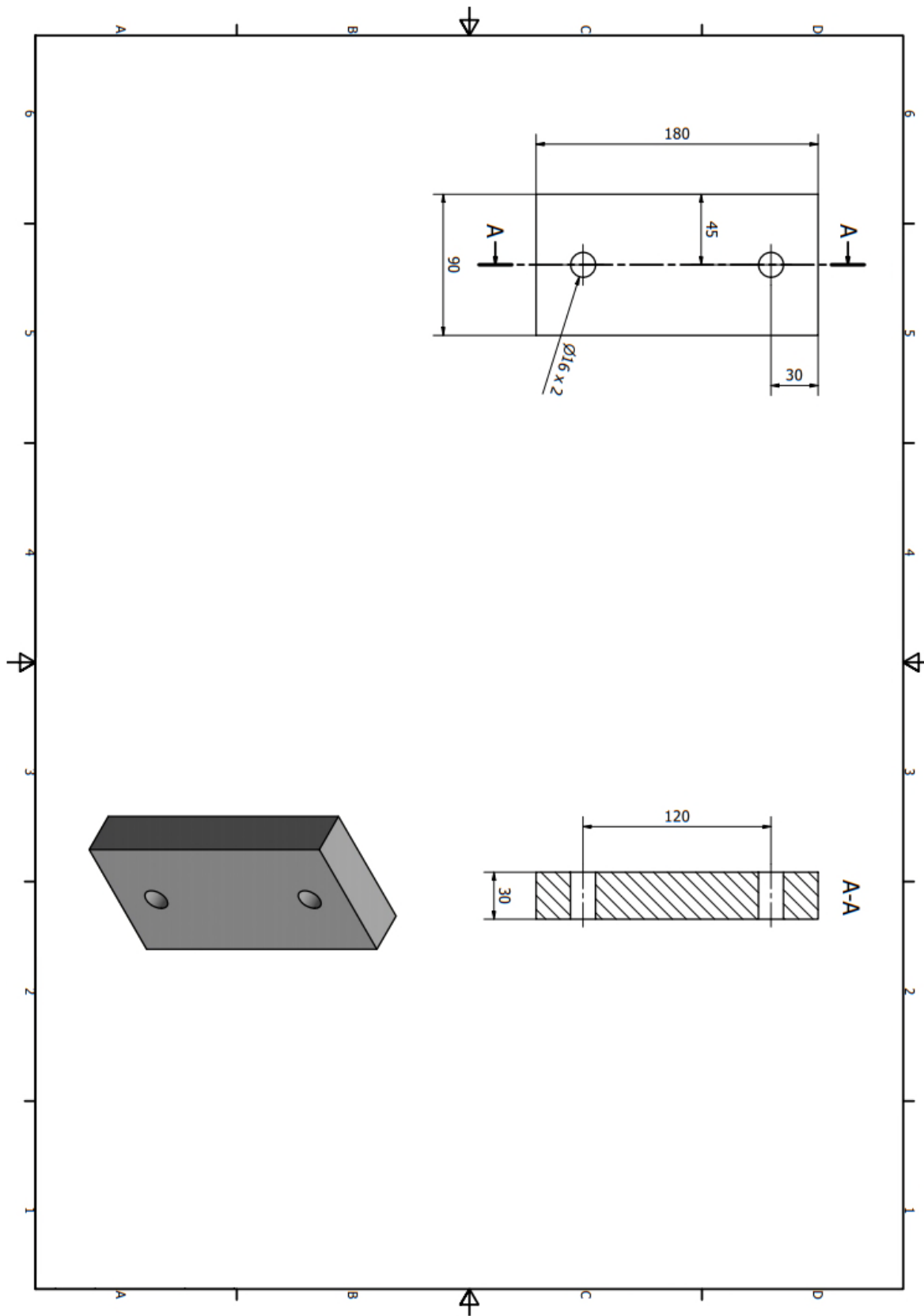


Figure A.3 – Inertia plate block drawing with dimensions in mm.

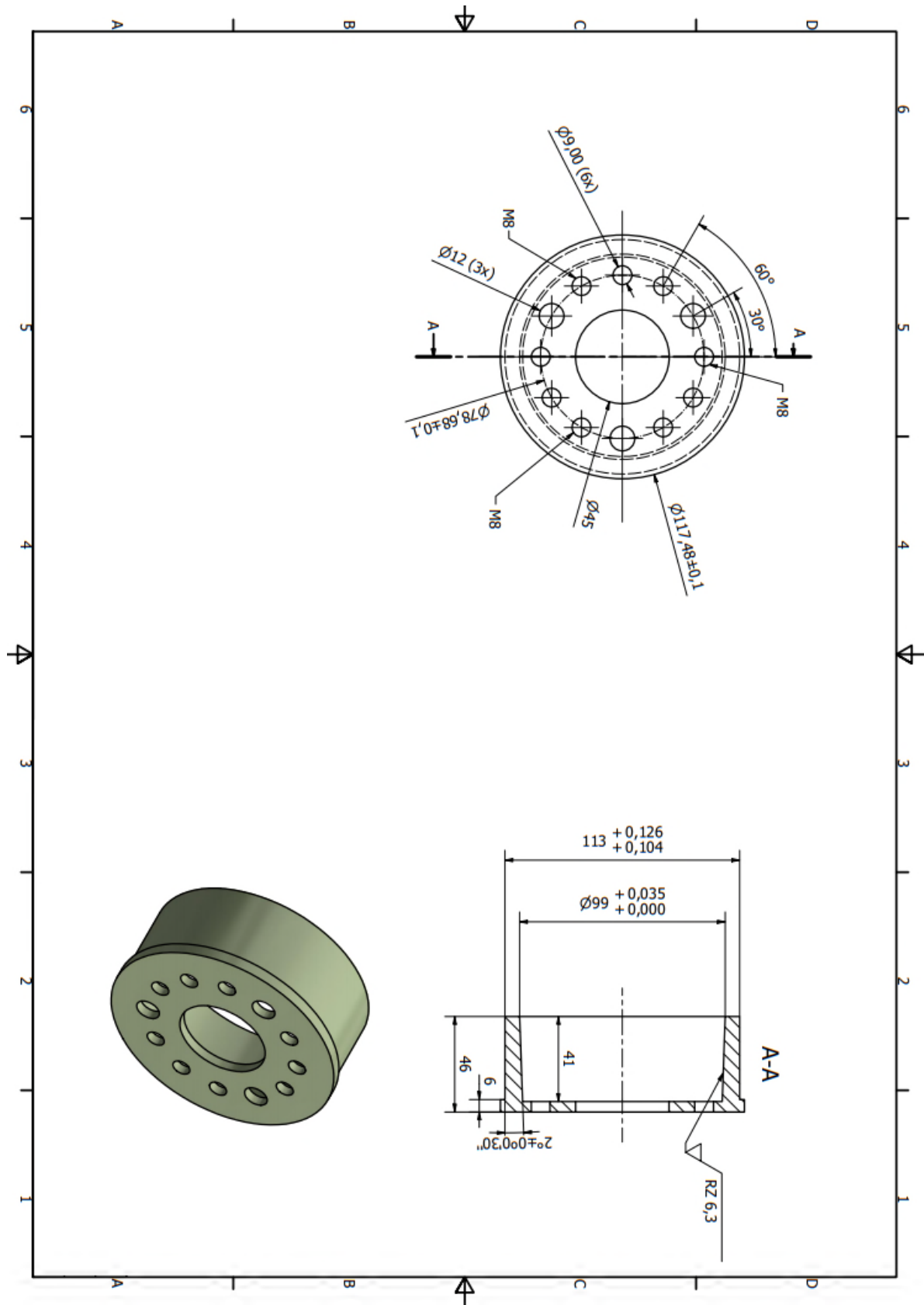


Figure A.4 – External sleeve drawing with dimensions in mm.

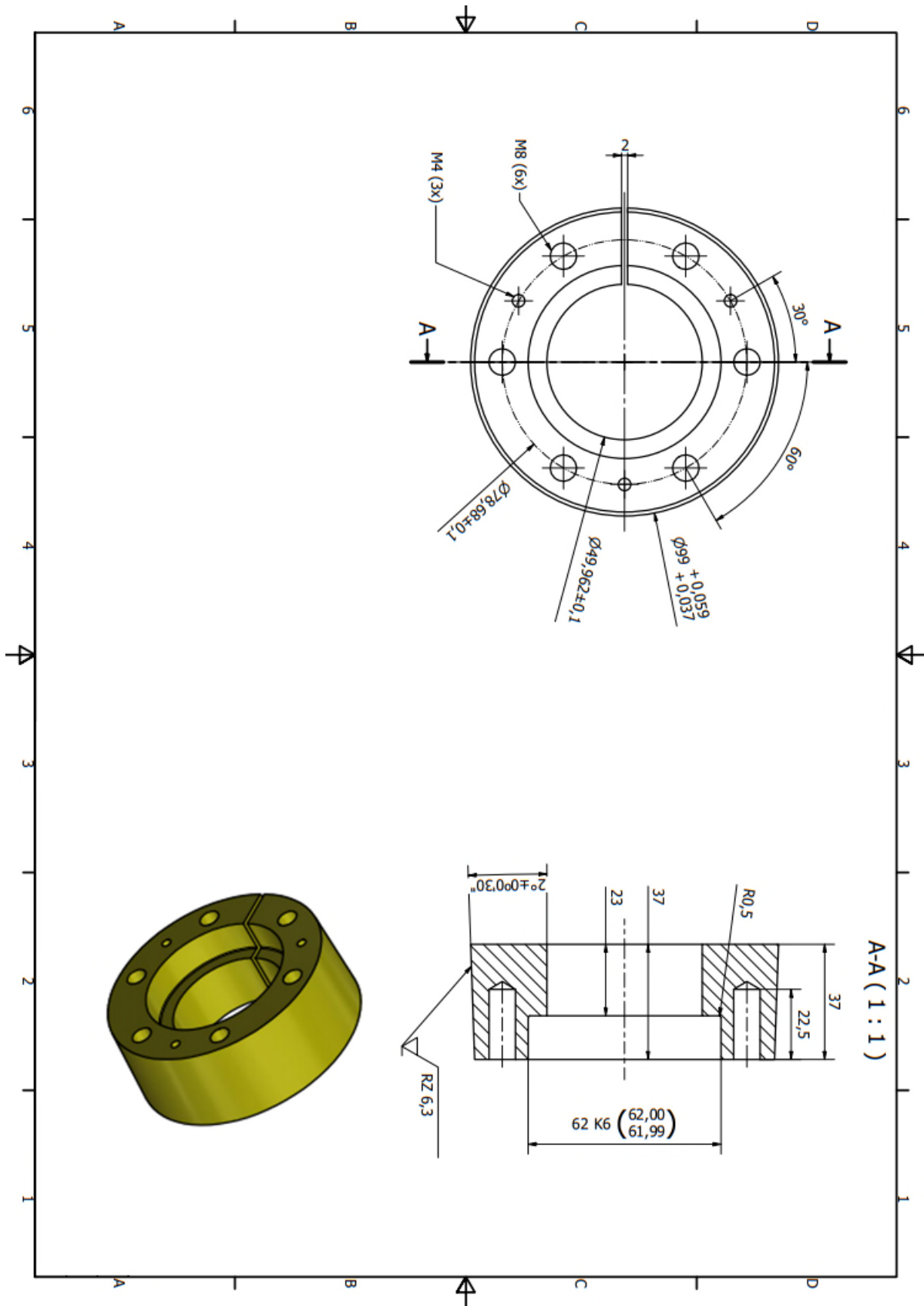


Figure A.5 – Internal sleeve drawing with dimensions in mm.

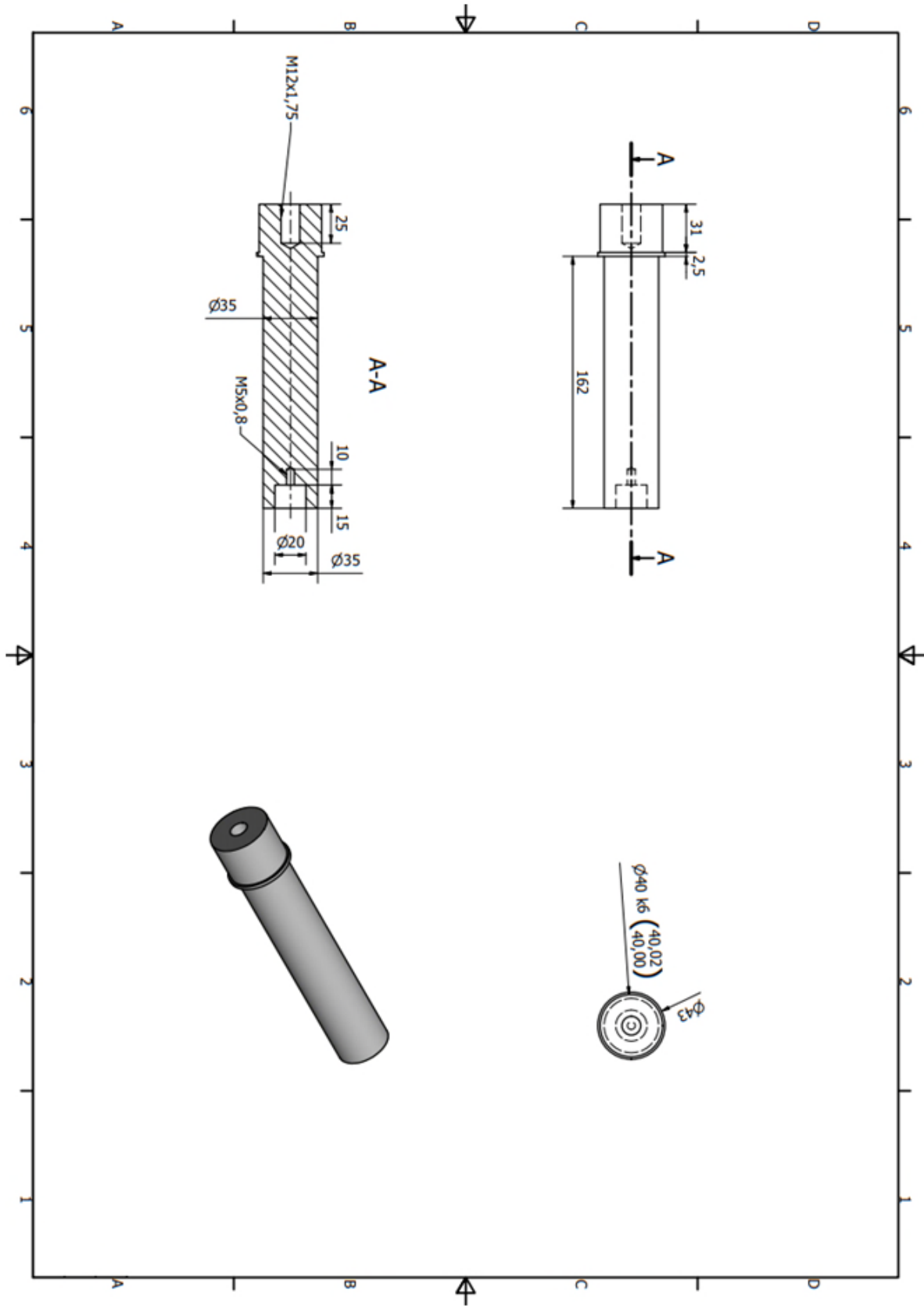


Figure A.6 – Shaft drawing with dimensions in mm.

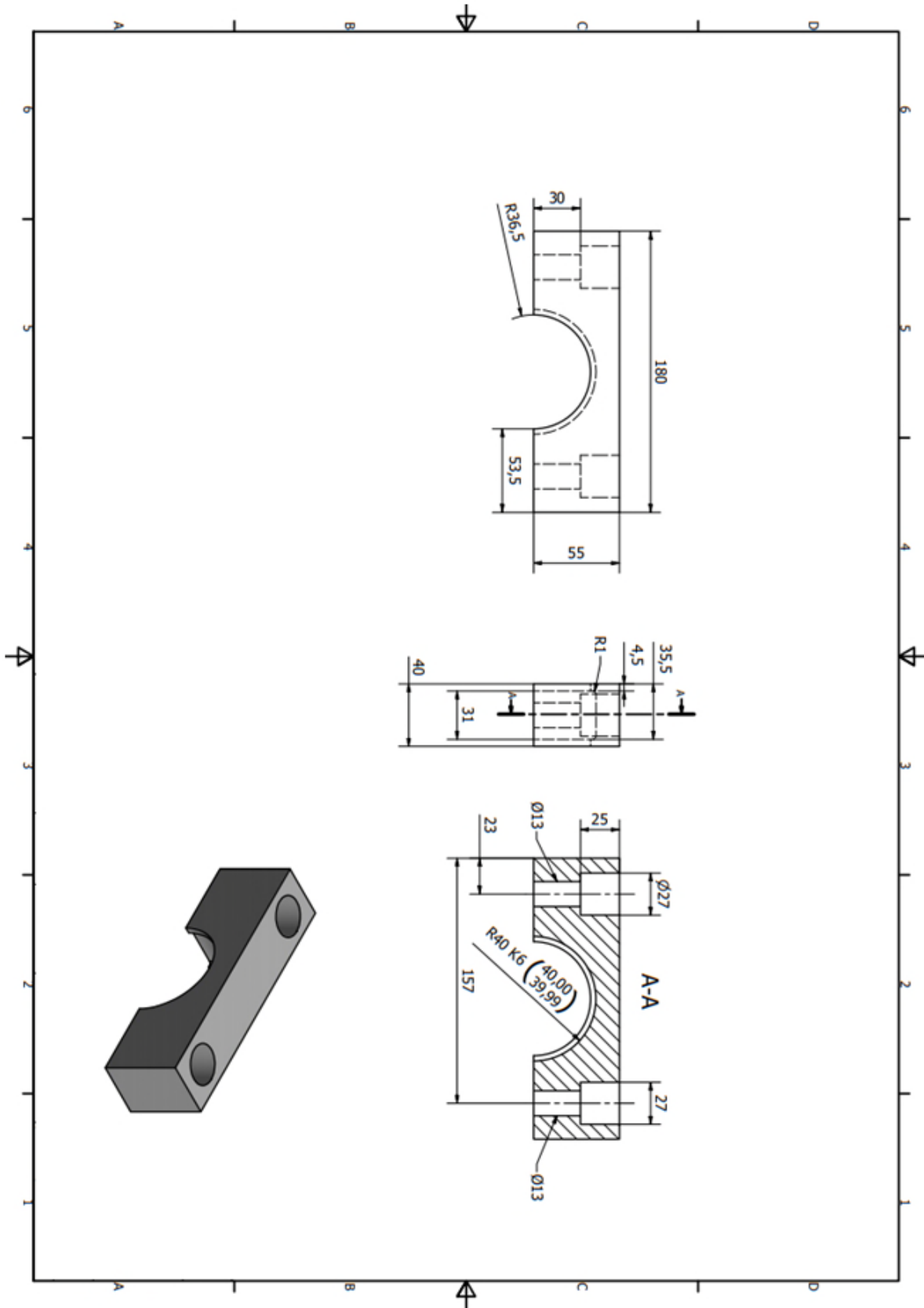


Figure A.7 – Upper fixed support with dimensions in mm.

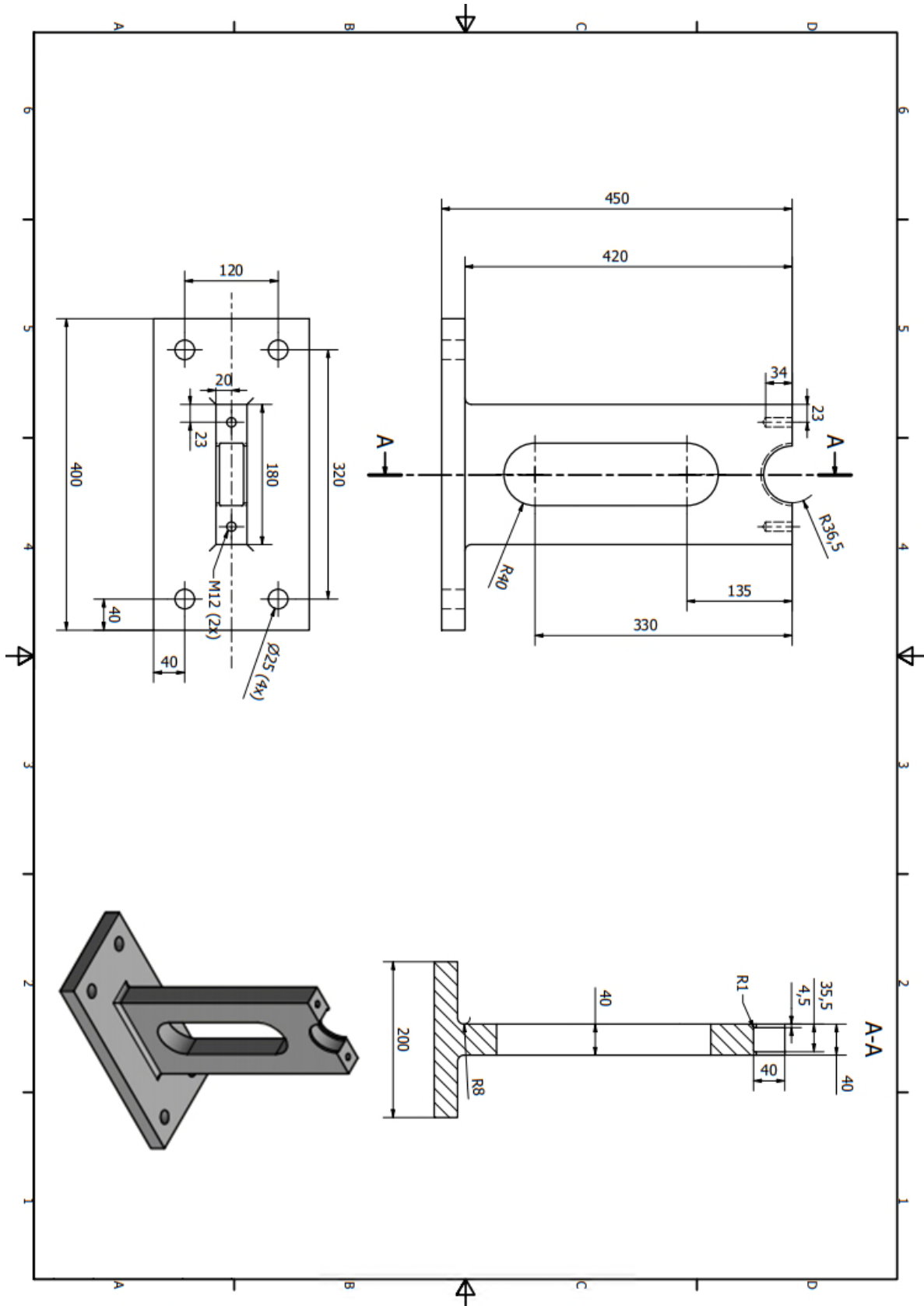


Figure A.8 – Bottom fixed support with dimensions in mm.

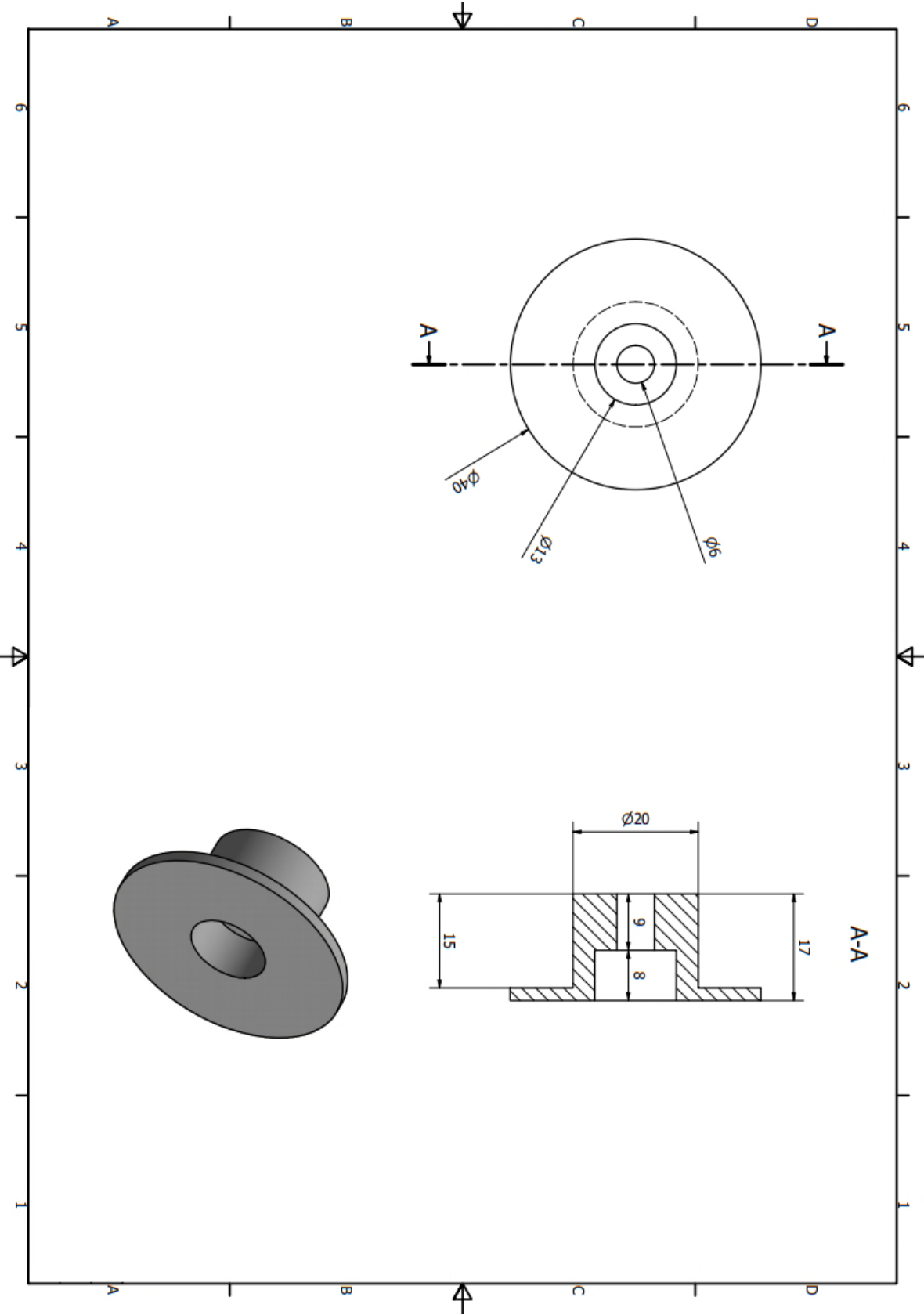


Figure A.9 – Bearing support with dimensions in mm.